THE UNIVERSITY OF QUEENSLAND

AUSTRALIA

Kinetic, mechanistic, structural and spectroscopic investigations of Bimetallic Metallohydrolases

Christopher Michael Selleck

Bachelor of Science (Hons)

A thesis submitted for the degree of Doctor of Philosophy at
The University of Queensland in 2017

School of Chemistry and Molecular Biology

Abstract

Binuclear Metallohydrolases (BMHs) are a vast family of enzymes that play crucial roles in numerous metabolic pathways. The overarching aim of this thesis is the investigation of the structure and mechanism of a series of related BMHs, with a range of physicochemical techniques, in order to provide essential insight into the development of specific inhibitors. Since an increasing number of BMHs have become targets for chemotherapeutic agents, such inhibitors may thus serve as suitable leads in drug development.

The general biochemical properties of BMHs is discussed in Chapter 1. Particular focus is on antibiotic-degrading metallo-β-lactamases (MBLs), Zn^{2+}-dependent enzymes that have emerged as a major threat to global health care due to their ability to inactivate most of the commonly used antibiotics. No clinically relevant inhibitors for these enzymes are currently available, exacerbating their negative impact on the treatment of infections. Also discussed are a range of phosphatases; while functionally distinct from MBLs, they employ a related mechanistic strategy to hydrolyse a broad range of phosphorylated substrates. Specifically, purple acid phosphatases (PAPs) are also a useful target for novel chemotherapeutics to treat osteoporosis, while organophosphate (OP) pesticide-degrading enzymes have gained attention as biocatalysts for application in environmental remediation.

In Chapter 2 the trajectory and transition state of the PAP-catalysed reaction is investigated using a high-resolution crystal structure. Importantly, the inhibitor and substrate mimic phosphate is observed in two alternative conformations. When superimposed they describe a trigonal bipyramidal structure reminiscent of the proposed transition state. Hence, this study provides the first crystallographic insight into the transition state of a BMH-catalysed reaction and may thus guide transition state-based inhibitor designs.

In Chapter 3 the crystal structure of a fluoride-inhibited OP-degrading BMH, the OP-degrading enzyme from *Agrobacterium radiobacter* (OpdA) is described. The significance of this structure is that it highlights the significance of hydrogen bonding interactions in enhancing minor structural changes into significant functional differences. Specifically, we demonstrate that in the absence of

this hydrogen bond fluoride has no effect on enzyme performance, and illustrate that fluoride binding mediates long range effects that influence substrate binding and thus catalytic efficiency.

In Chapter 4 the crystal structures of two novel MBLs from the non-pathogenic marine microorganisms *Novosphingobium pentaromativorans* and *Simiduia agarivorans* (*i.e.* Maynooth ImiPenemase -1 and -2 (MIM-1 and MIM-2), respectively) are described. These enzymes were discovered in a database mining study and highlight that antibiotic-degrading activity is present in environments that are not specifically challenged by human activities. Both MIM-1 and MIM-2 are efficient MBLs, but are also acting as quorum-sensing enzymes by hydrolysing a range of lactone substrates. Their crystal structures demonstrate that the MBL active site can accommodate a range of diverse substrates. This observation may render the design of potent inhibitors more difficult as the active site may be flexible and/or too ill-defined to interact with a persistent and specific inhibitor.

In Chapter 5 the structural and functional flexibility of the MBL active site was further investigated with a range of kinetic and spectroscopic techniques. The focus of this study, Adelaide ImiPenemase 1 (AIM-1), is a pathogenic MBL isolated from P*seudomonas aeruginosa*. The enzyme has two distinct options available for the hydrolysis of β-lactam substrates, distinguished by the identitiy of the rate-limiting step. This observation supports a model whereby the initial conformation of the bound substrate is rather flexible, thus providing an opportunity for the reaction to proceed in two alternative pathways. This flexibility may indeed be a useful strategy for the enzyme to remain dynamic with respect to its evolution. In essence, due to this flexibility AIM-1 may adapt to novel substrates quickly, exacerbating its role in spreading antibiotic resistance.

In Chapters 2 to 5 physico-chemical and structural properties of BMHs with diverse functions and substrate preferences have been discussed. In Chapter 6 it is demonstrated that the in-solution structures of a selection of BMHs (representing both phosphatases and MBLs) are indeed rather conserved. Specifically, the use of magnetic circular dichroism (MCD) is a simple and informative technique to probe the coordination environments of BMHs. In Chapter 6 we utilise this technique to investigate CpsB, an emerging target for novel agents to combat antibiotic resistance, and the MBL-like proteins LRA-8, MIM-1 and MIM-2. All of which originate from environmental bacteria that are not associated with human disease (the crystal structures of MIM-1 and MIM-2 were described in Chapter 4). Co^{2+} was used as a paramagnetic probe for these MCD studies, facilitating a detailed comparison to related BMH and model systems. The spectroscopic data indicate that despite considerable functional/metabolic differences, numerous BMHs share close active site structural

similarity. Thus, the active site characteristic of numerous BMHs is characterised by functional plasticity that may allow at least some of these enzymes (*i.e.* MBLs) to adopt novel functions rapidly.

In summary, insights gained from this thesis may inform the design and development of potent inhibitors for BMHs that can be used as leads for novel chemotherapeutic strategies. Failure to do so in the near future presents grave dangers for the future of human health and the treatment of many human ailments. In Chapter 7 some recent initial studies are introduced which demonstrate several potent MBL inhibitors that are active against representatives from each of the three main groups of MBLs (*i.e.* the B1-, B2- and B3-subgroups). The study was also expanded to include preliminary data of a novel MBL-like enzyme from *Salmonella typhimurium*. The hope is that with further studies like the one presented in this thesis, will lead to positive outcomes for healthcare leading into the future.

Declaration by author

This thesis is composed of my original work, and contains no material previously published or written by another person except where due reference has been made in the text. I have clearly stated the contribution by others to jointly-authored works that I have included in my thesis.

I have clearly stated the contribution of others to my thesis as a whole, including statistical assistance, survey design, data analysis, significant technical procedures, professional editorial advice, and any other original research work used or reported in my thesis. The content of my thesis is the result of work I have carried out since the commencement of my research higher degree candidature and does not include a substantial part of work that has been submitted to qualify for the award of any other degree or diploma in any university or other tertiary institution. I have clearly stated which parts of my thesis, if any, have been submitted to qualify for another award.

I acknowledge that an electronic copy of my thesis must be lodged with the University Library and, subject to the policy and procedures of The University of Queensland, the thesis be made available for research and study in accordance with the Copyright Act 1968 unless a period of embargo has been approved by the Dean of the Graduate School.

I acknowledge that copyright of all material contained in my thesis resides with the copyright holder(s) of that material. Where appropriate I have obtained copyright permission from the copyright holder to reproduce material in this thesis.

Publications during candidature

Peer Reviewed papers:

AIM-1: an antibiotic-degrading metallohydrolase that displays mechanistic flexibility.

Chem. Eur. J; accepted: DOI: 10.1002/chem.201602762, Volume 22, Issue 49 December 5, 2016, Pages 17704–17714.

http://dx.doi.org/10.1002/chem.201602762

Christopher Selleck, James L. Larrabee, Jeffrey Harmer, Luke W. Guddat, Nataša Mitić, Waleed Helweh, David L. Ollis, Whitney A. Craig, David L. Tierney, Marcelo Monteiro Pedroso, Gerhard Schenk.

Visualization of the reaction trajectory and transition state in a hydrolytic reaction catalysed by a metalloenzyme.

Chem. Eur. J; accepted: DOI: 10.1002/chem.201700866, Volume 23, Issue 20 April 6, 2017, Pages 4778–4781.

http://dx.doi.org/10.1002/chem.201700866

Christopher Selleck, Daniel Clayton, Lawrence R. Gahan, Nataša Mitić, Ross P. McGeary , Marcelo Monteiro Pedroso, Luke W. Guddat, Gerhard Schenk.

High resolution crystal structure of a fluoride-inhibited organophosphate-degrading metallohydrolase.

J. Inorg. Bio; In Press, Corrected proof: DOI: 10.1016/j.jinorgbio.2017.06.013, June 27, 2017.

https://doi.org/10.1016/j.jinorgbio.2017.06.013

Christopher Selleck, Luke W. Guddat, David L. Ollis, Gerhard Schenk, Marcelo Monteiro Pedroso.

Metallo-β-lactamases: a major threat to human health.

AJMB; accepted: DOI:10.4236/ajmb.2014.43011, Vol.4 No.3, July 2014, Pages 89-104.

http://dx.doi.org/10.4236/ajmb.2014.43011

Emer K. Phelan, Manfredi Miraula, **Christopher Selleck**, David L. Ollis, Gerhard Schenk, Nataša Mitić·

Structure-Activity Relationship Study and Optimization of 2-Aminopyrrole-1-benzyl-4,5-diphenyl-1H-pyrrole-3-carbonitrile as a Broad Spectrum Metallo-β-lactamase Inhibitor. EJMECH; accepted: DOI:10.1016/j.ejmech.2017.05.061, Volume 137, September 8, 2017, Pages 351-364.

https://doi.org/10.1016/j.ejmech.2017.05.061

Ross McGeary, Daniel Tan, **Christopher Selleck**, Marcelo Pedroso, Hannah Sidjabat, Gerhard Schenk.

Reaction mechanism of the metallohydrolase CpsB from Streptococcus pneumoniae, a promising target for novel antimicrobial agents.

Dalton Trans.; accepted, epub ahead of print, May 26, 2017: DOI: 10.1039/c7dt01350g.

http://dx.doi.org/10.1039/C7DT01350G

Marcelo Monteiro Pedroso, **Christopher Selleck,** Jessica Bilyj, Jeffrey R. Harmer, Lawrence R. Gahan, Nataša Mitić, Alistair Standish, David L. Tierney, James L. Larrabee, Gerhard Schenk.

Characterization of a highly efficient antibiotic-degrading metallo-β-lactamase obtained from an uncultured member of a permafrost community.

Metallomics; accepted, epub ahead of print, Jul 27, 2017: DOI:10.1039/c7mt00195a.

http://dx.doi.org/10.1039/C7MT00195A

Marcelo M. Pedroso, **Christopher Selleck,** Charmaine Enculescu, Jeffrey R. Harmer, Nataša Mitić, Whitney R. Craig, Waleed Helweh, Philip Hugenholtz, Gene W. Tyson, David L. Tierney, James A. Larrabee, Gerhard Schenk.

Book Chapters:

Catalytic mechanisms of metallohydrolases containing two metal ions.

In Christo I. Christov (Ed.), Metal-Containing Enzymes (pp. 49-81) Maryland Heights, MO, United States: Academic Press. DOI: 10.1016/bs.apcsb.2014.07.002, Volume 97, 2014, Pages 49-81.

http://pubs.acs.org/doi/abs/10.1021/cr050318f

Nataša Mitić, Manfredi Miraula, **Christopher Selleck,** Kieran S. Hadler, Elena Uribe, Marcelo M. Pedroso, Gerhard Schenk.

Publications included in this thesis:

Visualization of the reaction trajectory and transition state in a hydrolytic reaction catalysed by a metalloenzyme.

Chem. Eur. J; accepted: DOI: 10.1002/chem.201700866, Volume 23, Issue 20 April 6, 2017, Pages 4778–4781.

http://dx.doi.org/10.1002/chem.201700866

Christopher Selleck, Daniel Clayton, Lawrence R. Gahan, Nataša Mitić, Ross P. McGeary , Marcelo Monteiro Pedroso, Luke W. Guddat, Gerhard Schenk. - Incorporated as **Chapter 3**.

Contributor	Statement of contribution
Christopher Selleck	Experimental work (75%) Analysis (80%) Writing and interpretation (60%)
Daniel Clayton	Experimental work (25%)
Marcelo Monteiro Pedroso	Analysis (5%)
Nataša Mitić	Analysis (5%)
Luke W. Guddat	Analysis (10%)
Gerhard Schenk	Writing and interpretation (30%)
Lawrence R. Gahan	Writing and interpretation (5%)
Ross P. McGeary	Writing and interpretation (5%)

High resolution crystal structure of a fluoride-inhibited organophosphate-degrading metallohydrolase.

J. Inorg. Bio; In Press, Corrected proof: DOI: 10.1016/j.jinorgbio.2017.06.013, June 27, 2017.

https://doi.org/10.1016/j.jinorgbio.2017.06.013

Christopher Selleck, Luke W. Guddat, David L. Ollis, Gerhard Schenk, Marcelo Monteiro Pedroso. - Incorporated as **Chapter 3**.

Contributor	Statement of contribution
Christopher Selleck	Experimental work (70%) Analysis (80%) Writing and interpretation (60%)
Marcelo Monteiro Pedroso	Experimental work (30%) Analysis (10%) Writing and interpretation (5%)
Luke W. Guddat	Analysis (10%)
David L. Ollis	Writing and interpretation (5%)
Gerhard Schenk	Writing and interpretation (30%)

AIM-1: an antibiotic-degrading metallohydrolase that displays mechanistic flexibility.

Chem. Eur. J; accepted: DOI: 10.1002/chem.201602762, Volume 22, Issue 49 December 5, 2016, Pages 17704–17714.

http://dx.doi.org/10.1002/chem.201602762

Christopher Selleck, James L. Larrabee, Jeffrey Harmer, Luke W. Guddat, Nataša Mitić, Waleed Helweh, David L. Ollis, Whitney A. Craig, David L. Tierney, Marcelo Monteiro Pedroso, Gerhard Schenk. - Incorporated as **Chapter 5**.

Contributor	Statement of contribution
Christopher Selleck	Experimental work (80%) Analysis (60%) Writing and interpretation (60%)
Marcelo Monteiro Pedroso	Experimental work (12%) Analysis (20%) Writing and interpretation (10%)
Larrabee JA	Experimental work (2%)
Craig WR	Experimental work (2%)
Tierney DL	Experimental work (2%)
Helweh W	Experimental work (2%)
Ollis DL	Analysis (5%)
Harmer J	Analysis (5%)
Guddat LW	Analysis (5%)
Mitić N	Analysis (5%)
Gerhard Schenk	Writing and interpretation (30%)

Contributions by others to the thesis

Professor Gerhard Schenk and Doctor Marcelo Pedroso have assisted me with experimental design, conceptual data analysis and corrections to this thesis. Prof Luke Guddat manipulated the MX-2 beam during the collection of crystallographic data and assisted with troubleshooting molecular replacement and refinement during my candidature. Professor Tierney DL and Associate Professor Jeffrey Harmer assisted with the collection and manipulation of EPR data. Professor James L. Larrabee assisted with the collection and manipulation of MCD data.

Statement of parts of the thesis submitted to qualify for the award of another degree

None

Acknowledgements

There are a number of people I would like to acknowledge and thanks for their guidance, support and technical expertise that have enabled me to complete my studies.

First and foremost, I would like to thank my primary supervisor Prof. Gary Schenk. Thankyou for providing me with the opportunity to study within your lab. You have a true talent in providing support, and you did on numerous occasions when I was lacking direction and perspective. You have shown me a leadership style, which I will endeavour to assimilate into my own. It is my hope that we stay in contact moving forward.

To Dr Marcelo Pedroso, you have had the daunting task of moulding me from an explosives chemist into a biochemist. Although you may not think so, you have incredible mentorship skills and this was one of the primary reasons I have been able to make it to this point. I respect your opinions, both scientifically and otherwise, and have really appreciated your company over a mexican lunch or two. Thankyou for the significant time and effort you have put into me and my development as a scientist, I will be forever grateful.

I would like to thank some of the research groups and individuals that have assisted me with the various techniques I have utilized during my candidature. Thanks to Prof. Luke Guddat for his assistance and mentoring in the field of enzyme crystallography. Thanks to James Larrabee for your hospitality and guidance during my trip to your lab in the USA to collect MCD data. Thanks to Prof. Tierney DL and Associate Prof. Jeffrey Harmer who have assisted me with the collection and manipulation of EPR data.

I would like to thank my Undergraduate chemistry staff from the Australian Defence Force Academy for providing me with the knowledge and skills to succeed in my studies of chemistry. More specifically, I would like to thank Prof. Lynne Wallace for sparking an interest in chemistry that has evolved into my career.

I would like to thank all the SCMB staff, along with acknowledging the financial support provided to me from the Commonwealth Government (APA Scholarship), and the Graduate School ‘Gibbins’ Travel Award which enabled me to travel to the USA for my research.

I would like to thank my wife, Jessica, my brother James, and my close mates who have always provided an abundance of support and motivation during the entirety of my candidature.

Keywords

organophosphate, phosphoesterase, binuclear metallohydrolase, magnetic circular dichroism, stopped-flow fluorescence, kinetics, electron paramagnetic resonance, beta-lactamase, phosphatase, transitions state.

Australian and New Zealand Standard Research Classifications (ANZSRC)

ANZSRC code: 060101, Analytical Biochemistry, 20%

ANZSRC code: 060112, Cell Metabolism, 60%

ANZSRC code: 060199, Biochemistry and Cell Biology not elsewhere classified, 20%

Fields of Research (FoR) Classification

FoR code: 0302 Inorganic Chemistry 25 %

FoR code: 0601 Biochemistry and Cell Biology 25 %

FoR code: 0306 Physical Chemistry (incl. structural) 50 %

Table of contents

List of figures

List of tables

List of equations

List of abbreviations

Aim-1	Adelaide Imipenemase number 1
BJP	Bradyrhizobium japonicum Enzyme
bla	β-Lactamase (use to designate a gene)
BLAST	Basic Local Alignment Search Tool
BMH	Bimetallic Metallo Hydrolase
CCP4mg	Free graphic software
Clustal	A software program to analyse and compare sequences
CphA	Carbapenem hydrolysing and first (‘A’) from Aeromonas hydrophila
CpsB	Streptococcus pneumoniae Phosphotyrosine Phosphatase
EDTA	Ethylenediaminetetraacetic acid (a chelator)
EI	Enzyme-Inhibitor complex
EPR	Electron paramagnetic resonance
EPR	Electron paramagnetic resonance
ES	Enzyme-Substrate complex
ESI	Enzyme-Substrate-Inhibitor complex
FEZ-1	Legionella (Fluoribacter) gormanii endogenous zinc β-lactamase
GpdQ	Glycerophosphodiesterase enzyme
IPTG	Isopropyl β-D-1-thiogalactopyranoside
ITC	Isothermal titration calorimetry
K	Equilibrium
k_1	Forward rate of reaction
k_{-1}	Reverse rate of reaction
k_{cat}	Turnover number
kDa	Kilodaltons
K_i	Inhibition constant
K_{ic}	Competitive Inhibition constant
K_m	Michaelis constant
k_{obs}	Observed rate of reaction
L1	Labile enzyme from Stenotrophomonas (Pseudomonas, Xanthomonas)
LRA-8	Lactamase resistance from Alaskan soil number 8
MBL	Metallo-β-lactamase
MCD	Magnetic circular dichroism

MIM-1	Maynooth Imipenemase number 1
MIM-2	Maynooth Imipenemase number 2
NDM-1	New Dehli Metallo-β-lactamase number 1
OP	Organophosphates
OpdA	Organophosphate-degrading enzyme from Agrobacterium radiobacter
PAP	Purple Acid Phosphatase
PDB	Protein Data Bank
SIM	Salmonella Imipenemase
SMB-1	Serratia metallo-β-lactamase
SPR-1	Serratia Proteamaculans MBL
VTVH	Variable temperature, variable field MCD
μOH	Water/hydroxide molecule bridging a binuclear metallic centre

Chapter 1
Introduction

1.1 Bimetallic metallohydrolases

Bimetallic metallohydrolases (BMH) are a large group of enzymes that are characterised by an active site that contains divalent metal ions (≤4 Å apart) that play a pivotal role in the hydrolysis of ester and amide bonds of a range of substrates [1,2]. While diverse BMHs may vary greatly in their polypeptide sequence and biological functions, their active site geometries tend to be rather conserved (Figure 1.1). A typical active site geometry for theses enzymes include two divalent metal ions that are mainly coordinated by nitrogen atoms from histidine residues, or oxygens from aspartates. The coordination spheres generally also contain several water/hydroxide molecules in terminal and/or metal ion-bridging positions. The majority of BMHs utilise metal ion-bound hydroxides as nucleophiles to initiate the hydrolytic reaction. Several examples of active sites of BMHs are shown in Figure 1.1. In the case of the β-lactam antibiotic-degrading metallo-β-lactamases (MBL; for illustration a member from the B3 subgroup was selected - see below for more details) the two Zn^{2+} ions in the active site are bridged by the nucleophilic hydroxide [3]. In purple acid phosphatase (PAP), the only BMH where the necessity for a heterobinuclear metal centre of the form Fe^{3+}-M^{2+} (with M = Fe, Zn or Mn) has been established, the two metal ions are also bridged by a hydroxide in addition to an oxygen from an aspartate residue. The hydroxide may also act as reaction-initiating nucleophile in PAP, but other candidates are possible, depending on the metal ion composition and substrate used in the reaction [4]. In some organophosphate (OP)-degrading BMH, including the enzyme from *Agrobacterium radiobacter* (OpdA), the metal ion-bridging hydroxide acts as nucleophile, while a carboxylated lysine residue stabilises the active site structure [5]. In contrast to MBL or PAP, OpdA and related enzymes are rather promiscuous with respect to metal ions they require to promote catalytic activity.

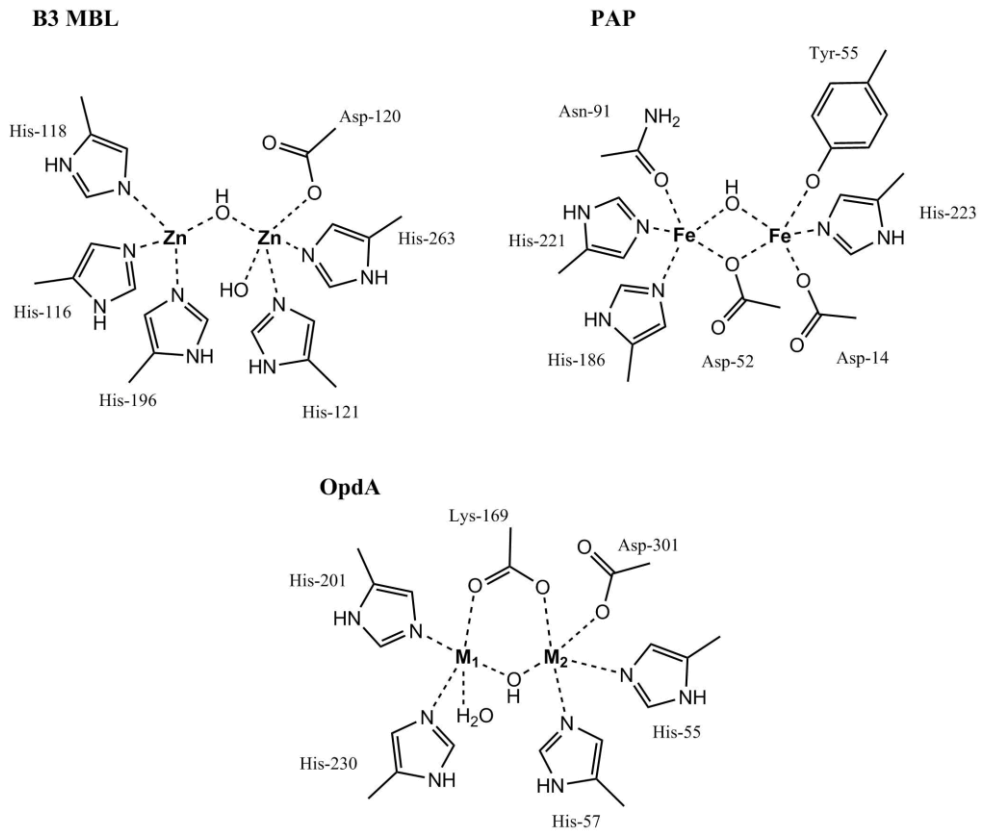

Figure 1.1: Active site geometries of selected BMHs, all relevant to this thesis. They include MBLs (top left), PAPs (top right) and OpdA (bottom) [6-9].

BMHs play important roles in numerous metabolic pathways and an increasing number of these enzymes have become important in the development of chemotherapeutics to treat various human ailments. MBLs, for instance, are major contributors to the emergence and spread of antibiotic resistance, but to date no clinically relevant inhibitors have been developed to combat their activity [10,11]. In contrast, OP-degrading BMHs have a strong potential to be used in bioremediation applications. OpdA is commercially sold by Orica as an agent that is efficient in breaking down pesticides in agricultural areas [12].

1.2 Selection and function of metals in BMHs

In general, the function of metals in enzymes can be structural, catalytic or both. In addition, metal ions may provide suitable binding partners for substrate molecules. The selection of metal ions may vary between different BMHs, with some of these enzymes displaying a stringent requirement for a particular metal ion (*e.g.* urease for Ni^{2+}) [13,14] while others are far more promiscuous (*e.g.* OP-degrading BMHs) [12]. Furthermore, some BMHs such as MBLs appear to require Zn^{2+} *in vivo*, however, *in vitro* activity can be reconstituted with a range of other divalent metal ions [15]. Such metal ion replacements are frequently exploited in functional studies where the catalytic and spectroscopic properties of different metal ion derivatives of an enzyme are compared to probe its mechanism of action. In this thesis, I will employ this methodology to investigate the mechanism of MBLs.

All the enzyme systems studied in this thesis (*i.e.* MBL, PAP, OpdA) are active in the presence of Zn^{2+}. Zinc is essential for the growth and development of most forms of life on earth. It is the second most prevalent metal (second only to iron) in the human body and is essential to numerous biological functions, often associated with proteins. Unlike other first row transition metal ions Zn^{2+} is unique in that it contains a full d orbital (d^{10}) and as such it is diamagnetic. Zn is able to form tetrahedral, octahedral or trigonal bipyramidal complexes, with the latter being the most common geometry found in metalloenzymes [3]. The most common ligands in proteins are histidine residues [16-19].

1.3 Mechanisms of hydrolysis

The exact molecular details of the mechanism employed by BMHs can be quite diverse between different groups of enzymes, and sometimes even within the same group. For example, for PAPs it could be shown that the identity of the reaction-initiating nucleophile may change as a function of the metal ion composition of the active site, the pH of the reaction and the identity of the substrates [20,21]. Similar observations were reported for the OP-degrading BMHs OpdA and glycerophosphatediesterase from *Enterobacter aerogenes* (GpdQ) [22,23]. With respect to MBLs mechanistic variations are reported within different subgroups, and even within a particular enzyme it appears that more than one mechanistic strategy may be available (see below for more details). This mechanistic flexibility may also be associated with a functional promiscuity frequently observed with BMHs; indeed, it has been speculated that the incorporation of alternative metal ions may serve as evolutionary triggers to adapt enzymes for new functions [24]. As an example, two recently discovered MBL-like enzymes from the marine organisms *Novosphingobium pentaromativorans* and *Simiduia*

agarivorans, MIM-1 and MIM-2, respectively, are introduced here. The two enzymes were discovered due to their sequence homology to known members of the MBL family [25]. Indeed, both enzymes emerged as potent β-lactam antibiotic-degrading enzymes [26], but they were equally efficient as enzymes in quorum-sensing networks, potentially with Zn^{2+} favouring the lactamase activity and Ca^{2+} the quorum sensing-related one [26]. However, despite variations in the details of the mechanism employed common to the large majority of BMH is that a metal ion-activated hydroxide initiates the catalytic reaction. Figure 1.2 illustrates this principle with a few specific examples.

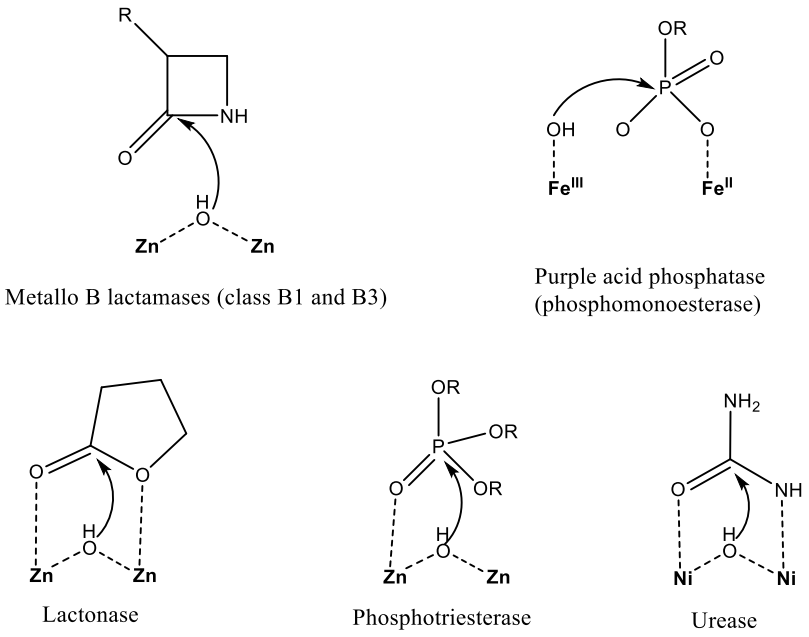

Figure 1.2: Simplified mechanism of selected metallohydrolases [1].

1.4 Phosphatases

Phosphatases constitute a large family of enzymes that play crucial roles in numerous metabolic pathways, including energy conversion, signalling and DNA replication [27]. Many of these phosphatases are metal ion-dependent. While phosphatases are capable of hydrolysing the phosphate ester bonds of a large array of biologically relevant molecules, some of these enzymes are also efficient in catalysing the hydrolysis of synthetic (*i.e.* non-natural) organophosphates (OPs). Such OPs have become widely utilised as plasticizers and pesticides, while others are used as nerve agents in chemical and biological warfare [28,29]. Especially their use as pesticides is of utmost relevance to the global bio economy as they guarantee an expansion of agricultural food production to provide sufficient food for a rapidly growing population. However, the use of OPs as pesticides has not been without risk. Due to their significant toxicity they pose a serious threat to environmental health, and due to their chemical stability they can persist and accumulate in ground water [30,31]. If not monitored

and controlled properly these pesticides may enter the drinking water and it is thus no surprise that the estimated death toll associated with their ingestion is estimated in the hundreds of thousands, largely in the developing world [32]. The toxicity of these OP pesticides originates from their potent inhibition of the enzyme acetyl cholinesterase in the nervous system [33]. A recent report from the United Nations states that pesticides "impose substantial costs on Governments and have catastrophic impacts on the environment, human health and society as a whole", yet industry (an estimated 50bn net worth in 2017) continue to argue that pesticides are required to "feed a growing world" [34]. Fortuitously, some soil-dwelling microorganisms have evolved the enzymatic machinery to degrade such organophosphates; these OP-degrading phosphatases thus provide a promising avenue to develop a biocatalytic tool to control pesticide levels and destroy them in an efficient yet "green and clean" way [35-41]. OpdA, mentioned above, is one of the most efficient OP-degrading enzymes. I will elaborate further on this enzyme in Chapter 3. In Figure 1.3 several OP pesticides and nerve agents are shown; also included are two OP substrates that are frequently used as convenient substrates for functional studies on phosphatases, *i.e.* the monoester *para*-nitrophenyl phosphate (*p*NPP) and its diester homolog bis*p*NPP.

Synthetic OPs used in agriculture or warfare are mainly phosphotriesters and enzymes such as OpdA evolved to be rather specific for such substrates [12]. However, other phosphatases have evolved to hydrolyse the P-O bonds of mono-, or diester substrates. Examples of predominantly monoester phosphatases include PAPs [42-47] and CpsB from *S. pneumoniae* [48,49]. PAP and CpsB will be discussed in more detail in Chapters 2 and 6, respectively. The enzyme GpdQ from *E. aerogenes* [50], mentioned above is predominantly a diesterase, but it demonstrates considerable promiscuity by being capable of hydrolysing a range of tri- and monoester substrates as well [23,51].

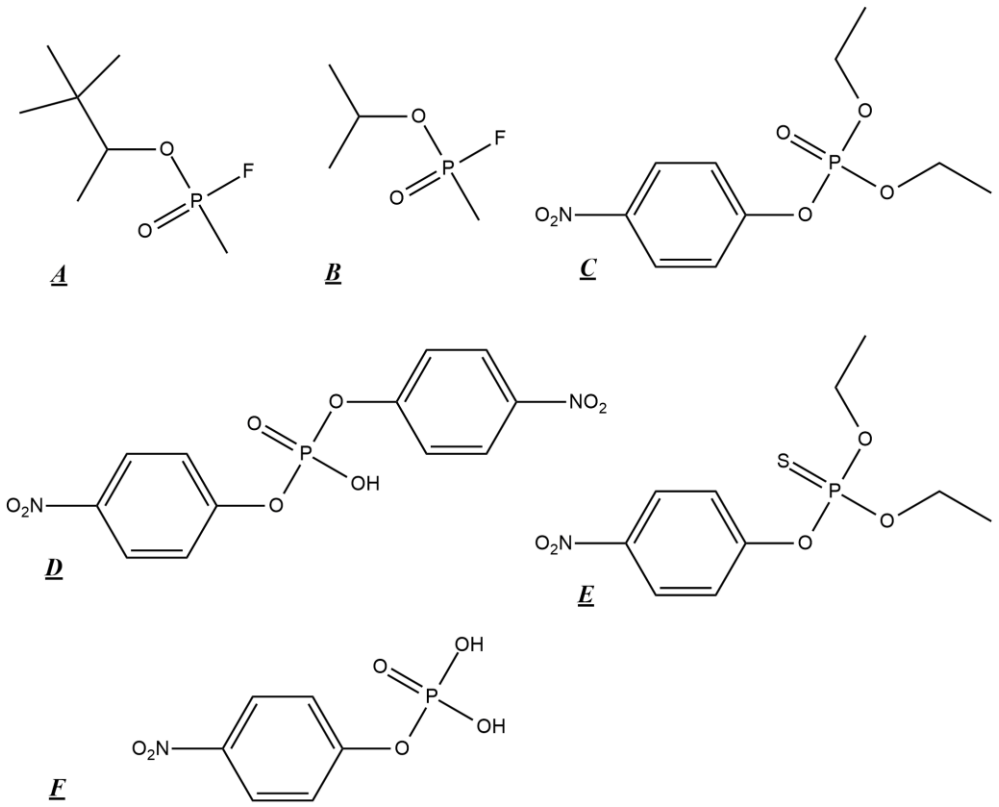

Figure 1.3: Select phosphate ester substrates; A- soman, B- sarin, C- paraoxon, D- bis(p-nitrophenyl)phosphate, E- parathion, F- p-nitrophenylphosphate (1).

Common to the mono-, di- and triesterases introduced above is that they contain a bimetallic metal centre in their catalytically active site. The only potential variant may be the enzyme CpsB, which, according its crystal structure, may use three closely spaced metal ions to maintain its catalytic function (Figure 1.4). However, as will be discussed in Chapter 6, only two of these metal ions play an active role in CpsB, while the third metal (M3 in Figure 1.4) represents an artefact of the crystallisation procedure.

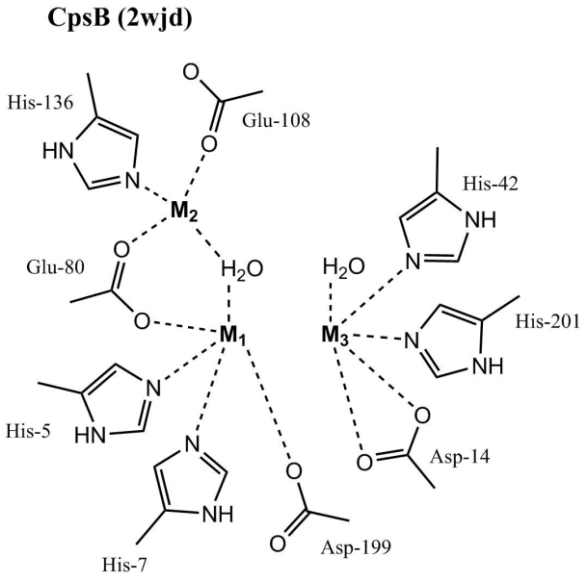

Figure 1.4: Active site of CpsB based on crystallographic studies shows three metal ions bound in the active site [52].

1.5 Antibiotic-degrading enzymes – Is the age of antibiotics coming to an end? Current trends in resistance

While this thesis focuses on the function and mechanism of a series of BMHs that differ in their substrate preference the group that has attracted the most significant attention in recent years is the one that comprises the β-lactam antibiotic-degrading MBLs. The reason why these enzymes have gained notoriety is outlined in the remaining sections of this introduction. Before the discovery of the β-lactam penicillin by Alexander Fleming in the 1920's a simple prick from a rose thorn could lead to a potentially lethal infection [52]. Since the introduction of penicillin and its various derivatives (which constitute more than 60% of all currently used antibiotics), infections linked to diseases such as pneumonia, tuberculosis, syphilis and gonorrhoea can be treated. However over- and misuse of antibiotics has led to the gradual development of resistance and we are now faced with the real threat that infections that have been controllable since World War II become dangerous once again. Sadly, Alexander Fleming himself predicted such an outcome long ago: 'the public will demand [the drug and]…then will begin an era…of abuses. The microbes are educated to resist penicillin and a host of penicillin-fast organisms is bred out which can be passed to other individuals and perhaps from there to others until they reach someone who gets a septicaemia or a pneumonia which penicillin cannot save. In such a case, the thoughtless person playing with penicillin treatment is morally responsible for the death of the man who finally succumbs to infection with the penicillin-resistant organism. I hope the evil can be averted' [53].

Antibiotics are, however, not only used in a medicinal context. It is common practice to add antibiotics to food supplies for livestock to prevent disease. In 2015 it was reported that up to 80% of the antibiotics used in the US were administered to animals via either direct (treatment) or indirect (preventative) methods. Of these antibiotics, a significant number of them are clinically relevant for the treatment of infections in humans [(54)]. Administering antibiotics in this fashion to livestock is akin to a large scale petri dish where microbes are exposed to low grade antibiotics, which essentially encourages bacteria to become resistant. When one considers the scale on which this form of experiment is being conducted it is little surprise that resistance is on the rise. Resistant bacteria can pass through their hosts (pigs, chickens, cattle) and end up in manure, which then is widely distributed as fertiliser. From there resistant bacteria may accumulate in soil, or leeches into waterways, thus promoting the distribution of resistance on a large scale. A recent study illustrated the grave significance of this cycle; the profiles of over 23,000 bacterial genomes demonstrated how antibiotic resistance genes can be transferred from bacteria in food animals to bacteria native to the human stomach [(55)]. This cycle affects the entire global resistome and its long-term effect on the environment, if not controlled urgently, will be devastating.

The current arms race for supremacy over resistant pathogens does not appear to run in our favour. At the very least it appears that the rate of resistance is equal to or higher than the rate of development of new and more effective antibiotics. For example, rises in resistance to penicillin led to the introduction of carbapenem antibiotics to treat particularly resistant bacteria. However, today an increasing number of pathogenic organisms have become resistant to all known forms of clinical antibiotics. Not only is the rise in resistance alarming for health reasons, but the rate at which resistance is increasing makes the development of new antibiotics less financially viable for large pharmaceutical companies. 10-15 years and millions of dollars in research into novel FDA approved antibiotics that quickly become irrelevant is not financially sustainable for any pharmaceutical company.

So how large is the problem of antibiotic resistance today? The Center for Disease Control (CDC) reports that ‘in America alone at least 2 million become affected with antibiotic resistant bacteria and at least 23,000 people die as a direct result of these infections’. The CDC has made efforts to track trends in resistance, focusing on emerging and particularly dangerous threats. These include but are not limited to *Clostridium difficile* (CDIFF), which caused 15,000 deaths in the USA in 2015, *carbapenem-resistant Enterobacteriaceae* (CRE) bacteria, NDMs from *Klebsiella pneumonia* and *Escherichia coli* and, most recently, multi-resistant MCR-1 found in a patients in numerous countries

[56-62]. Moving forward, efforts are being made by researchers around the globe to find novel strategies in an effort to make resistant bacteria sensitive to antibiotics once again. A major target for such strategies is a group of enzymes that is very efficient in hydrolysing and thus inactivating β-lactam antibiotics, the β-lactamases.

1.6 β-lactamases and their function

β–Lactamases catalyze the hydrolysis of the four-membered β-lactam ring, the characteristic feature of many commonly used antibiotics such as penicillins, carbapenems, cephalosporins and monobactams (Figure. 1.5). These compounds are very effective in impeding the enzymes involved in the generation of peptidoglycans in the cell wall of pathogenic bacteria [3,7,63-65]. In Gram negative bacteria, β-lactam antibiotics invade bacteria via passing through the cell membrane and cell walls. Once inside the cell, β- lactams disrupt cell wall biosynthesis by targeting the enzymes responsible for peptidoglycan synthesis. β-Lactamases prevent this process by hydrolysing β-lactams before they become toxic to the host bacteria (Figure 1.6) [19].

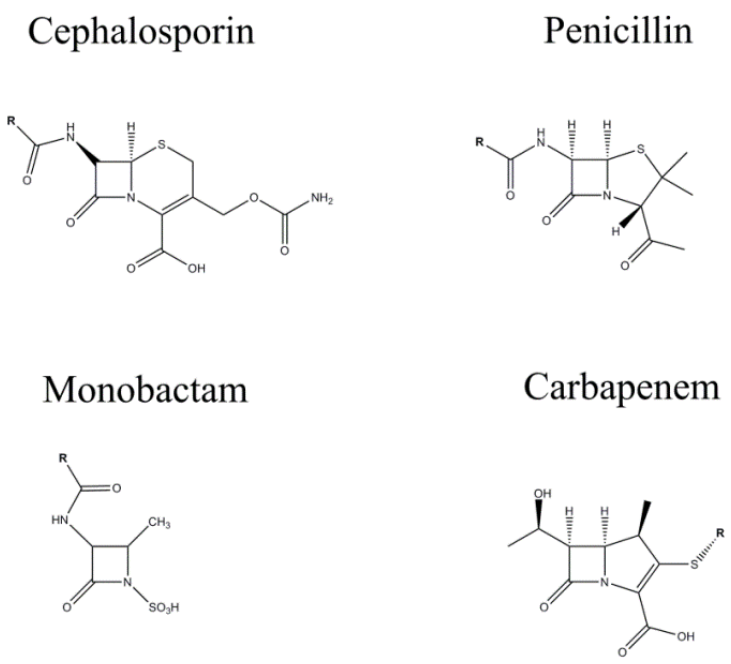

Figure 1.5: Classes of β-lactam antibiotics.

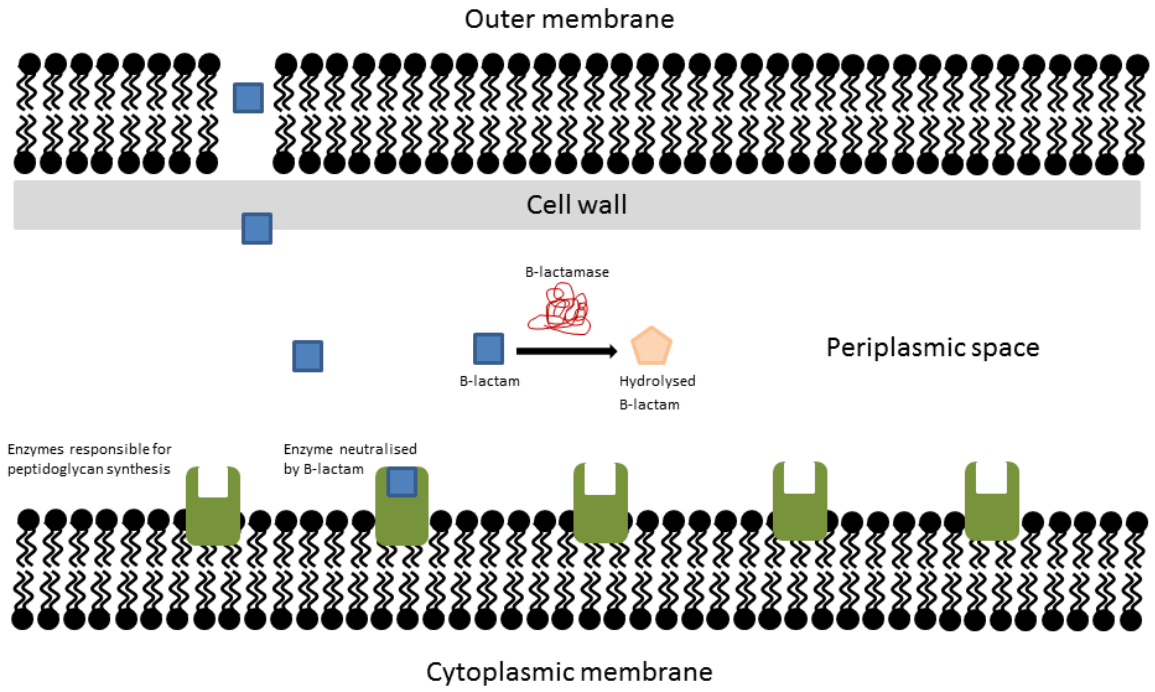

Figure 1.6: β-lactamase activity within gram negative bacteria. β-lactam antibiotics diffuse across the cell outer membrane and cell wall, then neutralise peptidoglycan synthesizing enzymes. β-lactamases render b-lactams inactive through hydrolysis [19].

β-Lactamases are divided into four groups based on their mechanism of hydrolysis and cofactor requirements [66]. Groups A, C and D are serine-β-lactamases (SBLs), which employ a serine residue to initiate the hydrolysis of the β-lactam ring (*i.e.* its opening), whilst group B contains the MBLs, which require either one or two metal ions in their active site as essential cofactors for catalysis [3,7,65,67,68].

SBLs have been extensively studied and mitigation strategies in the form of co-administered inhibitors like clavulanic acid have been proven to be effective in clinical use. Unfortunately, unlike for SBLs there are no clinically viable MBL inhibitors available. With increasing trends in resistance and declining interest among the major pharmaceutical companies in research into new antibiotics, novel MBL inhibitors are urgently needed combat these enzymes directly. To date, the most efficient (non-clinical) leads are thiol [69-73], carboxylate [74] or tertazole [75] compounds. Crystal structures for MBL-bound thiol based inhibitors such as captopril and thioglycolic acid provide insights into inhibitor binding. For both these compounds, crystal structures with the B3 MBLs L1 and SMB

support a binding mode in which the sulfur of the inhibitor displaces the bridging hydroxide between the two Zn in the active site [70,71,76]. This represents a competitive type of inhibition. Unfortunately, neither compound is clinically relevant, with captopril being a medication for treating hypertension and it is unsafe for patients suffering from ailments such as congestive heart failure, kidney problems caused by diabetes, and heart attack recovery [77]. It is especially dangerous for pregnant women as it can lead to death of the unborn child [78].

1.7 Metallo β Lactamases

The first MBLs were discovered by Sabath and Abraham in 1966 in a strain of *Bacillus cereus* [79]. This was followed with the discovery of numerous chromosomally encoded MBLs, however, in 1990 the discovery of MBLs on mobile genetic elements within *P. aerguinosa* and *B. fragillis* represented the beginning of the increasing trend of resistance we are battling today [80]. Wide spread horizontal dissemination of resistant genes is a reality as seen by the rapid spread of MBLs such as IMP, VIM and NDM globally [81]. *P. aerguinosa* has been identified by both the World Health Organisation and the C DC in America as one of the most dangerous pathogens currently in circulation, with in the excess of 51,000 infections per year, resulting in over 440 deaths [7,63,82]. The primary treatment option for this pathogen has been the use of carbapenem antibiotics since the 1980s [83]. However, this bacterium has evolved the machinery to produce lactam-degrading proteins including the recently discovered "Adelaide Imipenemase-1" (AIM-1) in an aboriginal patient in Adelaide, Australia [7,63]. Structural, mechanistic, spectroscopic and kinetic investigations of AIM-1 are a particular focus of this thesis (Chapter 5).

The MBL-encoding genes can reside on either mobile genetic elements that can readily be shared between bacteria, or can be chromosomally encoded within the bacterium. Zinc-dependent MBLs share minor structural similarities to SBLs and typically have a broad substrate profile, hydrolysing almost all known β-lactams. They are further divided into as many as four sub-groups, *i.e.* B1, B2, B3 and B4, depending upon their sequence homology and metal ion requirements for hydrolysis [3,84]. However, all MBLs do share a characteristic αββα fold as seen in Figure 1.7 [3,7,65].

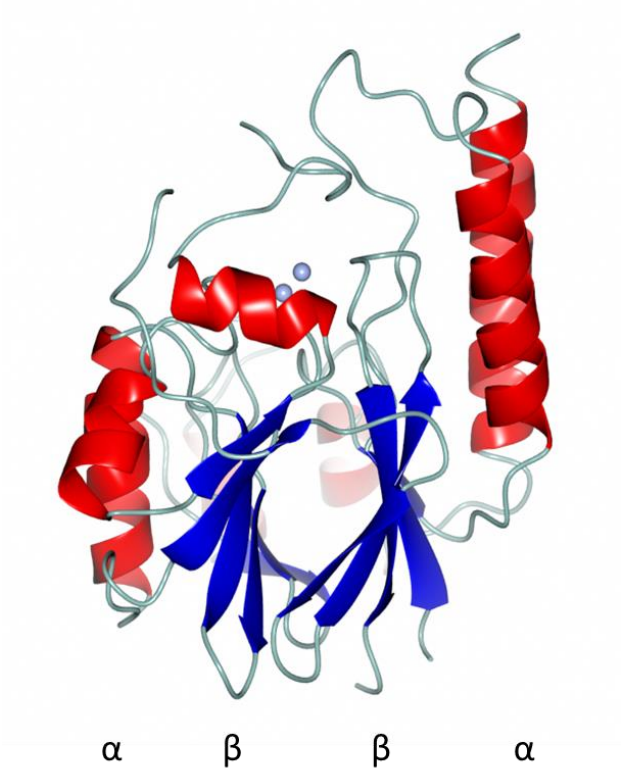

Figure 1.7: The characteristic αββα fold, illustrated using the MBL MIM-2 from S. agarivorans (see Chapter 4 for the structural investigation of this enzyme)

The B1 subclass MBLs require two Zn^{2+} metal ions for catalytic activity [3,65,67,68,85], although at least the MBL from *B. subtilis* (BcII) was shown to be partially active in the mononuclear form [86]. This subclass of enzymes is currently the most prevalent clinically, and hence, has been the most extensively studied. Members include IMP from *P. aeruginosa* [74,87-89], VIM from *K. pneumoniae* [90-95], NDM from *K. pneumoniae* [58,59,96-102] and BcII from *B. cereus* [103-107]. The binding of substrates within this class of MBLs is believed to be affected by two peptide loops within close proximity of the metal ions and the extended N-terminus (Figure 1.8), defining the active site pocket [65].

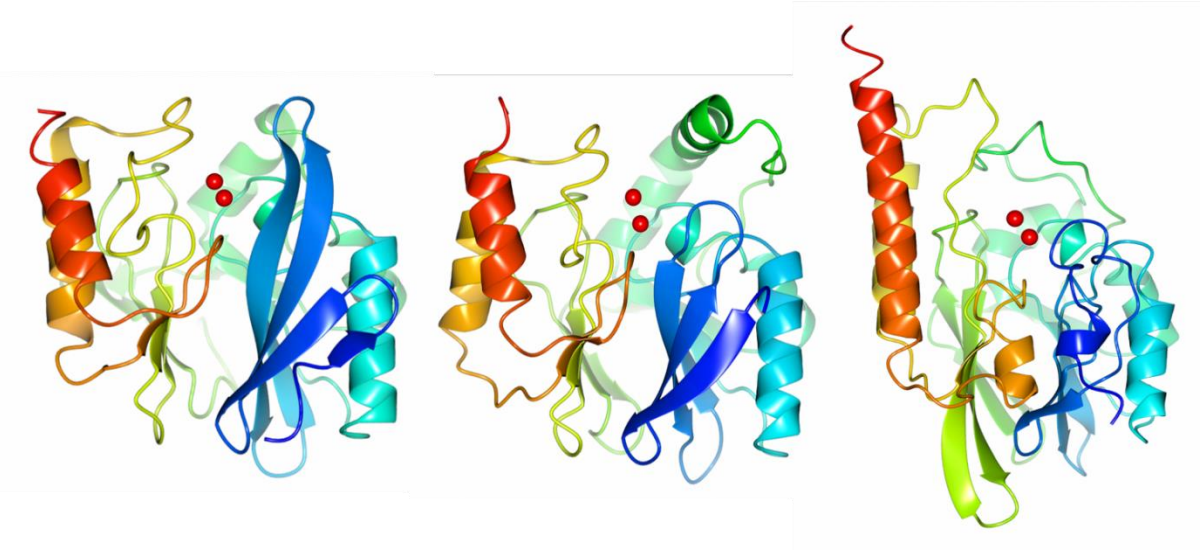

Figure 1.8: Representative ribbon structures for MBLs: Class B1 (left – NDM-1, pdb:3ZR9) [108], B2 (middle –CphA, pdb:3F9O) [109] and B3 (right – MIM-1; see Chapter 4). Structures are coloured by gradient extending from the C terminus (red) to the N terminus (blue).

In contrast, B2-type MBLs require only one metal ion in their active site for optimal catalytic activity; the binding of a second metal ion leads to the inactivation of the enzyme [3,110]. Homologous families within the B2 subclass include CphA from *A. hydrophilia* [109,111-117] and SfH from *S. fonticola* [118,119]. Unlike B1 MBLs, B2 enzymes have an extended α-helix in the loop 2 position that defines the active site pocket, making them particularly narrow in geometry (Figure 1.8). Consequently, these MBLs are more selective for their preferred substrates, displaying specific activity towards monobactams, a group of substrates that is poorly inactivated by other MBLs [3,110,111,114].

B3-type MBLs are similar to B1 enzymes in requiring two metal ions in their catalytic site to be fully active; however, their active site architecture is quite different as can be seen in Figure 1.8 [7]. Both loop 1 and 2 regions differ considerably from those seen in B1 and B2 MBLs, and especially in the case of MIM-1, it is proposed that an arginine residue (Arg46) located in the N-terminus may have an active role in substrate recognition, which is elaborated on further in Chapter 4. Currently, there are over 151 proteins within the B3 subclass, with more than 39 associated crystallographic structures; however, this number is steadily rising[120]. Examples of enzymes form this subclass include: L1 from *S. maltophilia* [76,121-128], SMB from *S. marcescens* [70,71], BJP from *B. japonicum* [129,130], FEZ from *F. gormanii* [131-134], LRA and Rm3 from functional metagenomic studies [135,136], AIM from *P. aeroginosa* [7,72,137], MIM-1 from *N. pentaromativorans* and MIM-2 from *S. agarivorans* [26]; LRA, AIM and the two MIMs will be discussed in more detail in subsequent chapters (*i.e.* Chapters 4, 5 and 6).

One MBL, expressed by *S. proteamaculans* (SPR-1), may belong to the proposed B4 subgroup. The metal ion requirement of SPR-1 is different from the other MBLs; in its resting state the enzyme appears to bind only one Zn^{2+}, however, upon interaction with a substrate, a bimetallic centre is formed that is catalytically active [138]. The substrate-initiated binding of a catalytically important metal has been seen before for the phosphatase GpdQ from *E aerogenes* [3,23,51,122,139-145].

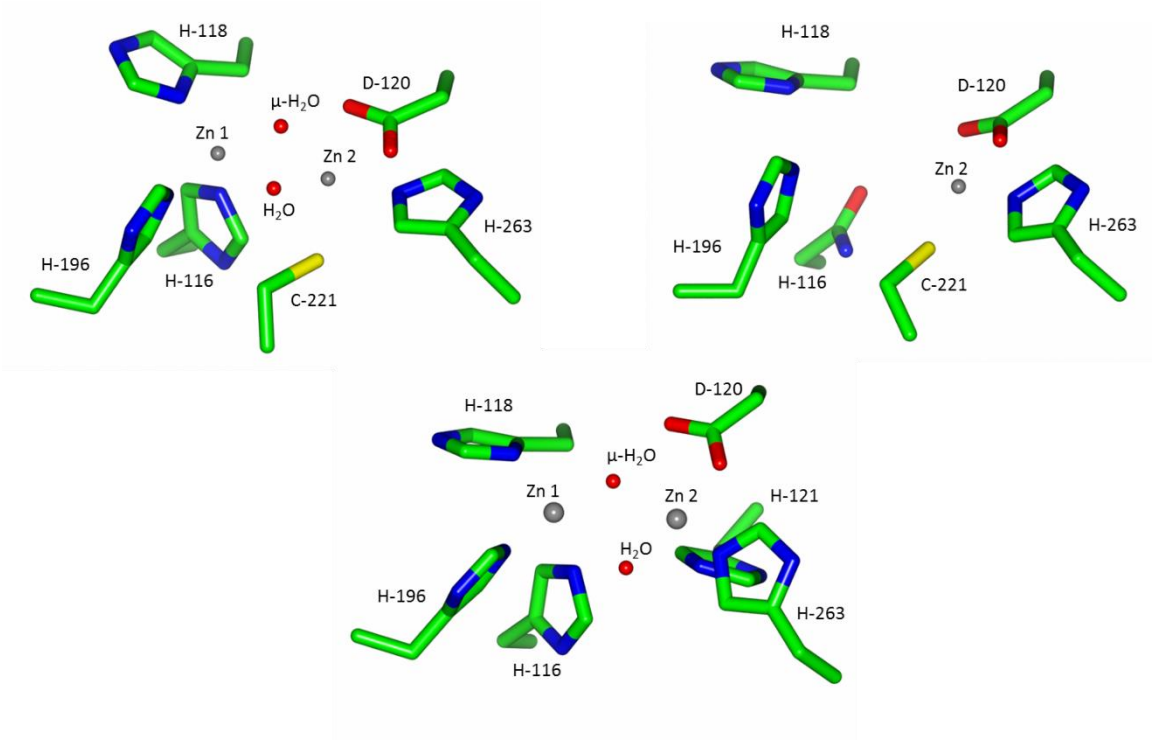

Figure 1.9: MBL active sites – B1 (top left), B2 (top right) and B3 (bottom centre)

Table 1.1: Zn coordination and associated geometries of MBLs from the different subgroups

Subclass	Zn1 Ligands	Zn1 Geometry	Zn2 Ligands	Zn2 Geometry
B1	His116, His118, His196 & µW1	Tetrahedral	Asp120, Cys221, His263, µW1 & W2	Trigonal bipyramidal
B2	Not occupied in active form of the enzyme	-	Asp120, Cys221, His263	Tetrahedral
B3	His116, His118, His196 & µW1	Tetrahedral	Asp120, His121, His263, µW1 & W2	Trigonal bipyramidal
B4	His116, Arg118, His196 µW1 (upon Zn2 binding)	Tetrahedral	Asp120, Gln121⁄Ser221, Ala262 µW1 (upon Zn2 binding)	Trigonal bipyramidal

Figure 1.9 and Table 1.1 illustrate the relevant Zn-ligand interactions seen for MBLs from different subgroups. Whilst B1- and B2-type MBLs have identical ligands for the Zn2 binding site, they differ in the Zn1 metal centre. In contrast, in B3 MBLs Cys221 in Site 2 is replaced by a histidine (His121), but their Site is identical to that of B1 MBLs. In both B1 and B3 MBLs Zn1 and Zn2 are bridged by a water molecule (µ-H_2O; the likely nucleophile that initiates the hydrolysis) [7,65,95,122,146,147]. In contrast, B4 MBLs both metal binding sites differ from other MBLs.

Proposed mechanisms for both mononuclear (*i.e.* B2 subgroup) and binuclear (*i.e.* B1, B3 and B4 subgroups) MBLs have been published, with a common theme involving a nucleophilic hydroxide group that is either terminally bound (B2 MBLs) or bridging both metals (B1, B3 and B4 MBLs) [15,19,65,105,124,139,148-153]. Figure 1.10 illustrates simplified mechanistic schemes for both models using a truncated penicillin molecule as the substrate.

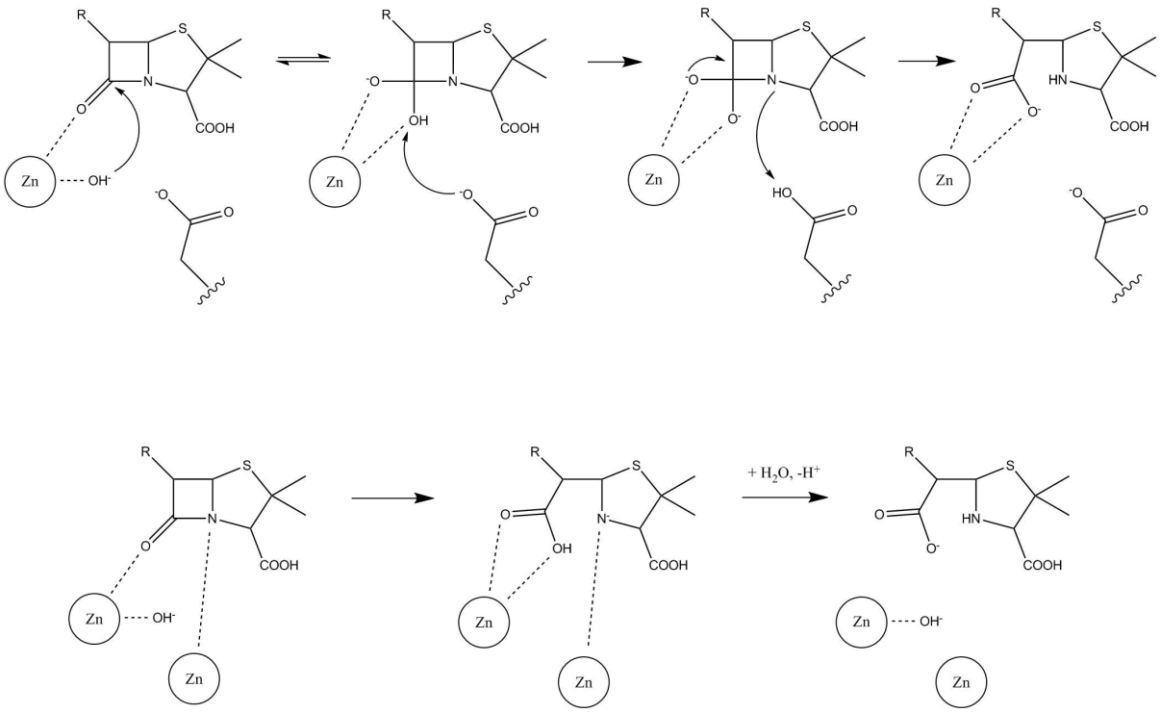

Figure 1.10: Proposed reaction mechanisms for mononuclear (top) and binuclear MBLs (bottom) [19].

1.8 Scope of this thesis

As illustrated in the preceding sections BMHs constitute a diverse group of enzymes, relevant to both medicinal applications as drug targets (*e.g.* MBLs, PAPs, CpsB) or biotechnology applications in form of catalysts that can break down and thus detoxify dangerous compounds in the environment (*e.g.* OpdA, GpdQ). In this thesis I employed a series of physico-chemical methods on these structurally and functionally distantly related enzymes to gain a better understanding into the factors that allow these biocatalysts to be highly efficient for their respective reactions. I envision that these insights can be translated either into successful strategies to develop clinically useful inhibitors, or modify some of these enzymes to be more suited for direct application in the environment. Specifically, the kinetic, spectroscopic, structural and crystallographic properties of PAP, OpdA, CpsB, AIM-1, MIM-1 and MIM-2 enzymes are explored with a view to provide insights into the mechanism of hydrolysis employed by these enzymes.

1.9 The aims of the project

The aims of this project include:

- Visualisation of the reaction trajectory and transition state in a hydrolytic reaction catalysed by the BMH PAP (Chapter 2).
- High resolution crystal structure of a fluoride-inhibited OP-degrading metallohydrolase (Chapter 3).
- Crystal structures of the B3 MBLs MIM-1 and MIM-2 from environmental microorganisms (Chapter 4).
- AIM-1: an antibiotic-degrading BMH that displays mechanistic flexibility (Chapter 5)
- Spectroscopic investigations of the structure and mechanism of the BMHs MIM-1, MIM-2, LRA-8 and CpsB (Chapter 6).
- General conclusions and future directions (Chapter 7).

Chapter 2

Visualization of the reaction trajectory and transition state in a hydrolytic reaction catalysed by a metalloenzyme.

Christopher Selleck, Daniel Clayton, Lawrence R. Gahan , Nataša Mitić, Ross P. McGeary, Marcelo Monteiro Pedroso, Luke W. Guddat, Gerhard Schenk.

[a]School of Chemistry and Molecular Biosciences, The University of Queensland, St. Lucia, Queensland, 4072, Australia

[b]Department of Chemistry, Maynooth University, Maynooth, Co. Kildare, Ireland

Corresponding Authors

G.Schenk: schenk@uq.edu.au L. Guddat: luke.guddat@uq.edu.au

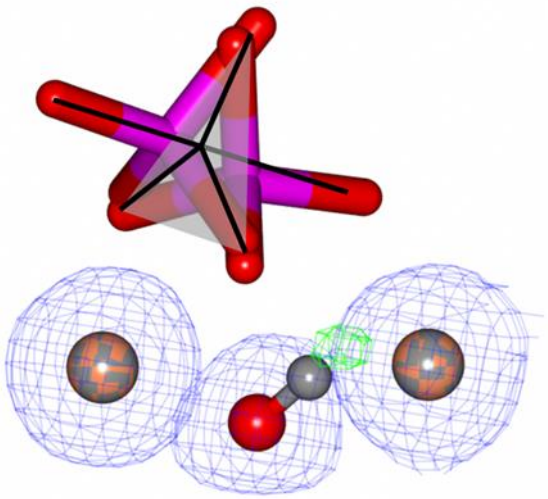

Figure 2.1 : Reaction trajectory in a metal ion-dependent hydrolase: A high resolution structure of a purple acid phosphatase (PAP) shows two binding modes for a substrate mimic. Their overlay provides unprecedented insight into the structure of the transition state of the reaction catalysed by this enzyme.

2.2 Abstract

Metallohydrolases are a vast family of enzymes that play crucial roles in numerous metabolic pathways. Several members have emerged as targets for chemotherapeutics. Knowledge about their reaction mechanisms and associated transition states greatly aids the design of potent and highly specific drug leads. Using a high-resolution crystal structure, we have probed the trajectory of the reaction catalysed by purple acid phosphatase, an enzyme essential for the integrity of bone structure. In particular the transition state is visualized, thus providing detailed structural information that may be exploited in the design of specific inhibitors for the development of novel anti-osteoporotic chemotherapeutics.

2.3 Keywords:

Metallohydrolase, phosphomonoester, phosphatase, transition state, metalloenzyme

2.4 Introduction:

Metal ion-dependent hydrolases (metallohydrolases) are a large family of enzymes that play a central role in numerous biological functions, including energy metabolism, signal transduction, biosynthesis and bone turnover [1,154,155]. An increasing number of these enzymes have become targets for the development of chemotherapeutics against a wide range of diseases. An example is the metallo-β-lactamases (MBLs), a family of Zn^{2+}-dependent enzymes that break down the most commonly used antibiotics, and are a major contributor to the emergence of antibiotic-resistant pathogens [150,156-158]. The development of promising drug leads that target a specific member within the metallohydrolase family is challenging because the catalytically relevant metal ion centre is often close to the surface of the protein, thus increasing the risk of low binding specificity. The design and synthesis of leads with high specificity for a particular target is, however, strongly aided by detailed information for the reaction mechanism and transition state(s) of this reaction.[159,160]

Here, we solved the high-resolution crystal structure (1.18 Å) of the metallohydrolase purple acid phosphatase (PAP) [161] from porcine uterus, and combined with previously reported structures of that enzyme individual steps for the transformation of a substrate to a product are tracked. In particular, this structure facilitates insight into the transition state of the reaction. PAP is able to hydrolyze a broad range of phosphomonoester substrates and plays a crucial role in bone metabolism; high levels of PAP in blood serum is a diagnostic marker for osteoporosis [162]. The identity of the preferred in

vivo substrate(s) of PAP is still unclear, but both ATP and ADP (but not AMP) are hydrolyzed effectively by this enzyme [163]. PAP is the only known metallohydrolase that requires a heterovalent dinuclear metal center of the form Fe^{3+}-M^{2+} (where M = Fe, Zn or Mn) in order to be catalytically active.[164] A distinctive characteristic feature of PAP is its purple color in concentrated solutions, which is due to a charge transfer transition between the Fe^{3+} and a tyrosine ligand in the active site (Figure 2.2) [161]. Importantly, the amino acid side chains that coordinate the metal ions are invariant in all PAPs and highly conserved among numerous members of the metallohydrolase family [1,154,161].

Despite the availability of detailed structural [8,165-169], kinetic [21,170-174] and spectroscopic [175-178] data, several aspects of the catalytic mechanism employed by PAPs remain obscure, including the mode(s) of substrate binding, the identity of the reaction-initiating nucleophile(s) and the nature of the transition state. The observation that PAP is also able to hydrolyze both ester bonds in some diester substrates in a processive (as opposed to sequential) manner demonstrates that the active site is capable of accommodating diverse substrates and that at least two different nucleophiles can be active [21]. Furthermore, metal ion replacement studies indicated that these nucleophiles do not necessarily need to be bound to one of the metal ions [174]. In the proposed transition state the phosphate group adopts the geometry of a five-coordinate trigonal bipyramidal oxyphosphorane, but its structure is yet to be visualized [167].

Our focus was on the elucidation of the likely transition state of the reaction catalysed by the di-iron pig PAP, using inorganic phosphate (Pi) as a probe. Pi is not only the smallest substrate mimic for PAP, but also the final product of the reaction as well as a mild competitive inhibitor of catalysis, with inhibition constants that are conserved across all known PAPs; reported Ki values are in the high micro- to low millimolar range [167,170-173]. This similarity in Ki values indicates that the binding mode of Pi is similar in different PAPs. Furthermore, rapid kinetics measurements demonstrate that the initial association between Pi and various PAPs is conserved [173,174], suggesting that this tetraoxo anion is a suitable agent to monitor the transformation of a substrate molecule to product.

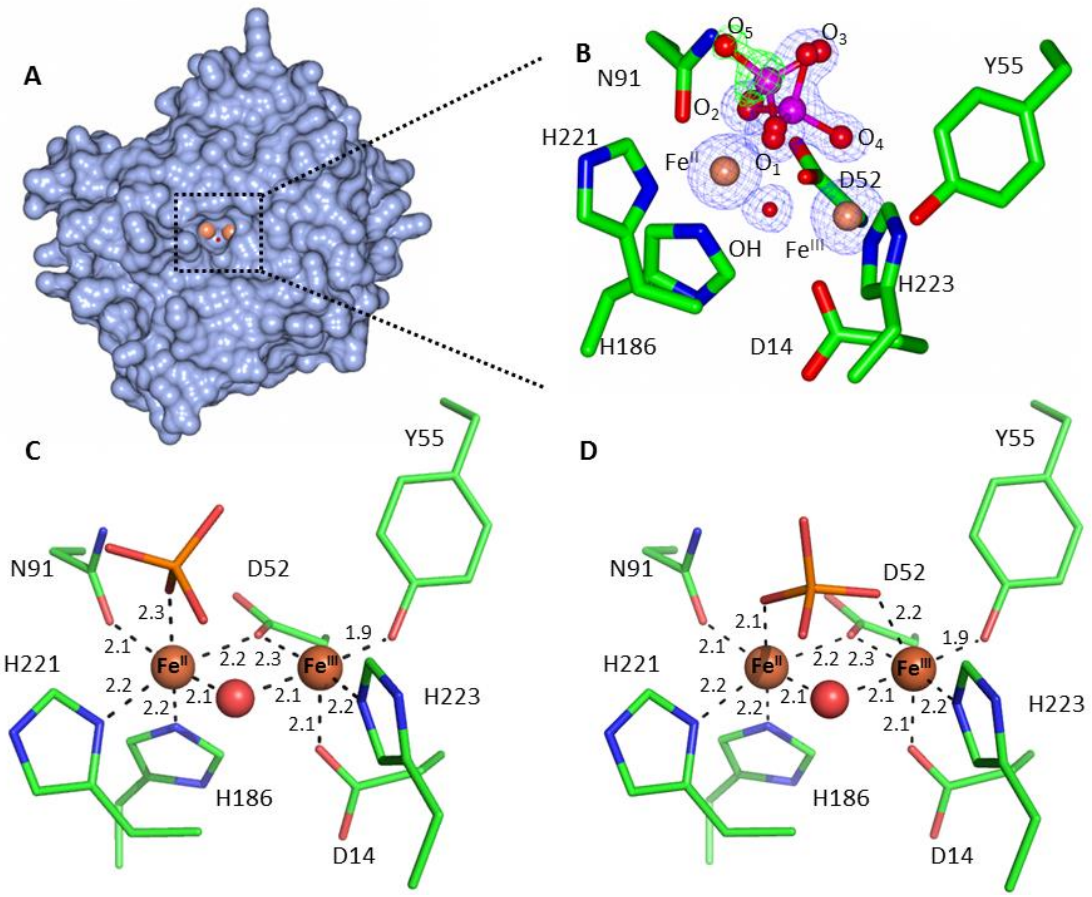

Figure 2.2: Structure of pig PAP at 1.18 Å. (A) Connolly surface showing the monomeric structure of the enzyme. Orange spheres indicate the presence of the metal ions in the active site. (B) Active site showing the electron density for the two metal ions, the μ-OH

2.5 Results

PAP was purified from the uterus of a pregnant sow using a previously published protocol [165]. The enzyme (66 mg/mL) was crystallized at 20°C using the hanging-drop vapor-diffusion method with crystallization conditions identical to those described previously. Specifically, at 5.0 the pH was close to the condition optimal for the catalytic activity of PAPs [165]. Crystallographic data were collected by remote access on beamline MX-2 at the Australian Synchrotron (Melbourne) using BLU-ICE [179].

The data were integrated, scaled and merged using HKL-2000 [180]. Refinement and model building were carried out using PHENIX 1.8.4 [181] and COOT 0.7 [182] respectively, using the previously published coordinates for pig PAP with PDB code 1UTE [165,183]. All atoms were subsequently refined with anisotropic B-factors; most hydrogen atoms were fitted as riding models, though the proton of the bridging hydroxide was added manually based on the electron density. Relevant crystallographic data and refinement statistics are summarized in Table 2.1. There is a single monomer of pig PAP in

the asymmetric unit with density for the presence of two Fe ions in the active site (Figure 2.2 A-B). Also well-defined within the active site is a bridging group we ascribe to a hydroxide ion and Pi in two alternative binding modes (discussed below) (Figure 2.2 C-D).

Table 2.1: Data collection and refinement statistics for PAP from porcine uterus.

Diffraction data	
Resolution Range (Å)	75.05 - 1.18
Observations (I>σ(I))	390,157 (45,794)
Unique reflections (I>σ(I))	98,587 (13,107)
Completeness (%)	91.3 (83.9)
Mean <I/σ(I)>	11.2 (1.7)
R_{merge}	0.068 (0.859)
R_{pim}[b]	0.037 (0.503)
Multiplicity	4.0 (3.5)
Crystal parameters	
Space group	*P*212121
Unit cell lengths (Å)	*a* = 63.12 *b* = 69.98 *c* = 75.05
Unit cell angles (°)	α = 90.0 β = 90.0 γ = 90.0
Refinement	
R_{work}[c]	0.1414
R_{free}[c]	0.1555
rmsd bond lengths (Å)	0.007
rmsd bond angles (º)	0.980
Ramachandran plot statistics	
Favoured regions	97.4
Outlier regions	0.00
PDB code	5UQ6

aValues in parentheses are for the outer resolution shell (1.25-1.18 Å). bRpim,; cRwork = Σ||Fobs|-|Fcalc||/Σ|Fobs|, Rwork is calculated based on the reflections used in the refinement (95% of the total data) and Rfree is calculated using the remaining 5% of the data.

The overall structure of pig PAP (Figure 2.3 A) is virtually identical to that described in a previous study of that enzyme [165]. The significance of the present structure is that it provides high-resolution insight into the active site and mechanistic features of PAP and related enzymes. Specifically, the metal ion-bridging oxygen appears to be protonated, as evidenced by residual difference density after the fitting of the oxygen atom (Figure 2.3 A-C). In support of this assignment is that this hydrogen atom is within H-bond distance of the phosphate oxygen atoms O1 and O4 (Figure 2.3). While this H-bond between the μ-OH group and P_i supports a role of this bridging ligand in substrate and/or product binding, and possibly also the stabilization of the transition state, it argues against the proposed role of this ligand as the hydrolysis-initiating nucleophile, at least under the conditions employed to crystallize pig PAP.

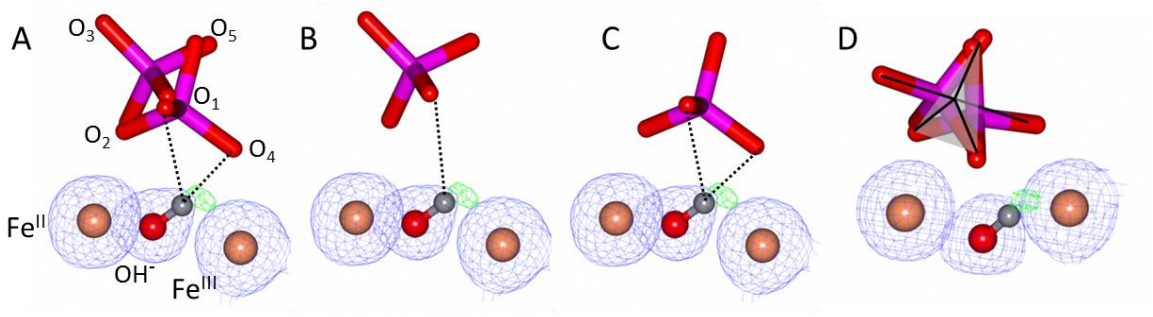

Figure 2.3: Phosphate coordination in the active site of pig PAP. In (A) both modes are shown, while in (B) and (C) the modes are deconvoluted. (D) Illustrates the geometry of the five-coordinate trigonal bipyramidal oxyphosphorane transition state that results from the overlay of the two Pi binding modes. The bridging hydroxide plays a pivotal role in both substrate and product binding.

Of particular mechanistic importance is the observation of alternative binding modes of P_i in the active site (Figure 2.2 C and D). In one mode of P_i binding (Figure 2.2 D; comprising ~40% of the population) the substrate mimics only coordination to the redox-active, non-chromophoric metal ion. However, hydrogen bonding between O1 of the bound phosphate moiety and the metal ion-bridging hydroxide leads to a stabilization of the complex. This complex is likely to illustrate the substrate-bound state immediately preceding hydrolysis. Importantly, in this binding mode the phosphorous atom of the substrate mimic is directly in line for a nucleophilic attack by a hydroxide bound to the chromophoric Fe^{3+}. In the other binding mode (Figure 2.2 C; comprising ~60% of the population) P_i forms a μ-1,3 complex with the bimetallic metal center; in addition to these two coordination bonds μ-OH forms bifurcated H bonds with O1 and O4. This complex is likely to represent the product-bound state immediately after hydrolysis. In fact, the superposition of the two P_i binding modes (Figure 2.3 D) leads to a trigonal bipyramid that mimics the proposed transition state of the reaction

[167]. In this state oxygen atoms O1, O2 and O3 span the plane of the pyramid, while O4 represents the position of the nucleophile that initiated the reaction and O5 that of the leaving group.

Here, it is salient to point out that NMR and X-ray absorption studies indicated that at least in the resting form of PAP the Fe^{3+} centre may be five-coordinate and no terminally bound hydroxide ligand is present [176,177]. Furthermore, rapid kinetics measurements in combination with metal ion replacements have demonstrated that there is more than one active nucleophile in the active site; experimental conditions such as pH and the identity of the substrate determine which nucleophile(s) will be selected for a particular reaction [21,171,174]. Hence, while not observed experimentally, it is plausible that a nucleophilic hydroxide enters the coordination sphere of the chromophoric Fe^{3+} upon substrate binding. In agreement with this observation a series of studies with PAP biomimetics supports a role for such a terminal ligand as the effective nucleophile for the hydrolytic reaction [184-186].

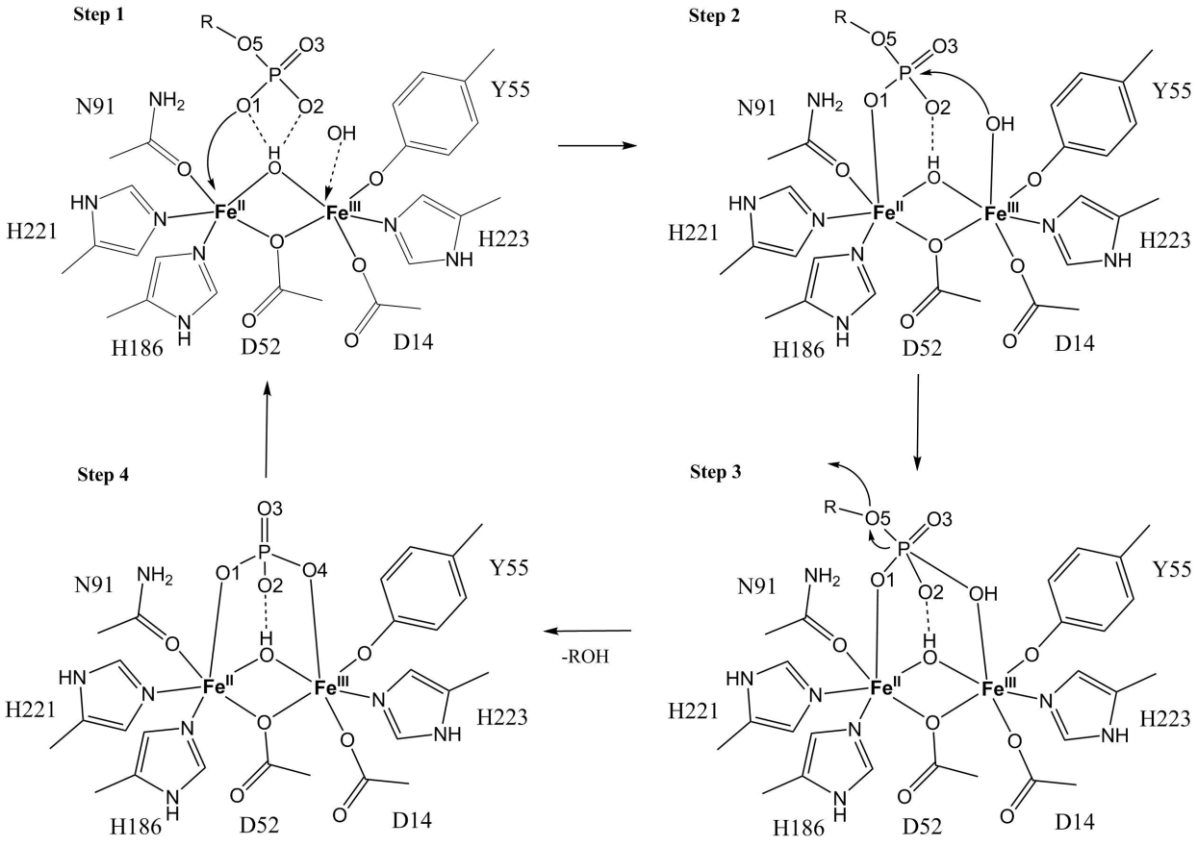

Figure 2.4: Proposed reaction mechanism employed by the FeFe pig PAP. Note that focus here is on the first coordination sphere only. Two Histidine residues in the second sphere also play important roles in substrate binding and transition state stabilization but are not shown for illustrative purposes [4].

The structure of pig PAP with two coordination modes of P_i completes the comprehensive visualization of the trajectory of the reaction coordinate from the initial substrate association to the product-bound state (Figure 2.4). In *Step 1* the substrate binds in a catalytically non-competent manner whereby it interacts, via hydrogen bonds, with the μ-OH group in the active site. This mode of binding was initially proposed based on stopped-flow kinetics measurements [173] and was later observed in PAP from red kidney bean in complex with the tetraoxo anion sulfate [169]. In *Step 2*, illustrated by the monodentate mode of phosphate binding (Figure 2.2 D), the substrate rearranges to form a catalytically competent Michaelis complex. Possibly, at this stage a water molecule enters the active site and coordinates to the chromophoric ferric centre. The substrate is now primed for an attack by this Fe^{3+}-bound nucleophile. The attack (*Step 3*) leads to a five-coordinate trigonal bipyramidal oxyphosphorane that defines the transition state of the reaction. Figure 2.3 D illustrates the structure of this state; oxygen atoms O1-O3 span the plane of the pyramid, while O4 represents the incoming nucleophile. The hydrogen bond between O2 and the μ-OH plays a pivotal role in stabilizing this state. Release of the leaving group from O5 (*Step 4*) then leads to a product-bound complex, illustrated in Figure 2.2 C. The subsequent release of the phosphate moiety then regenerates the active site for the next catalytic cycle.

2.6 Conclusion

In summary, the elucidation of the crystal structure of pig PAP at high resolution, together with the presence of a substrate mimic in two distinct binding modes has facilitated detailed insight into the transition state of the reaction catalysed by a bimetallic hydrolase (previous attempts to crystallize a PAP in presence of transition state mimics such as vanadate or aluminium fluoride failed, either because no suitable crystals for diffraction studies were obtained, or the resolution was too low for a conclusive data interpretation). Of particular relevance is the hydrogen bond formed between one of the oxygen atoms of the phosphate group of the substrate and the metal ion-bridging hydroxide, a feature that may be common amongst metallohydrolases. It is thus likely that the observed transition state is relevant to enzymes other than PAPs, an interpretation that may be exploited in the development of future transition state mimics/chemotherapeutics against a wide range of disorders.

2.7 Funding Sources:

Australian Research Council (DP150104358 and FT120100694). Science Foundation Ireland in the form of a President of Ireland Young Researcher Award (SFI-PIYRA).

2.8 Acknowledgement:

This research was undertaken on the MX2 beamline at the Australian Synchrotron, Victoria, Australia.

Chapter 3

High resolution crystal structure of a fluoride-inhibited organophosphate-degrading metallohydrolase

Christopher Selleck, Luke W. Guddat, David L. Ollis, Gerhard Schenk, Marcelo Monteiro Pedroso.

[a]School of Chemistry and Molecular Biosciences, The University of Queensland, St. Lucia, Queensland, 4072, Australia

[b]Research School of Chemistry, Australian National University, Canberra, ACT, 0200, Australia

Corresponding authors:

M. Pedroso: m.pedroso@uq.edu.au G. Schenk: schenk@uq.edu.au

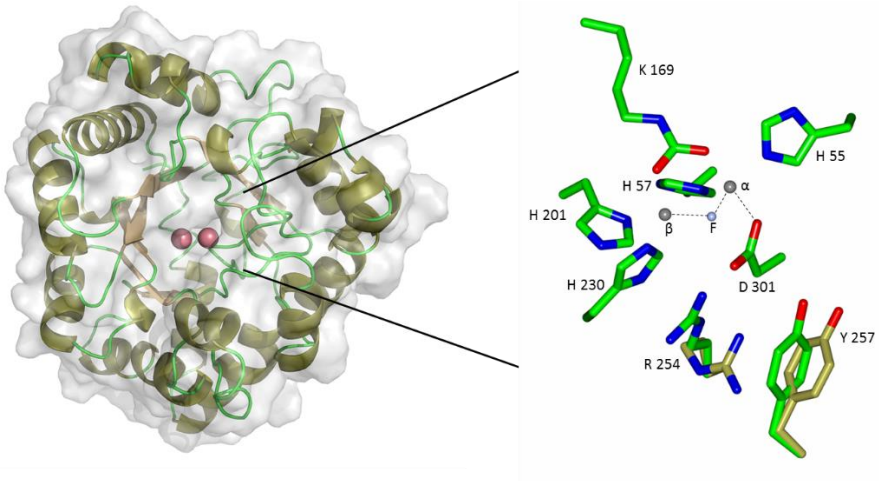

Figure 3.1: Crystal structure of the fluoride-inhibited organophosphate-degrading metallohydrolase from Agrobacterium radiobacter (OpdA). Fluoride displaces the metal ion-bridging nucleophile and disrupts the hydrogen bond network linking the metal ion center to the substrate binding pocket.

3.1 Abstract:

Metal ion-dependent, organophosphate-degrading enzymes (OP hydrolases) have received increasing attention due to their ability to degrade and thus detoxify commonly used pesticides and nerve agents such as sarin and VX. These enzymes thus garner strong potential as bioremediators. The OP hydrolase from *Agrobacterium radiobacter* (OpdA) is one of the most efficient members of this group of enzymes. Previous studies have indicated that the choice of the hydrolysis-initiating nucleophile may depend on the pH of the reaction, with a metal ion-bridging hydroxide being preferred at low pH, and a terminally coordinated hydroxide at high pH. Furthermore, fluoride was shown to be a potent inhibitor of the reaction, but only at low pH. Here, the crystal structure (1.3 Å, pH 6) of OpdA in presence of fluoride is described. While the first coordination sphere in the active site displays minimal changes in the presence of fluoride, the hydrogen bonding network that connects the dimetallic metal center to the substrate binding pocket is disrupted. Thus, the structure of fluoride-inhibited OpdA demonstrates the significance of this hydrogen bond network in controlling the mechanism and function of this enzyme.

3.2 Keywords:

Binuclear metallohydrolases, organophosphate-degrading enzymes, fluoride inhibition, bioremediation

3.3 Introduction:

Organophosphates (OPs) are non-natural compounds that have been synthesized since the late 1800s and have been used as petroleum additives, plasticizers and, in particular since World War II, as pesticides [(187)]. Since then OPs have played a crucial role in facilitating the global expansion of agriculture, but due to their inherent toxicity they pose a considerable risk to both human and environmental health [(5)]. While currently no clean and effective ways for their decontamination are available, microorganisms exposed to such compounds have evolved the enzymatic machinery to utilize them as nutrients to obtain phosphorous for metabolic functions [(5)]. Of particular relevance are OP-degrading phosphotriesterases (PTEs), the first of which was isolated in 1973 from a strain of *Flavobacterium* [(188)]. PTEs have since been identified in several microorganisms, including *Pseudomonas diminuta* [(40)] and *Agrobacterium radiobacter* [(189)]. The PTE expressed by *P. diminuta* (*i.e.* OPH) is identical to that found in the *Flavobacterium*, whereas the *A. radiobacter* enzyme (*i.e.* OpdA) shares approximately 90% sequence with the other PTEs.

OPH and OpdA are among the best-characterized PTEs to date. Both contain a di-metallic metal center in their active sites with invariant amino acid ligands (Figure. 3.2). These include H55, H57 and D301 for the metal ion in the more buried α site, and H201 and H230 for the more solvent-exposed metal ion in the β site (unless stated otherwise residue numbers refer to the sequence of OpdA). In both enzymes the metal ions are bridged via a carboxylated lysine residue (K169) and a water/hydroxide molecule [190]. The precise metal ion composition for the two enzymes is not firmly established; while an analysis of anomalous scattering data indicated that native OpdA may have a preference for the heterodinuclear Fe^{2+}-Zn^{2+} combination [191], both enzymes can readily be activated with a range of divalent metal ions including Zn^{2+}, Co^{2+}, Mn^{2+} and Cd^{2+} [22,192].

Proposed models for the reaction mechanisms employed by the two enzymes are also similar, invoking a role for the metal ion-bridging hydroxide as nucleophile initiating hydrolysis of the OP triester [187]. However, significant variations are observed with respect to their catalytic efficiency, substrate selectivity and metal ion affinities [5,193,194]. Site-directed mutagenesis and in vitro evolution studies demonstrated that in particular two residues in the substrate binding pocket may play an important role in mediating these variations: while R254 and Y257 in OpdA are integrated into an extensive hydrogen bonding network that connects the substrate binding pocket to the metal ion center (Figure. 3.2 A), the corresponding residues in OPH are two histidines, and no hydrogen bond network is present (Figure 3.2 B). In OpdA this network controls the conformation of R254: when present the side chain is kinked, allowing access to the metal center, when absent the side chain is more linear, obstructing access [195]. It is this sequestration of the catalytic site that may underlie (i) the preference of OpdA for smaller substrates, (ii) this enzyme's enhanced catalytic efficiency and (iii) its increased metal ion affinity when compared to OPH [195]. This interpretation may also account for the distinct variation observed between OpdA and OPH with respect to their interaction with fluoride. Fluoride is a potent inhibitor for a number of metal ion-dependent hydrolases, including the di-Ni^{2+} urease [196], the di-Mn^{2+} arginase [197,198] and the Fe^{3+} -M^{2+} purple acid phosphatase (PAP, where M = Fe, Zn or Mn) [199,200]. OpdA is also inhibited by fluoride (Ki ~ 300 nM at pH 6.5), and the uncompetitive mode of inhibition, together with a strong exchange coupling of the metal ions is consistent with fluoride displacing the hydrolysis-initiating μ-OH [195]. Considering that OPH is expected to employ a mechanism similar to that of OpdA (*vide supra*) it is surprising that this enzyme is not inhibited by fluoride [195].

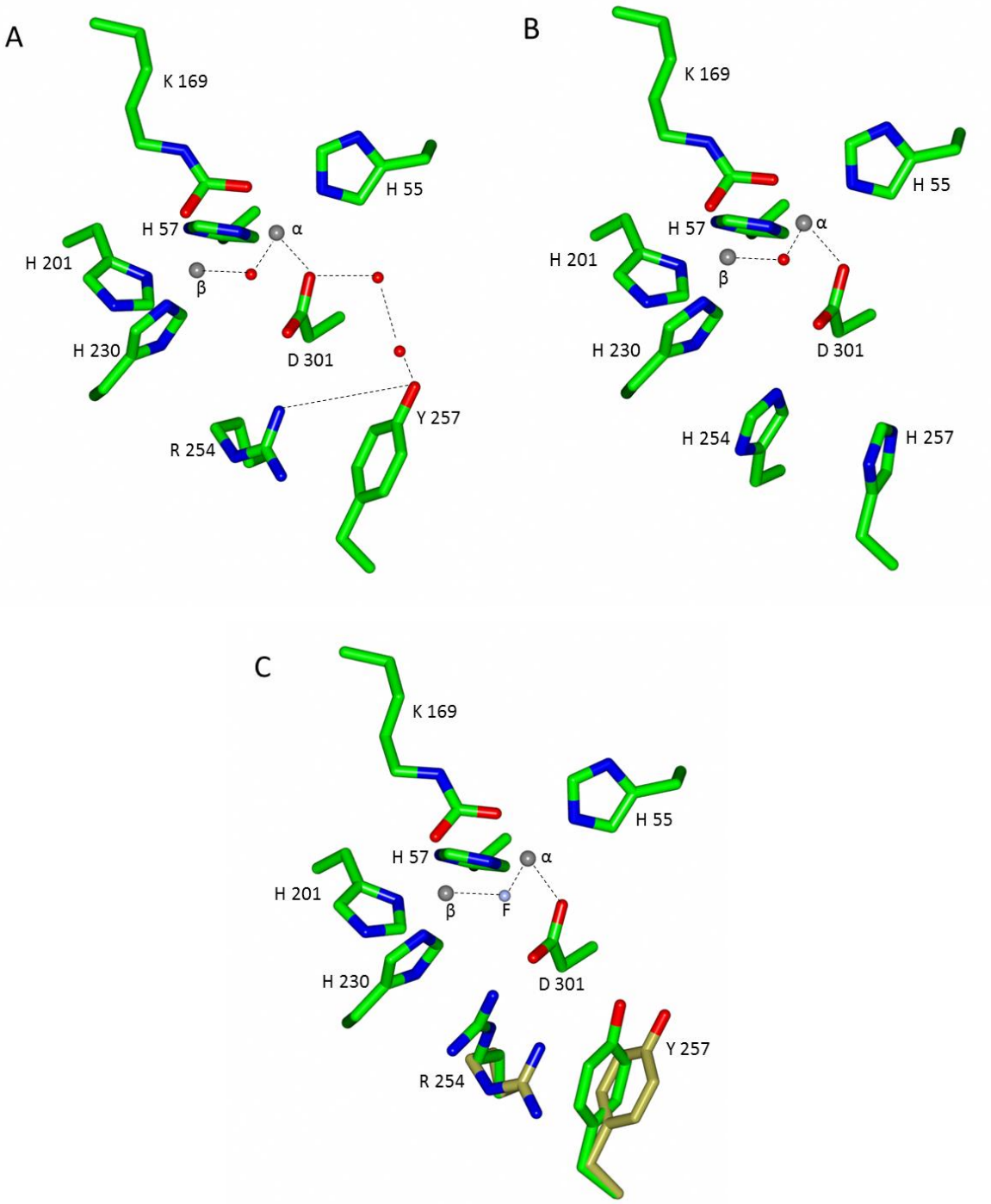

Figure 3.2: Structures of OpdA and OPH. (A) Active site of OpdA in its resting state, illustrating the extensive hydrogen bond network connecting the metal ion center to the substrate binding pocket. (B) Active site of OPH; no hydrogen bond is present. (C) Active site of OpdA in presence of fluoride. The hydrogen bond network is disrupted and the substrate binding pocket residues R254 and Y257 display conformational flexibility

3.4 Results:

In order to better understand the interaction between OpdA and fluoride the enzyme was crystallized in presence of this inhibitor. Recombinant di-Co^{2+} OpdA was expressed and purified using a well-established procedure [22,195,201,202]. The isolated enzyme was >95% pure, judged by SDS PAGE analysis, and concentrated to 20 mg/mL for crystallization in presence of 100 μM fluoride (NaF). The enzyme was crystallized at 20 °C using the hanging-drop vapor-diffusion method. The crystallization solution was made up in 10 mM MES, pH 6.0, with 0.16 M calcium acetate, 80 mM sodium carbonate and 14% v/v PEG 1000. Crystals formed after five days.

Table 3.1: Data collection and refinement statistics for di-Co^{2+} OpdA in the presence of fluoride

Diffraction data	
Resolution Range (Å)	47.2 - 1.3
Observations (I>σ(I))[a]	11143063 (48587)
Unique reflections (I>σ(I))	105162 (4986)
Completeness (%)	99.7 (96.6)
Mean <I/σ(I)>	15.2 (2.3)
R_{merge}	0.073 (0.842)
R_{pim}	0.023 (0.279)
Multiplicity	10.9 (9.7)
Crystal parameters	
Space group	P 31 2 1
Unit cell lengths (Å)	a = 109.072 b = 109.072 c = 62.79
Unit cell angles (°)	α = 90 β = 90 γ = 120
Refinement	
R_{work}[b]	0.1308
R_{free}[b]	0.1437
rmsd bond lengths (Å)	0.007
rmsd bond angles (o)	1.05
Ramachandran plot statistics	
Favored regions	97.21
Outlier regions	0.00
PDB code	5VEJ

[a]Values in parentheses are for the outer resolution shell (1.6-1.3 Å). [b]Rwork = Σ||Fobs|-|Fcalc||/Σ|Fobs|, Rwork is calculated based on the reflections used in the refinement (95% of the total data) and R_{free} is calculated using the remaining 5% of the data.

X-ray diffraction data were collected by remote access on beamline MX-2 at the Australian Synchrotron (Melbourne) using BLU-ICE [179]. The data were integrated, scaled and merged using HKL-2000 [180]. Refinement and model building were carried out using PHENIX 1.8.4 [181] and COOT 0.7 [182], respectively, with the previously published coordinates for OpdA with PDB code 2D2J [165]. All atoms were subsequently refined with anisotropic B-factors. The relevant crystallographic data are summarized in Table 3.1, and coordinates for the structure have been deposited in the Protein Data Bank with accession code 5VEJ.

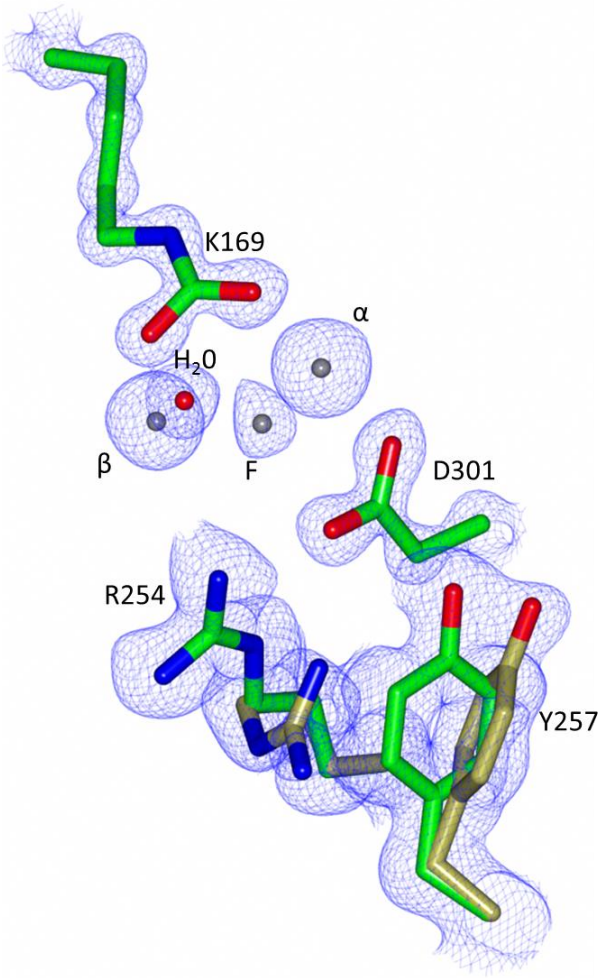

Figure 3.3: Active site of OpdA in presence of fluoride. R254 and Y257 adopt two distinct conformations, a less abundant one that resembles the conformation observed in the absence of fluoride (~20%) and a more abundant one (~80%) that leads to a sequestration of the active site associated with the rearrangement of R254. In both conformations the hydrogen bond network that connects the substrate binding pocket to the metal ion center is disrupted.

3.5 Discussion:

The overall structure of OpdA is virtually indistinguishable from previously reported structures of that enzyme [6,193,202]. The subunit structure adopts a TIM barrel fold, characteristic for members of the amidohydrolase superfamily [203]. Crystallizing OpdA in presence of its uncompetitive inhibitor fluoride also has only a marginal effect on the first coordination sphere of the active site; the metal-metal distance changes from 3.60 Å to 3.67 Å when structures of fluoride-free (2D2J) and fluoride-bound complexes are compared. Similarly, the distances between the metal ions in the α and β sites to the bridging ligand are only minimally affected by the addition of fluoride, changing from 1.94 Å to 1.96 Å for the distance between the metal ion in the α site and the ligand, and from 2.09 Å to 2.14 Å for the corresponding bond involving the metal ion in the β site. More significant is the effect of fluoride on the outer coordination sphere (Figures 3.2 C and 3.3). In particular the conformations of residues R254 and Y257 are affected. In the OpdA structure obtained in the absence of fluoride (Figure 3.2 A) the two side chains appear to be rigid and integrated into an extensive hydrogen bonding network that connects these two residues to D301, a ligand of the metal in the α site (discussed above). In the presence of fluoride structural flexibility is observed, whereby two distinct conformations of both R254 and Y257 are observed (Figure 3.3). One of these (~20% occupancy) resembles that observed in the fluoride-free structure, but the hydrogen bond network is disrupted (compare Figures 3.2 A and 3.2 C). In the other conformation (~80% occupancy) Y257 is tilted away from its original position and R254 moves towards the metal in the β site, obstructing access to the catalytic center.

The crystal structure of OpdA in the presence of fluoride thus provides insight into the mechanism of how this anion may inhibit this enzyme. The crystallographic data do not allow an unambiguous identification of the metal ion-bridging ligand, but due to the uncompetitive nature of fluoride inhibition, together with a significant change to the metal-metal interaction recorded by magnetic circular dichroism (12) it is plausible that fluoride displaces μ-OH. The resulting effect of this replacement on the first coordination sphere is subtle, but sufficient to affect the hydrogen bonding network that connects ligand D301 to Y257 (Figure 3.2). The net effect of this disruption is that R254 is moving closer to the metal ion center, rendering access to the active site for the substrate more difficult and thus inhibiting the overall reaction.

It is important to point out that the inhibitory effect of fluoride for OpdA is abolished at high pH (>9), an observation that was interpreted in terms of having available a hydroxide that is terminally bound

to one of the two metal ions and acts as nucleophile under high pH conditions (12). According to the crystal structure of OpdA in presence of fluoride (Figure 3.3) the terminal ligand bound to the metal ion in the α site is a suitable candidate for this nucleophile. In the absence of a crystal structure of OPH obtained in presence of fluoride the reason for this enzyme's lack of inhibition by this anion remains obscure. However, considering that this enzyme has a lower affinity for the metal in the β site than OpdA, despite identical amino acid ligands (10), indicates some variation in the coordination environment of these two enzymes, possibly linked to a difference in water molecules present in the enzyme-substrate complex. Insofar, in OPH substrate binding may alter the metal ion site in a way that prevents fluoride from binding, or of it binds, it may not displace the relevant nucleophile that initiates catalysis. Additional studies are required to fully understand the factors that contribute to the considerable functional variations observed for two highly homologous enzymes such as OpdA and OPH. However, the present study clearly demonstrated the significance of a hydrogen bonding network in the mechanism employed OpdA. For OPH, that lacks this network, the mechanism may be more reliant on a flexibility in the immediate coordination environment, especially of the metal ion in the β site. The study thus demonstrates how relatively subtle changes in a protein sequence can have significant effects with respect to enzymatic properties. This observation makes PTEs such as OpdA and OPH ideal candidates for optimization into catalyst that can be employed in bioremediation. Efforts towards this goal are in progress.

3.6 Acknowledgement

For financial support we are grateful to the Australian Research Council (DP150104358 and FT120100694). This research was undertaken on the MX2 beamline at the Australian Synchrotron, Victoria, Australia.

Chapter 4
Crystal structures of the B3 MBLs MIM-1 and MIM-2 from environmental microorganisms

4.1 Abstract

Genes that confer antibiotic resistance can rapidly be disseminated from one microorganism to another by mobile genetic elements, thus transferring resistance to previously susceptible bacterial strains. In particular the misuse of antibiotics in health care and agriculture has provided the ideal evolutionary pressure that has led to a rapid recent spread of β-lactamases, *i.e.* SBLs and MBLs, enzymes that are highly potent in inactivating most of the commonly used β-lactam antibiotics (see also Chapter 1). However, genes that confer antibiotic resistance are not only associated with pathogenic microorganisms, but are also found in non-pathogenic (*i.e.* environmental) microorganisms. Two such examples are the MBLs from *Novosphingobium pentaromativorans* and *Simiduia agarivorans, i.e.* Maynooth IMipenemase 1 (MIM-1) and 2 (MIM-2), respectively. Previous studies demonstrated that these proteins are homologous to B3-type MBLs, with catalytic properties similar to well-characterised MBLs such as AIM-1 (see Chapter 5). Here, the crystal structures of MIM-1 (2.60 Å) and MIM-2 (1.84 Å) are discussed and compared to MBLs from pathogenic origins.

4.2 Introduction

United States, Nevada, September 2016, a woman in her seventies died from an infection caused by carbapenem-resistant *Enterobacteriaceae* bacteria, resistant to all available antibiotics[204]. This woman was not the first to die of antibiotic-resistant bacteria. In fact, in 2013 the Centre for Disease and Control and Prevention (CDC) of the United States published a report where it is estimated that at least 2 million people acquire serious infections every year and at least 23,000 people die from the direct result of antibiotic resistant infections [82]. It was estimated that in 2011 alone there were 310,000 cases of multidrug-resistant tuberculosis, the majority of them occurring in China, India, Pakistan, Russia and South Africa [205,206]. Nonetheless, the problem is global and bound to worsen if no action is taken.

While antibiotic resistance has emerged amongst both Gram-positive and Gram-negative pathogens, it is the latter group (in particular the ESKAPE pathogens, *i.e. Enterococcus faecium, Staphylococcus aureus*, *Klebsiella pneumoniae*, *Acinetobacter baumannii*, *Pseudomonas aeruginosa* and the *Enterobacter* species) that poses a particularly alarming problem as there are only a few antimicrobial agents available to battle these pathogens [205,207]. The misuse of antibiotics is the single most important factor leading to antibiotic resistance around the world. A successful strategy used by the pathogens to acquire resistance is through the production of enzyme MBL, a member of the BMH family (208) (see also Chapter 1). Sustained periods of haphazard use of antibiotics in both the medical sector and agriculture, combined with enhanced global motility, have attributed to the growing threat of antibiotic resistance (209). Although the main contributor to their recent sharp rise is ascribed to anthropogenic activities [210,211], antibiotic-resistant bacteria have also been detected in pristine, unchallenged environments such as LRA-8 (this particular enzyme is further investigated in Chapter 6) [26,136]. Therefore, the study of the properties of MBLs from "unusual", *i.e.* pristine environments may hold clues about the origin and evolution of a major strategy employed to confer antibiotic resistance. It may also assist in the development of new drugs to combat this major threat to modern health care.

In the search for novel MBL-like proteins from unusual organisms, our group previously identified two possible candidates, one from *Novosphingobium pentaromativorans* and one from *Simiduia agarivorans*, both marine microorganisms. The proteins were labelled Maynooth IMipenemase 1 (MIM-1) and 2 (MIM-2), respectively [25,26,212]. Their nomenclature was associated with the place

(Maynooth University, Ireland) where they were initially discovered, but as will be demonstrated in this Chapter, these labels are not ideal as they infer a close similarity of these two proteins. Although both MIM-1 and MIM-2 are homologous to members of the B3 subgroup of MBLs they share only 23% protein sequence similarity with each other [26]. Furthermore, the true biological function of these enzymes is not yet known as they are multifunctional *in vitro*, possessing both MBL and N-acylhomoserine lactonase activities [26]. In order to further probe the function of MIM-1 and MIM-2, their crystal structures were solved here and compared with those of other MBLs.

4.3 Materials and Methods

MIM-1 and MIM-2 were expressed and purified using a previously published procedure [137]. In brief, BL21 (DE3) cells were transformed with the plasmid bla_{MIM-1} or bla_{MIM-2} pJ411 (vector commercially available from DNA 2.0). The proteins were expressed in LB medium, supplemented with 50 µg/ml kanamycin. Initially, the cell cultures were grown at 37 °C until the OD_{600} reached 0.4 - 0.6. Then expression was induced by addition of 1 mM of IPTG at 18 °C; subsequently, the cell culture was grown for another 48 hours. Cells were then harvested by centrifugation and purified on a Hi-trap Q FF column, equilibrated with 20 mM Hepes buffer, pH 7.5, 0.15 mM $ZnCl_2$. Then proteins were eluted with a linear gradient from 0 to 1 M NaCl. Fractions containing activity against cefuroxime were combined, concentrated and subsequently loaded onto a Hiprep 16-60 sephacryl S-300 HR gel filtration column and eluted with 50 mM Tris buffer, pH 7.2, containing 0.15 mM $ZnCl_2$. The fractions were at least 95% pure, as judged by SDS-PAGE gel analysis, and the purified protein was stored in 10% glycerol at -20 °C. The protein concentration was determined by measuring the absorption at 280 nm (ε = 36,815 $M^{-1}cm^{-1}$ and 41,285 $M^{-1}cm^{-1}$ per monomer for MIM-1 and MIM-2, respectively)[26].

4.4 Crystallisation, X-ray diffraction data collection and refinement

Crystals were prepared using the hanging-drop diffusion method at 20 °C. The drop solution contained 300 µL of the desired enzyme (*i.e.* MIM-1 or MIM-2) at approximately 40 mg/mL and 300 µL of the precipitant buffer. The precipitant buffer used for MIM-1 was 0.05 M citrate, pH 5, 0.05 M Bis Tris Propane, pH 9.7, and 16% w/v PEG-3350; for MIM-2 it was 0.1 mM DS56E8 (a detergent), 0.1 M sodium citrate, pH 5.5, and 22% w/v PEG-3350. Typically, diamond-shaped (MIM-1) or plate-like (MIM-2) crystals began to form after seven days and continued to grow for the next 6 days (Figure 4.1). After this period, the crystals began to decompose and were no longer suitable for

crystallographic study. The crystals were thus cryoprotected in a mixture of 20% glycerol added to the precipitant buffer.

Crystallographic data were collected by remote access on beamline MX-2 at the Australian Synchrotron (Melbourne) using BLU-ICE [179]. The data were integrated, scaled and merged using HKL-2000 [180]. Refinement and model building were carried out using PHENIX 1.8.4 [181] and COOT 0.7 [182], respectively, using the previously published coordinates for Adelaide-IMipenemase-1 (AIM-1; see also Chapter 5) from *P. aeruginosa* (4AWY) [7]. All atoms were subsequently refined with anisotropic B-factors; most hydrogen atoms were fitted as riding models, though the proton of the bridging hydroxide was added manually based on the electron density. Relevant crystallographic data and refinement statistics are summarized in Table 4.1.

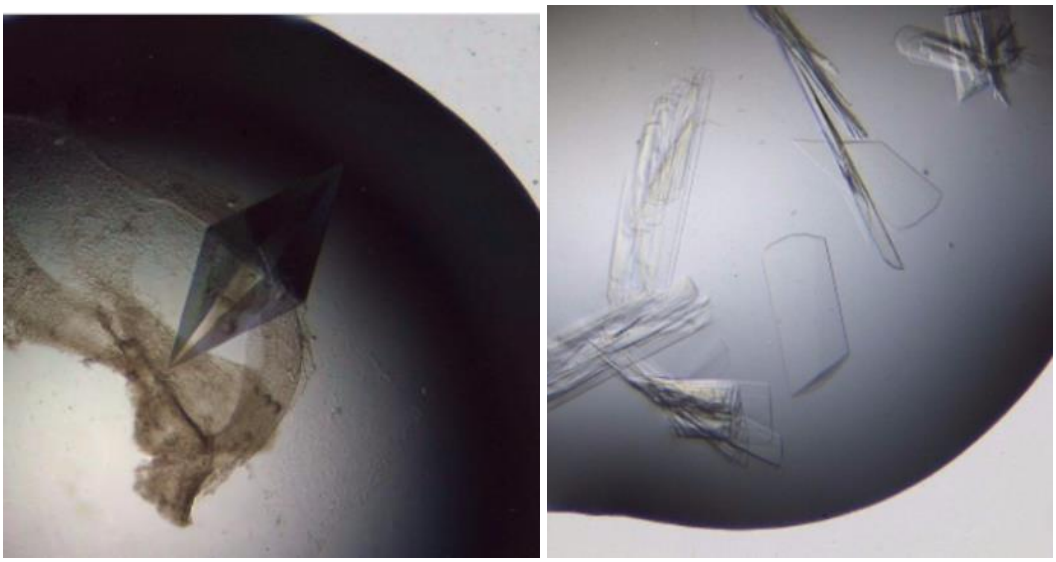

Figure 4.1: Typical diamond-shaped crystal obtained for MIM-1 (left). Characteristic plate-like crystals obtained for MIM-2.

4.5 Results and discussion

4.5.1 Protein purification and crystallography

Recombinant MIM-1 and MIM-2 were expressed in *E. coli* BL21(DE3) and purified using a protocol previously established by our group [26]. Importantly, the mature proteins had no N-terminal signal peptides, thus preventing their secretion into the periplasma. Both proteins crystallised over a period of approximately eight days.

For MIM-1 the large diamond-shaped crystals (Figure 4.1) diffracted to 2.6 Å and were of space group P 41 21 2. Molecular replacement showed the presence of a single molecule occupying each asymmetric unit (Table 4.1). The overall structure of MIM-1 consists of a well-defined electron density map containing 274 amino acid residues (out of 300 in total for the full length enzyme), allowing for an uninterrupted trace of the polypeptide backbone from Pro33 to Ala305. Also present are the two catalytically important Zn^{2+} ions with occupancies of 1.0 each, along with a citrate molecule, which was a component of the crystallisation buffer. The Ramachandran plot shows that most of the residues (93.73%) are within the favoured regions, whilst another 1.97% are within the allowed region.

For MIM-2 the plate-like crystals (Figure 4.1) diffracted to a resolution up to 1.8 Å and have the space group P 2 21 2, also with only one molecule per asymmetric unit. The structure of MIM-2 is well defined in the electron density map resolved for 264 residues (out of 295 in total for the full length enzyme), allowing for an interrupted trace of the polypeptide backbone from Thr31 to Ala300. However, the electron densities for the side chains of Ala160 to Leu161 and Glu207 to Arg210 are not clearly identifiable, hence, these residues are not present in the final structure. Also present are two Zn^{2+} ions, defining the catalytically relevant active site with an occupancy of 1.0 each (Figure 4.3). A Ramachandran plot shows that 94.19% of all residues are within the favoured regions whilst another 4.26% are within allowed regions. The Patterson analysis function in Xtriage indicates a significant off-origin peak that is 20.8% of the magnitude of the origin peak. This observation strongly suggests the presence of pseudo-translational symmetry within the data.

The refined overall structures of MIM-1 and 2 are shown below in Figure 4.2, along with the structures of the MBLs AIM-1, L1, SMB-1 and FEZ-1 for comparative purpose.

Table 4.1: Crystallographic data collection data and refinement statistics for MIM-1 and MIM-2.

Diffraction data	MIM-1	MIM-2
Resolution Range (Å)	48.06- 2.6	42.83- 1.84
Observations (I>σ(I))[a]	230230 (27609)	216935 (9576)
Unique reflections (I>σ(I))	16484 (1964)	24468 (1318)
Completeness (%)	99.9 (99.6)	99.3 (88.2)
Mean <I/σ(I)>	21.8 (2.2)	7.5 (2.2)
R_{merge}	0.0.078 (1.014)	0.168 (0.536)
R_{pim}	0.022 (0.278)	0.06 (0.205)
Multiplicity	14.0 (14.1)	8.9 (7.3)
Crystal parameters		
Space group	P 41 21 2	P 2 21 2
Unit cell lengths (Å)	a = 67.96 b = 67.96 c = 216.67	a = 51.67 b = 69.53 c = 76.54
Unit cell angles (°)	α = 90 β = 90 γ = 90	α = 90 β = 90 γ = 90
Refinement		
R_{work}[b]	0.1728	0.2602
R_{free}[b]	0.2194	0.3090
rmsd bond lengths (Å)	0.0062	0.0019
rmsd bond angles (o)	0.860	0.568
Ramachandran plot statistics		
Favoured regions	93.73	94.19
Outlier regions	0.37	1.55

4.5.2 Overall structure of MIM-1 and MIM-2

The overall folds of MIM-1 and MIM-2 consist of an αβ/βα motif that is characteristic for MBLs, with the hydrophilic α helices exposed to the solvent and the central core formed by two β-sheets composed of five and seven β strands (Figure 4.2). Specifically, both MIM-1 and 2 include thirteen B-sheets with seven antiparallel strands at the N-terminus (B1-B7) and five antiparallel sheets at the C-terminus. Additionally, the MIM-1 structure also contains six α helices, two 3_{10} helices (η1 and η2) and a citrate molecule bound within the active site. In contrast, the MIM-2 structure also contains 8 α helices and three 3_{10} helices (η1 to η3) as can be seen in the sequence alignment presented in Appendix A.

The active site groove is defined by two loops which are located at the interface of the two αβ domains and houses amino acid residues that are pivotal to the binding of substrates (Figure 4.4). Housed within the active site are two Zn ions whose amino acid coordination's are identical to those of B3-type MBLs (see below for details) [7,70]. Other interesting features include the presence of a Gln 157 residue located on loop 1 (Figures 4.3 and 4.4) and the presence of a third disulphide bridge which binds the extended N-terminus away from the active site, creating an open and accessible active site pocket capable of housing even the bulkiest substrates (Figures 4.5 and 4.6). These features are suggested to increase the ability of theses enzymes to hydrolyse a wide range of substrates and is discussed in detail below.

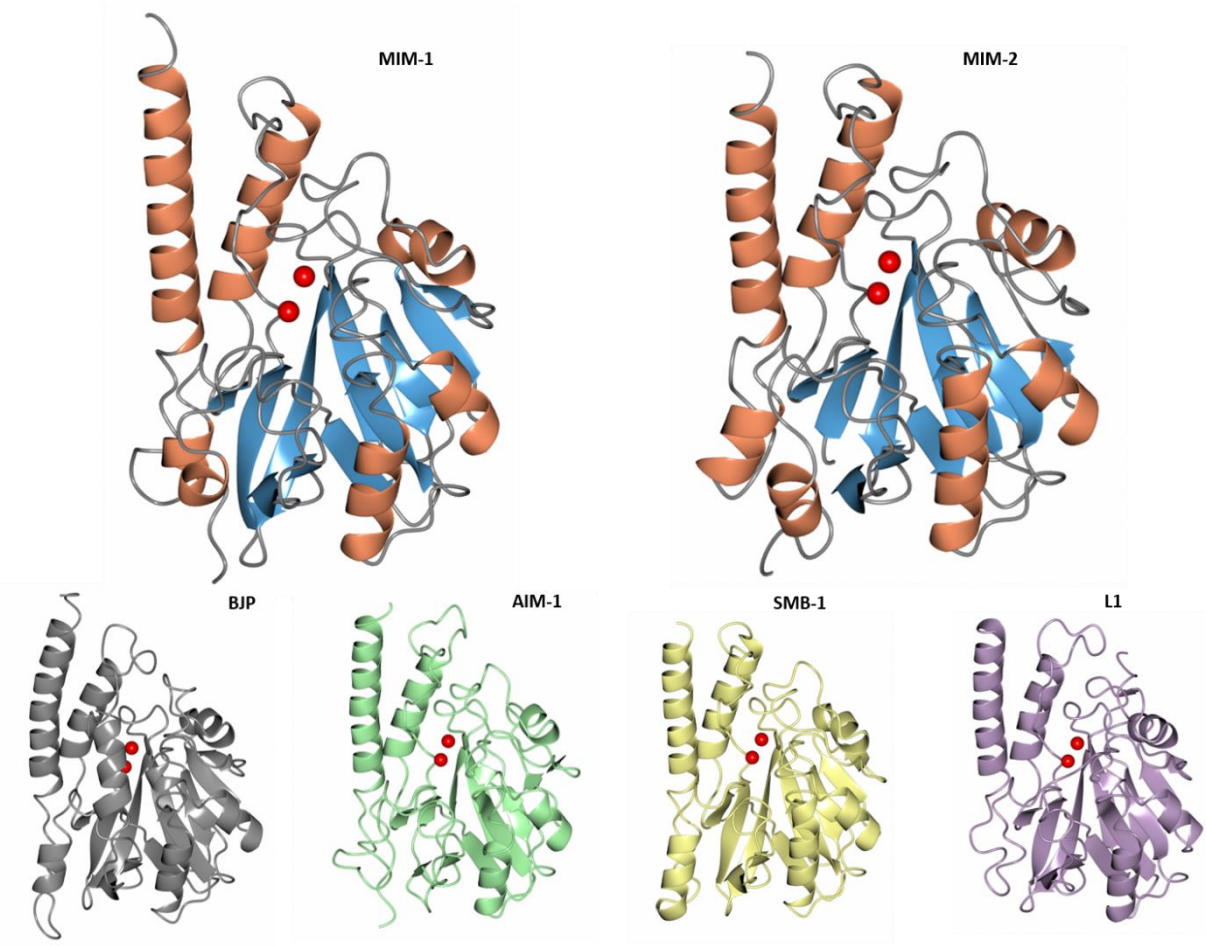

Figure 4.2: Overall structures of MIM-1 and MIM-2 with secondary structures coloured orange for helix and blue for sheet regions. For comparison the structures of the B3-type MBLs BJP from *B. japonicum* (PDB 3LVZ), AIM-1 from *P. aeruginosa* (PDB 4AWY), SMB-1 from *S. marcescens* (PDB 3VPE) and L1 from *S. maltophilia* (PDB 1SML) are also shown. All enzymes contain the characteristic αβ/βα structural motif, with the catalytically relevant metal ion centre located in the middle. The Zn^{2+} ions are shown as red spheres. The figure was generated using CCP4MG (http://www.ccp4.ac.uk/MG/).

4.5.3 Zn binding and active site

The zinc binding site in MIM-1 and MIM-2 is defined by the HXHXDH sequence motif, which is a characteristic motif for the core of the binuclear metal ion binding site in the MBL superfamily [7]. Thus, not surprisingly the coordination of the zinc ions in the active site of MIM-1 and MIM-2 closely resembles that observed for other MBLs, especially those of the B3 subgroup (Figure 4.3). The Zn-Zn distances in MIM-1 (4.02 Å) and MIM-2 (3.40 Å) are comparable with those observed in BJP-1, FEZ-1, L1 and AIM-1 structures (Table 4.2) [7,122,130,133]. The increased distance between the metal ions in MIM-1 is likely due to interactions with the bound citrate molecule, who's carboxyl oxygens are seen to occupy the positions of W1, W2 and W3 seen for MIM-2.

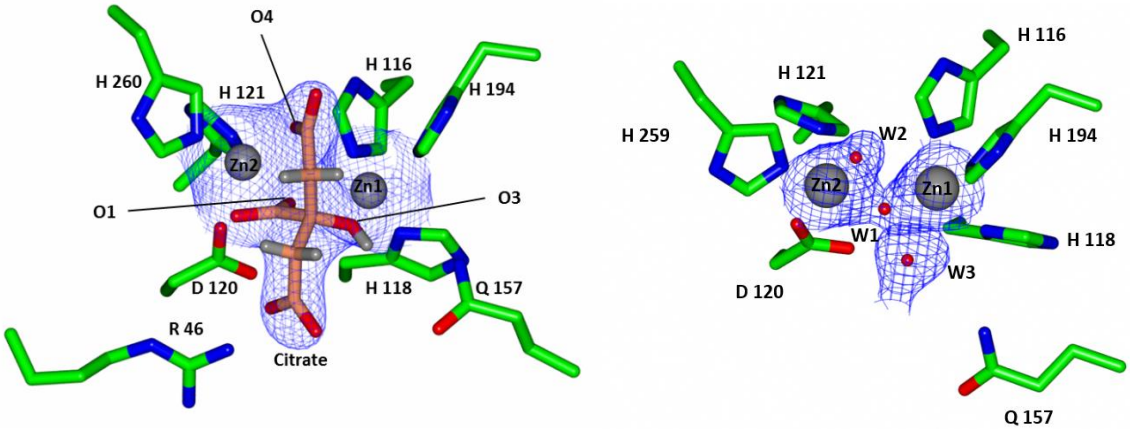

Figure 4.3: Active site structures of MIM-1 (left) and MIM-2 (right), including Gln157 in both enzymes and Arg46 (for MIM-1 only), which may play an important role in substrate binding (see text for details). In MIM-1 a molecule of citrate (a component of the crystallisation solution) is present in the active site with carbonyl oxygens occupying the positions of W1, W2 and W3 seen for MIM-2.

Generally, the active sites of all known B3-type MBLs, including the two MIM proteins, are highly conserved. For MIM-1 and MIM-2 the metal ion in the Zn1 site is coordinated in a tetrahedral conformation by His116, His118 and His194 (the His site), while the Zn2 site adopts a rather trigonal bipyramidal geometry, formed by residues Asp120, His121 and His260 (His259 in MIM-2). Relevant Zn-ligand distances are summarised in Table 4.2. It is interesting to point out that in MIM-1, unique among MBLs, an arginine residue (Arg46) located on the hairpin leading toward the N-terminus, is within close proximity to the active site (Figure 4.3). Although it has yet to be determined, it is possible that this side chain may play a role in the recognition of substrates for this enzyme. Directed

mutagenisis experiments on this residue may determine the impact, positive or negative, that this residue imposes upon the binding of substrates.

Table 4.2: Selected distances between the zinc ions and their ligands in the active sites of MIM-1 and MIM-2.

Interaction partner	MIM-1	MIM-2
Zn1		
His 116	2.09 Å	2.20 Å
His 118	1.91 Å	2.03 Å
His 194	2.08 Å	2.03 Å
W1	-	1.96 Å
W2	-	3.07 Å
O4 (displaced W1)	2.58 Å	-
O3 (displaced W2)	2.70 Å	-
Zn2		
Asp 120	2.34 Å	2.03 Å
His 121	1.97 Å	2.21 Å
His 260	2.00 Å	2.10 Å
W1	-	1.99 Å
W3	-	2.02 Å
O4 (displaced W1)	1.86 Å	-
O1 (displaced W3)	2.18 Å	-
Zn1-Zn2	4.02 Å	3.40 Å

The active site pocket of B3 MBL is largely defined by two loops that house the residues responsible for substrate recognition and binding. The backbone trace of the loop 1 and 2 regions for the MIM proteins is highly conserved with Aim-1 and SMB-1 yet differs from other members of the B3 subclass. Previously published directed mutagenesis and substrate co-crystallisation studies, have illustrated that residues Gln157 (located on loop 1), Ser221 and Thr223 (both located on loop 2) play a role in substrate recognition [7,71,213]. These residues are mostly conserved between the MIM proteins (Thr223 is replaced by Ser 223 in MIM-1), AIM-1 and SMB-1 however some small changes in geometry are evident.

Interestingly, it has been proposed that the presence of a Gln157 residue only occurs in MBLs that were acquired via horizontal gene transfer, but is not present in MBLs that are located on chromosomes (*i.e.* such as L1, BJP or FEZ-1) [70,130,133]. Thus, it seems likely that the MIM proteins are indeed located on a mobile genetic element and were acquired through horizontal gene transfer.

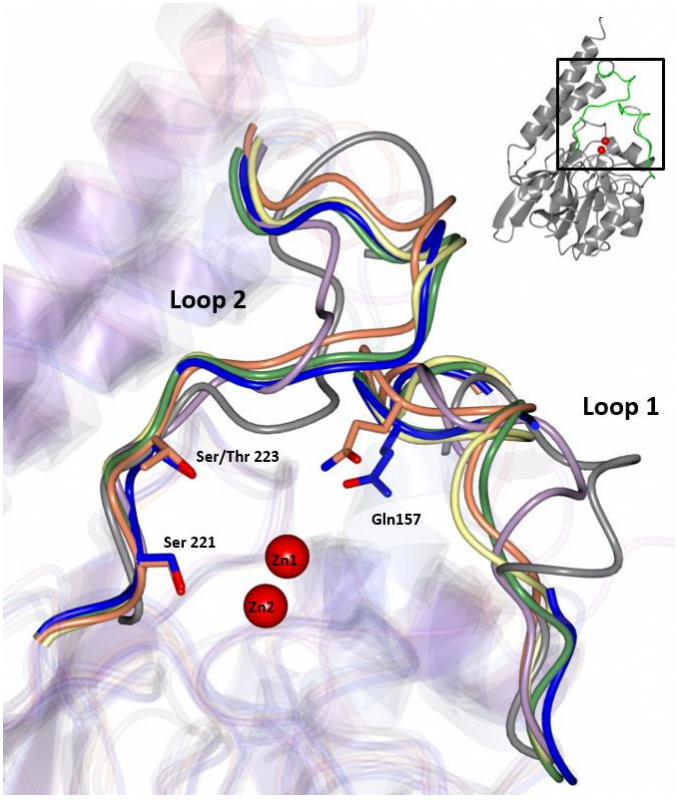

Figure 4.4: Loop 1 and 2 regions for selected MBL MIM-1 (orange), MIM-2 (blue), AIM-1 (green)[7], L1 (lilac)[122], SMB1 (yellow)[71] and BJP (grey)[130]. Important residues for substrate binding are also shown for the MIM proteins.

4.5.4 Disulphide bridges

Intramolecular disulphide bonds play an important role in protein folding and stability. Majority of B3 MBL poses at least one disulphide bond. In both of the MIM proteins three disulphide bridges are present (Figure 4.5). The Cys253-Cys282 and Cys252-Cys281 pair in MIM-1 and MIM-2, respectively, is also present in majority of B3-type MBLs. The two additional disulphide bonds (Cys40-Cys68, Cys206-Cys212 and Cys43-Cys68, Cys206-Cys211 in MIM-1 and MIM-2, respectively) are present in AIM-1 and SMB-1 but no other B3-type MBLs [7]. In particular, the Cys40-Cys68 (MIM-1) or Cys43-Cys48 (MIM-2) disulphide bridge directly affects the folding of the extended N-terminus in these enzymes. This bridge links the η1 helix with the β2 strand, causing the extended N-terminus to fold away from the active site (Figure 4.6). Similar B3 MBL that share this feature (Eg AIM-1, SMB-1) tend to have higher activity than those whose N-terminus enters or imposes on the space available within the active site (eg. BJP and RM3) [70,71,130,135]. With this theme in mind, it has been shown that the L1 protein also gained a reduction of the Kcat/km by at least 20-fold when its extended N-terminus was truncated such that it no longer imposed on the active site

[126]. Thus, it appears as though this feature is beneficial for the promiscuous catalytic activity of these enzymes, facilitating access for substrates with bulky functional groups [7].

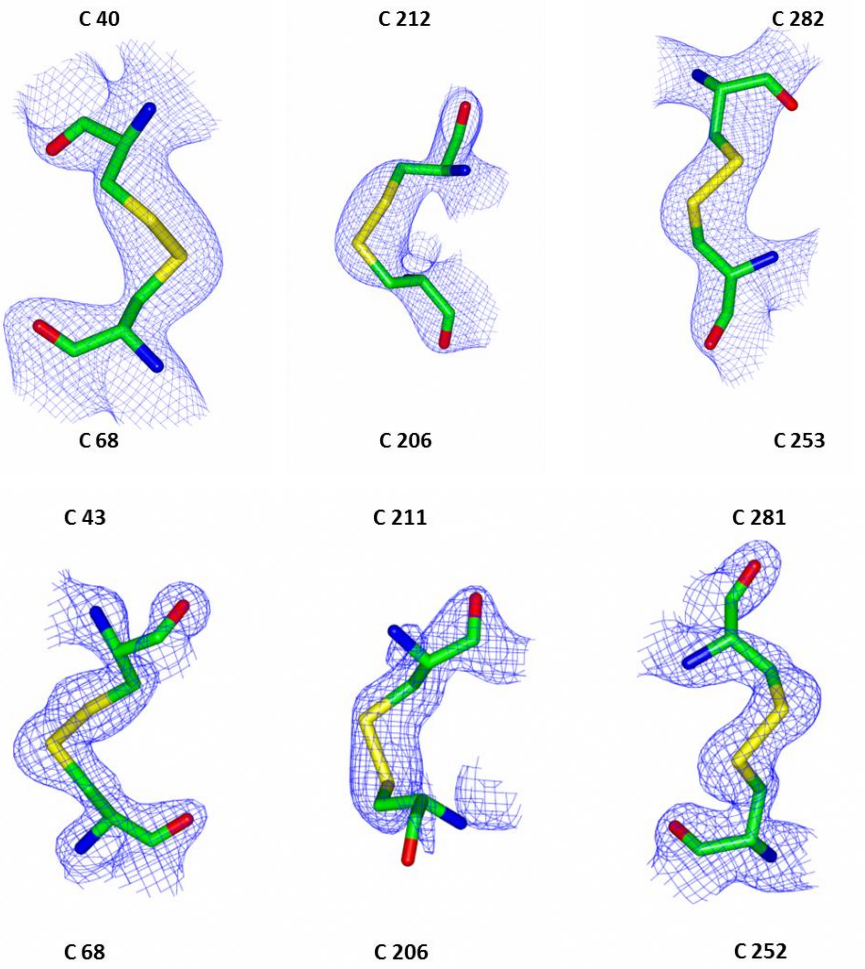

Figure 4.5: MIM-1 (top) and MIM-2 (bottom) have three disulphide bridges (shown with associated electron densities).

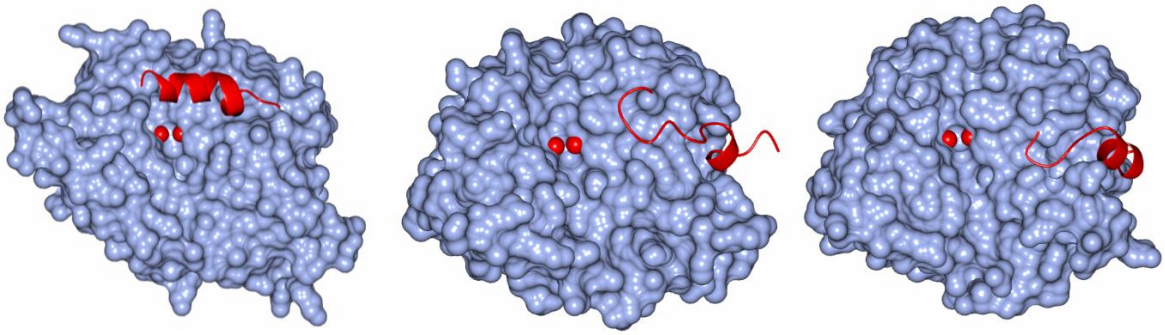

Figure 4.6 The extended N-terminus for BJP (left), MIM-1 (middle) and MIM-2 (right), illustrating the open active site of the MIM proteins in contrast to BJP, who's active site is blocked by the N-terminus..

4.6 Conclusion

In this Chapter, the crystal structures of two novel B3-type MBL-like enzymes from environmental (*i.e.* non-pathogenic) microorganisms are described. Indeed, MIM-1 and MIM-2, are closely related in structure to AIM-1, a B3-type MBL identified in a strain of *P. aeruginosa* that is resistant to most commonly used antibiotics (see also Chapter 5) [7]. This observation may not be surprising considering that the amino acid sequence of AIM-1 was used as a query sequence to identify MIM-1 and MIM-2 [25]. Although little is known about the genetic make-up of the host organisms of MIM-1 and MIM-2 (*i.e. N. pentaromativorans* and *S. agarivorans*, respectively) the structural similarity to AIM-1 suggests that the two novel MBL-like enzymes may be located on mobile genetic elements. Considering the considerable catalytic efficiency and broad range of substrates of MIM-1 and MIM-2 these enzymes may thus present a real threat to health care [26,212].

Both MIM-1 and MIM-2 have the αβ/βα fold characteristic for all MBLs. Generally, the loop regions and substrate binding residues are conserved between the MIM proteins and other B3 MBL. Interestingly, residue Gln157, which has only been seen in AIM-1 and SMB-1, is positioned close to the catalytic bimetallic metal ion centre where it is likely involved in interactions with the carbonyl group of the β-lactam ring, thus enhancing the electrophilicity of the substrate. Furthermore, the presence of additional disulphide bridges was seen to enlarge the active site through binding the extended N-terminus away from the active site. The combination of all these features are likely essential factors contributing to the promiscuous functionality of MIM-1 and MIM-2. With this knowledge, these enzymes may provide clues as to how to develop inhibitors that are not only potent in stopping β-lactamase activity, but that are also persistent. Studies towards this aim are currently in progress.

Chapter 5

AIM-1: an antibiotic-degrading metallohydrolase that displays mechanistic flexibility

Christopher Selleck, James L. Larrabee, Jeffrey Harmer, Luke W. Guddat, Nataša Mitić, Waleed Helweh, David L. Ollis, Whitney A. Craig, David L. Tierney, Marcelo Monteiro Pedroso, Gerhard Schenk

[1]School of Chemistry and Molecular Biosciences, The University of Queensland, St. Lucia, Queensland, 4072, Australia

[2]Department of Chemistry and Biochemistry, Middlebury College, Middlebury, Vermont 05753, USA

[3]Centre for Advanced Imaging, The University of Queensland, St. Lucia, Queensland, 4072, Australia

[4]Department of Chemistry, Maynooth University, Maynooth, Co. Kildare, Ireland

[5]Research School of Chemistry, Australian National University of Canberra, ACT, 0200, Australia

[6]Department of Chemistry and Biochemistry, Miami University, Oxford, Ohio 45056, USA

Corresponding authors:

M. Pedroso: m.pedroso@uq.edu.au G. Schenk: schenk@uq.edu.au

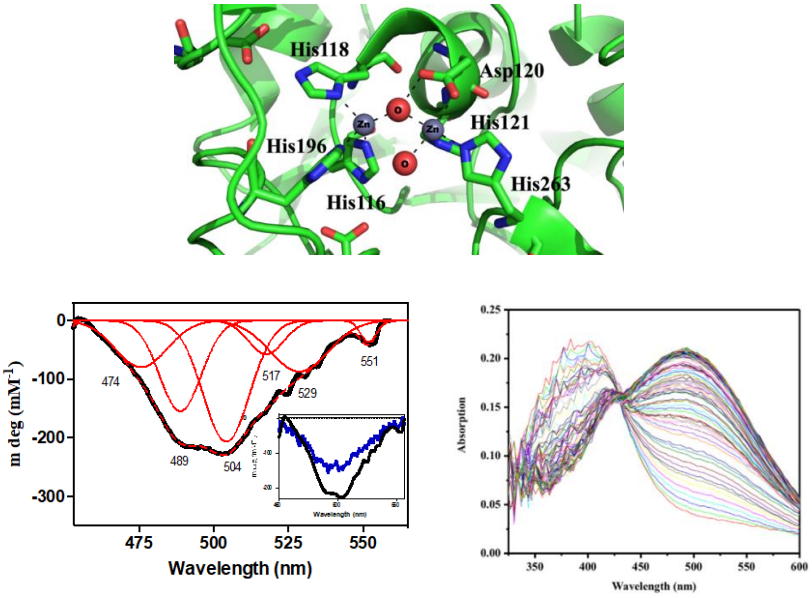

Figure 5.1: AIM-1 is a metallo-β-lactamase (MBL) with a broad substrate specificity. A range of physico-chemical techniques have been employed to demonstrate that both substrates and inhibitors may bind in different modes and locations to the enzyme. The insight gained may pave the way for the development of clinically useful universal MBL inhibitors, an essential strategy to combat antibiotic resistance.

5.1 Abstract

Antibiotic resistance has emerged as a major threat to global health care. This is largely due to the fact that many pathogens have developed strategies to acquire resistance to antibiotics. Metallo-β-lactamases (MBL) have evolved to inactivate most of the commonly used β-lactam antibiotics. AIM-1 is one of only a few MBLs from the B3 subgroup that is encoded on a mobile genetic element in a major human pathogen. Here, its mechanism of action was characterised with a combination of spectroscopic and kinetic techniques and compared to that of other MBLs. Unlike other MBLs it appears that AIM-1 has two avenues available for the turnover of the substrate nitrocefin, distinguished by the identity of the rate-limiting step. This observation may be relevant with respect to inhibitor design for this group of enzymes as it demonstrates that at least some MBLs are very flexible in terms of interactions with substrates and possibly inhibitors.

5.2 Keywords:

Antibiotic resistance, β-lactam antibiotics, metallo-β-lactamase, imipenemase, metalloenzyme

5.3 Introduction

β–Lactamases are a class of enzymes that catalyze the hydrolysis of the four-membered β-lactam ring, the characteristic feature of many commonly used antibiotics such as penicillins, carbapenems, cephalosporins and monobactams (Figure 5.2). These compounds are very effective in impeding the enzymes involved in the generation of peptidoglycans in the cell wall of pathogenic bacteria [16,150,156,208].

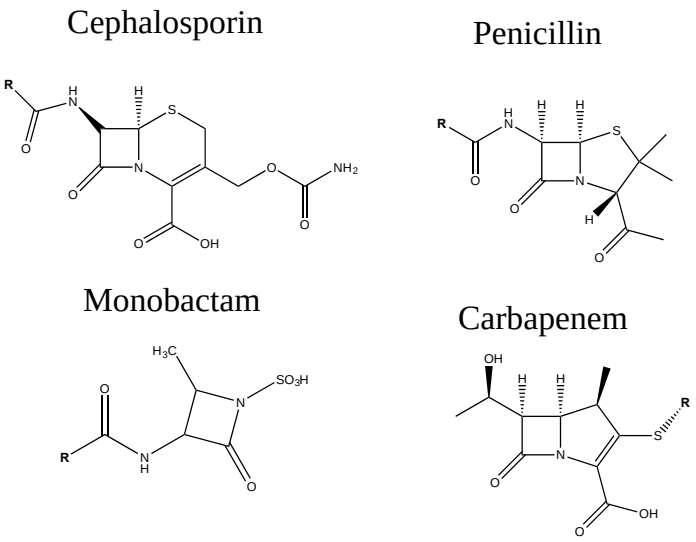

Figure 5.2: Illustration of the four major groups representing the family of β-lactam antibiotics.

β-Lactamases are divided into two main classes based on their mechanism of action and cofactor requirements [15,16,150,156,208]. These include the serine-β-lactamases (SBLs), which employ a serine residue to initiate the hydrolysis of the β-lactam ring (*i.e.* its opening), and metallo-β-lactamases (MBLs), which require either one or two metal ions in their active site as essential cofactors for catalysis [15,16,150,156,208]. MBLs are further sub-divided into as many as four sub-groups, *i.e.* B1, B2, B3 and B4, depending on their sequence homology and metal ion requirements. However, all MBLs do share a characteristic αββα fold (as discussed in Chapter 1) [15,16,150,156,208,214].

MBLs from the B1 subgroup generally require two Zn^{2+} metal ions for catalytic activity [15,16,150,156,208,214], although at least the MBL from *Bacillus cereus* (BcII) was shown to be partially active in its mononuclear form [151]. In contrast, B2-type MBLs require only one metal ion in their active site for optimal catalytic activity; the binding of a second metal ion leads to the inactivation of the enzyme [215]. These MBLs are also more selective in terms of their preferred substrates displaying specific activity towards monobactams (Figure 5.2), a group of antibiotics that are poor substrates for other MBLs [215]. B3-type MBLs are similar to B1 enzymes in that they require two metal ions in their catalytic site to be fully active, however their active site architecture is quite different [216]; whilst B1- and B3-type MBLs have identical ligands for one of the two Zn^{2+} binding sites (the Zn1 site; Figure 5.2), they differ in the other metal centre (the Zn2 site; Figure 5.3) [16,150,156,208,216].

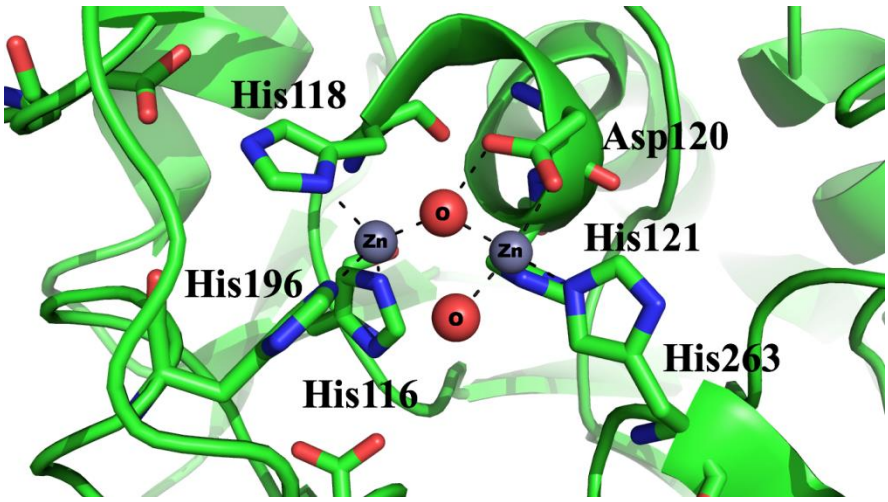

Figure 5.3: Active site structure of AIM-1. Two Zn^{2+} ions (grey spheres) are bound in the catalytic centre. The Zn1 site contains the ligands His116, His118 and His196 and is conserved in B1- and B3-type MBLs. The Zn2 site is made up of ligands Asp120, His121 and His263 and is different from the corresponding centre in B1-type MBLs. In addition, two water molecules (red spheres) complete the coordination spheres, one bridging the metal ions and one terminally coordinated to Zn2. Consequently, the two Zn^{2+} ions are four- and five-coordinate, respectively. The coordinates for the structure were taken from the PDB file with accession code 4AWY [216]

The remaining available coordination positions in both groups of enzymes are occupied by water molecules, including one that bridges the two Zn^{2+} ions. This water molecule is the likely nucleophile that initiates the hydrolysis of the β-lactam substrates [15,16,150,208]. No structural information has yet been reported for a member of the B4 subgroup, but catalytic data reported for the putative B4 MBL from *Serratia proteamaculans* (SPR-1) suggest that in its resting form this enzyme may be mononuclear and inactive, but that the addition of a substrate promotes the binding of a second metal ion, leading to the formation of a catalytically active dinuclear metal centre [217]. This substrate-promoted activation mechanism resembles that of another metallohydrolase, the organophosphate-degrading glycerophosphodiesterase from *Enterobacter aerogenes*, GpdQ [218-220].

Clinically, the capacity for β-lactamases to hydrolyse a wide range of β-lactam antibiotics represents a significant threat to global health [150,156]. In the case of SBLs, there are clinically useful inhibitors available, in particular clavulanic acid [221]. The co-administration of clavulanic acid with an antibiotic is a common practice to circumvent resistance [221]. In stark contrast, there are currently no clinically viable inhibitors available for MBLs. This, together with the fact that many MBLs are encoded on mobile genetic elements (plasmids, transposons) make them extremely dangerous agents [158,222,223]. MBLs can easily be "shared" between bacterial species, accelerating the spread of resistance dramatically [16,150,156,158,208,222-225].

An imipenem-degrading enzyme, initially identified in a pathogen in a hospital in Adelaide, Australia, and hence labelled Adelaide Imipenemase-1 (AIM-1), is a member of the B3 subclass of MBLs [158,216]. To date, AIM-1 is one of only a few members of the B3 subgroup that is encoded on a mobile genetic element in a major human pathogen (the Gram-negative *Pseudomonas aeruginosa*); the majority of B3-type MBLs have been found in environmental bacteria [158]. AIM-1 has the capacity to hydrolyse a broad spectrum of β-lactam antibiotics [158]. The crystal structure for wild-type AIM-1 (Figure 5.3) has been previously reported along with a preliminary characterisation of its catalytic parameters and substrate specificity [158,216]. Here, we employed a range of physico-chemical techniques to probe its reaction mechanism, with a particular view on highlighting variations that distinguish AIM-1 from other MBLs.

5.4 Results

5.4.1 Characterisation of the steady-state catalytic parameters of AIM-1

The substrate specificity of AIM-1 was probed previously, indicating that the enzyme is a broad-spectrum MBL [158]. At pH 7.5 the k_{cat} and k_{cat}/K_m for ampicillin, meropenem, cefuroxime and nitrocefin are 123.0(0.2) s^{-1} and 8.3(0.5) x 10^4 $s^{-1}M^{-1}$, 372.1(0.3) s^{-1} and 8.2(0.4) x 10^4 $s^{-1}M^{-1}$, 93.1(0.7) s^{-1} and 4.2(0.3) x 10^6 $s^{-1}M^{-1}$, and 240 (2) s^{-1} and 2.5 (0.7) x 10^6 $s^{-1}M^{-1}$, respectively, in reasonable agreement with values published previously for AIM-1 (no prior data for nitrocefin were available) [158]. We noted that for some substrates, independent of pH, high concentrations lead to a decrease of the catalytic activity (*i.e.* the rate *vs* [S] profiles deviate from Michaelis-Menten-type behaviour at high [S]; see [Equation 5.1] in the Experimental section and Figure 5.4. A similar observation was previously noted for the MBLs MIM-1 and MIM-2 (both belonging to the B3 subgroup) and CcrA from *Bacteroides fragilis* (representing the B1 subgroup) [226,227]. The estimated substrate inhibition constant K_i (using [Equation 5.2] is 106(10) μM, 202(50) μM and 87(15) μM for ampicillin, meropenem and cefuroxime, respectively, in reasonable agreement with K_i values reported for MIM-1 or MIM-2 (no substrate inhibition was observed with nitrocefin) [227].

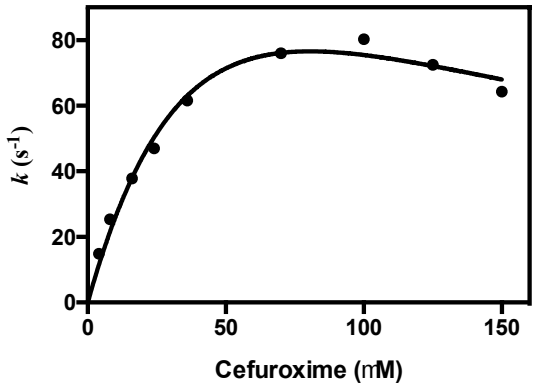

Figure 5.4: Rate vs substrate concentration profile for the hydrolysis of cefuroxime by AIM-1. Qualitatively similar data were obtained for ampicillin and meropenem. At high substrate deviations from Michaelis-Menten behaviour were observed. Each data set was thus analysed for low cefuroxime using the Equation 5.1 and for the entire range of substrate using Equation 5.2. The reaction with nitrocefin displayed Michaelis-Menten-type behaviour over the entire substrate range tested.

A similar behaviour was also observed for the reaction with the substrate biapenem, a compound that is structurally related to meropenem (Figure 5.2). Again, high concentrations of the reactant lead to deviation from Michaelis-Menten-type behaviour (Figure 5.5). However, uniquely for this reactant increasing concentrations of the substrate also lead to an increasing lag period before the steady-state rate is reached (Figure 5.5).

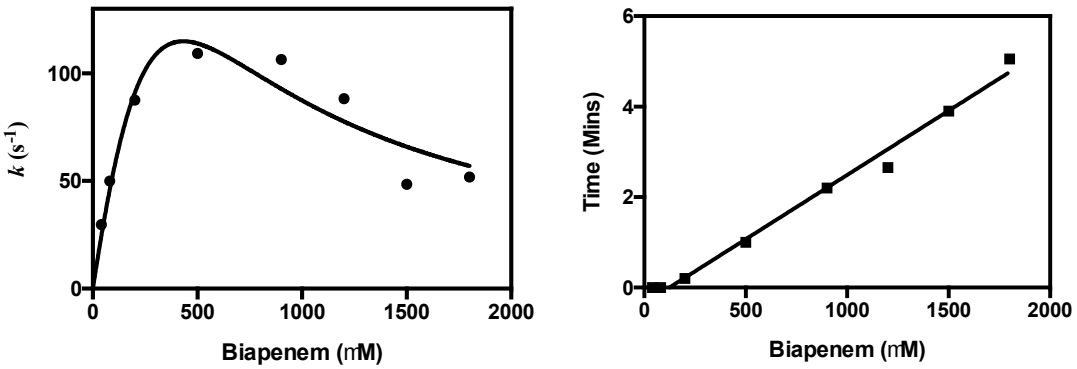

Figure 5.5: The activity vs [Biapenem] plot also illustrates a deviation from Michaelis-Menten-type behaviour at high substrate concentrations (left). Relevant catalytic parameters are kcat = 235(62) s-1, kcat/Km = 8.1(1) x 105 s-1M-1 and Ki = 906(452) µM. Furthermore, the higher the substrate concentration, the longer is the lag time before steady-state rates are attained (right).

The effect of pH on the catalytic properties of wild-type AIM-1 towards the selected subset of substrates representing major classes of β-lactam antibiotics (*i.e.* ampicillin, meropenem, cefuroxime and nitrocefin) was carried out to gain insight into catalytically relevant protonation equilibria. Measurements were carried out at suitably low substrate concentrations to minimise the inhibitory effect of the reactants. The pH dependence of k_{cat} and k_{cat}/K_m were analysed independently since they provide information about catalytically relevant protonation equilibria (*i.e.* pK_a values) of the enzyme-substrate (ES) complex, or free enzyme (E) or substrate (S), respectively [228]. For none of the four substrates tested did the k_{cat}/K_m ratio display pH dependence in the range between pH 6 to 10 (data not shown). In contrast, the catalytic rate (k_{cat}) is dependent on pH, but the effect is substrate specific (Figure 5.6).

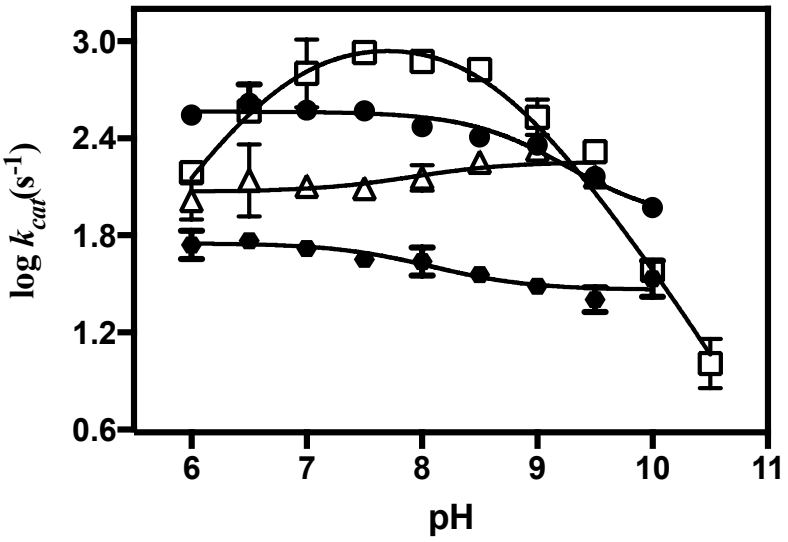

Figure 5.6: pH dependence of the catalytic activity (kcat) of AIM-1 for the hydrolysis of the following substrates: meropenem (circle), cefuroxime (hexagon), ampicillin (open triangle) and nitrocefin (open square).

For ampicillin and cefuroxime the effect of pH on k_{cat} is modest; while a deprotonation event leads to an increase in the reactivity towards ampicillin the opposite effect is observed for cefuroxime. An effect similar to that for cefuroxime is also observed for meropenem although the loss of activity with increasing pH is more significant. The slopes of the curves shown in Figure 5.6 are an indication of the presence of a protonatable residue that may contribute to the rate-limiting step of the reaction – a slope close to unity indicates that the residue is directly associated with the rate-limiting step, whereas the other extreme (*i.e.* pH independence indicated by a slope of zero) indicates that the respective residue is not involved in determining the overall rate of the reaction [228]. The pK_a values for the reactions with these three substrates (*i.e.* pK_{es} values) were estimated by fitting the data to an equation derived for a monoprotic model (Equation 5.3). Table 5.1 summarises relevant parameters. The pH

dependence of the reaction with nitrocefin is more complex displaying both an acidic (as observed with ampicillin) and an alkaline limb (as observed with meropenem and cefuroxime; Figure 5.6). The slopes of both limbs are close to unity indicating that at least two protonizable residues play an essential role in the AIM-1-catalyzed hydrolysis of nitrocefin. The profile adopts a characteristic bell-shaped curve and was fitted to Equation. 5.4; maximum activity is reached around pH 7.5-8.

Table 5.1: Catalytically relevant protonation equilibria for the AIM-1-catalysed hydrolysis of a range of substrates. pKes1 and pKes2 represent the acid dissociation constants of the enzyme-substrate complexes associated with the acidic and alkaline limbs of the pH profiles, respectively.

	Ampicillin	**Cefuroxime**	**Meropenem**	**Nitrocefin**
pK_{es1}	6.9(0.2)	-	-	6.7(0.4)
pK_{es2}		7.7(0.4)	9.4(0.8)	8.9(0.2)

D-Captopril is a known non-clinical, competitive MBL inhibitor with inhibition constants ranging from ~6 μM for MIM-1 (representing the B3 subgroup) to ~70 μM for CphA (a B2 subgroup MBL) [227]. The inhibitory effect of captopril on AIM-1 is similar to that reported for other MBLs from the B3 subgroup (Figure 5.7), although the best fit to the kinetic data suggests that two modes of inhibitor binding may be possible. The dominant mode of inhibition is competitive (K_{ic} ~ 19 μM), with an uncompetitive mode being approximately an order of magnitude weaker (K_{iuc} ~ 137 μM). Since the uncompetitive mode of binding has an affinity similar to that of the substrate inhibition constant 290 μM for cefuroxime; (*vide supra*) it is likely that captopril competes with the substrate for both its catalytically relevant and inhibitory sites. Interestingly, Cu^{2+} exerts an inhibitory effect on AIM-1 activity, which also has a competitive (K_{ic} = 11.9 μM) and uncompetitive (K_{iuc} = 35.5 μM) component (Figure 5.7).

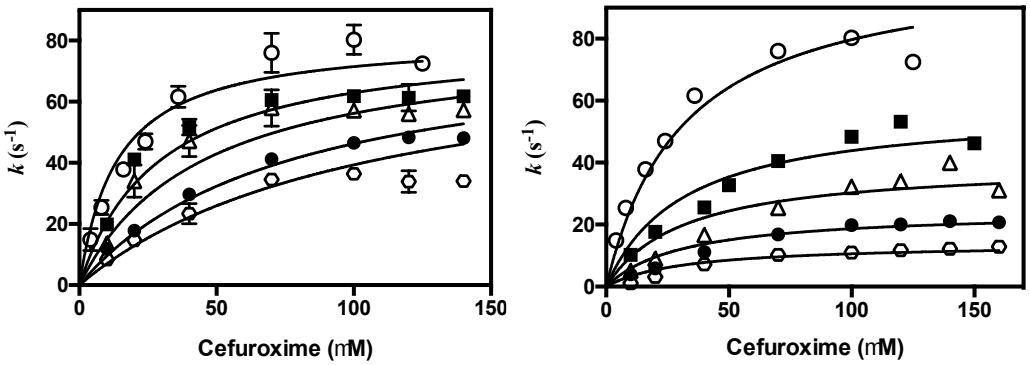

Figure 5.7: Inhibition of AIM-1 by Cu^{2+} (left) and captopril (right). The different concentrations of inhibitor tested for Cu^{2+} are zero (open circle), 0.04 µM (squares), 10 µM (open triangles), 20 µM (circles) and 30 µM (open diamonds). For captopril the concentrations are zero (open circle), 50 µM (squares), 100 µM (open triangles), 200 µM (circles) and 400 µM (open diamonds).

5.4.2 Metal ion replacement studies

Metal ion replacement studies with metalloenzymes frequently provide valuable catalytic insight, but the derivatives may also be useful for spectroscopic studies, in particular if a spectroscopically silent metal ion (*e.g.* Zn^{2+}) is replaced by a paramagnetic one (*e.g.* Co^{2+}). Here, the native Zn^{2+} ions could be easily removed from AIM-1 by incubation with a chelator solution. The apoform remained intact since the subsequent addition of Zn^{2+} led to a full reconstitution of the catalytic activity (data not shown). In a parallel experiment the apoenzyme was incubated with Co^{2+}. The catalytic parameters of the Co^{2+}-derivative of AIM-1 for the hydrolysis of cefuroxime at pH 7.5 are k_{cat} = 50.5 s^{-1} and K_m = 58.6 µM, compared to k_{cat} = 93.1 s^{-1} and K_m = 21.2 µM determined for the native Zn^{2+}-form under identical conditions (Figure 5.8).

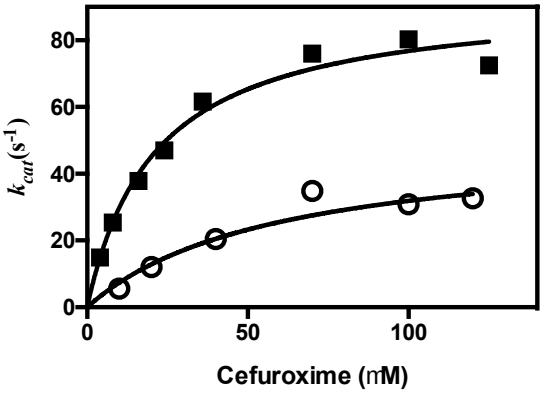

Figure 5.8: Comparison of the enzymatic activities of the Co^{2+}- and Zn^{2+}-derivatives of AIM-1 (open circles and squares, respectively) for the hydrolysis of the substrate cefuroxime.

The stoichiometry and binding affinities of these two metal ions were determined using isothermal titration calorimetry (ITC) (Figures 5.9 and 5.10). Two Zn^{2+} ions bind with similar affinity (~170 nM; Table 5.2). In contrast, only one site binds Co^{2+} with high affinity (~7 nM), while the other site has a considerably weaker affinity (~2 µM).

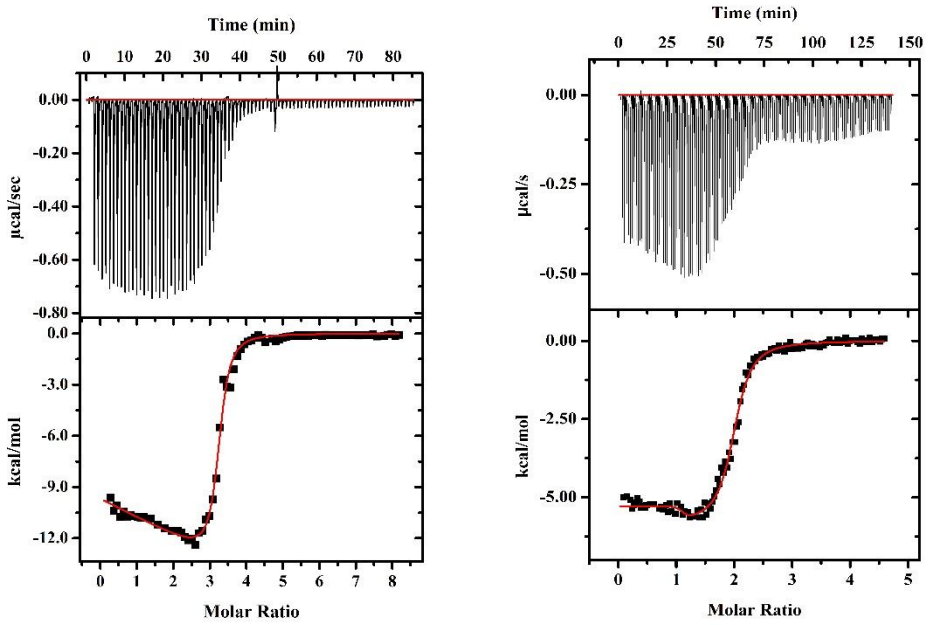

Figure 5.9: Representative ITC data for the interactions between AIM-1 (33 µM) and aliquots of 5 mM stock solutions of ZnCl2 (left) and CoSO4 (right). The data were fitted using a two-independent-binding-sites model.

Table 5.2: Stoichiometry and binding constants obtained from an ITC experiment whereby Zn^{2+} or Co^{2+} were added gradually to the apoform of AIM-1.

	Zn^{2+}		**Co^{2+}**	
	Site 1	Site 2	Site 1	Site 2
n_{ITC}	1.5(0.3)	1.3(0.2)	1.0(0.5)	0.9(0.2)
K_{ITC} (M^{-1})	4.15(1.1)x10^6	4.1(0.9) x10^6	1.14(0.2)x10^8	3.77(0.7)x10^5
K_{aff} (M^{-1})	5.69(0.2)x10^6	5.70(0.1) x10^6	1.40(0.2)x10^8	4.6(0.4)x10^5
K_d (µM)	0.17(0.05)	0.17(0.06)	0.0071(0.001)	2.16(0.3)
ΔG (kcal/mol)	-8.99	-9.02	-11.1	-7.72

[a]The robustness of the fits was tested by using a range of initial guess values including the optimised parameters from the Zn^{2+} titration for the Co^{2+} data set and *vice versa*. Independent of the initial guess the fits converged to the same optimised parameters.

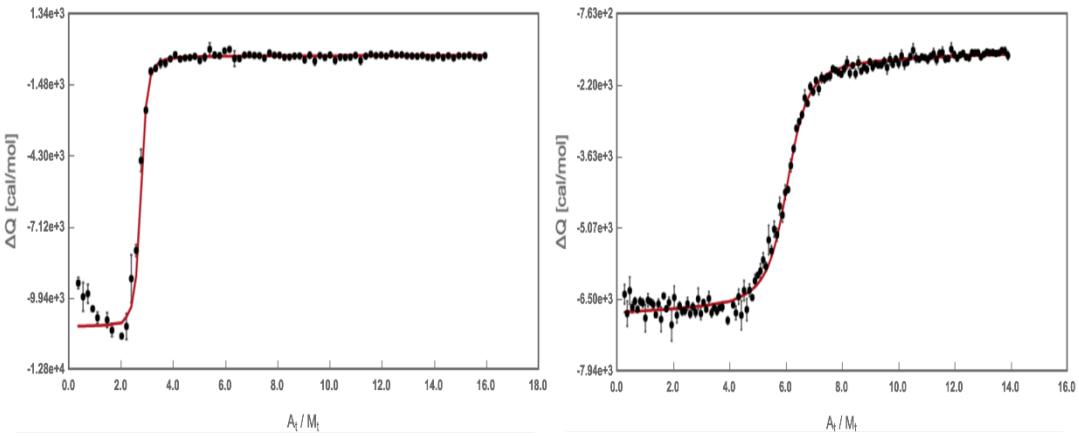

Figure 5.10: The error associated with each of the injections in the ITC experiments shown in Figure 5.9 were estimated using the Affinimeter software (https://www.affinimeter.com/).

5.4.3 Spectroscopic characterisation of the AIM-1 active site

The Co^{2+}-derivative of AIM-1 is well suited to investigate the catalytic centre of an active MBL using spectroscopic techniques. Here, magnetic circular dichroism (MCD) and continuous wave electron paramagnetic resonance (cwEPR) were employed to probe (i) the coordination environment of the metal centre in the resting, free enzyme and (ii) the effect (if any) of the inhibitor D-captopril on this centre.

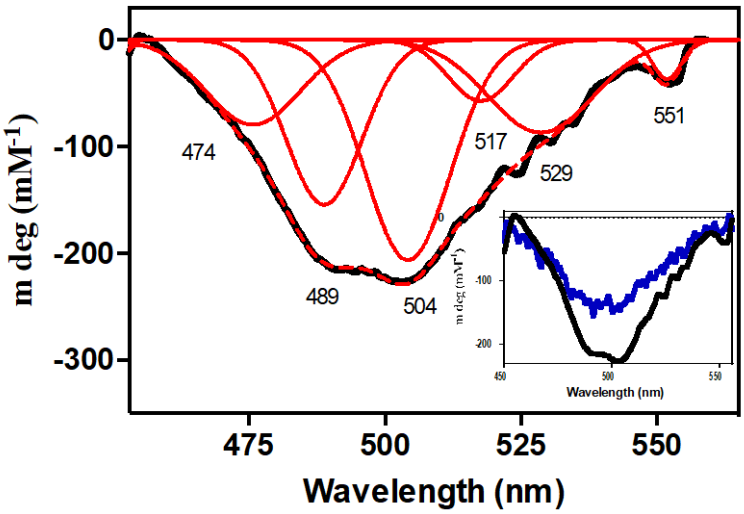

Figure 5.11: MCD spectrum (7 T) at 1.4 K of free AIM-1. Inset: the spectrum free AIM-1 (black) is compared with that recorded in the presence of D-captopril (blue).

The MCD spectrum of resting AIM-1 (Figure 5.11) could be fit to no fewer than six transitions between 450 and 600 nm. Calculations using the angular overlap model (AOM) were used to assign the individual transitions as described in detail elsewhere [218,220,229-232]. The coordinates for the calculations were taken from the crystal structure (PDB code: 4AWY [216]) and each Co^{2+} site was treated separately. The Racah parameters *C* and *B* were fitted individually and with $C = 4.7B$. The calculations indicate that the six transitions originate from two six-coordinate Co^{2+} species (Table 5.3).

Table 5.3: Summary of ligand field calculations

	Origin in O_h	*d-d* transition (nm)	
		Observed	Calculated
6-coordinate Species	$^4T_{1g} \rightarrow {}^2T_{1g}(G)$	474	469
	$^4T_{1g} \rightarrow {}^4T_{1g}(P)$	489	495
	$^4T_{1g} \rightarrow {}^4T_{1g}(P)$	504	503
	$^4T_{1g} \rightarrow {}^4T_{1g}(P)$	517	516
	$^4T_{1g} \rightarrow {}^4T_{1g}(P)$	529	525
	$^4T_{1g} \rightarrow {}^4A_{2g}$	551	549

Table 5.4: Spectroscopic parameters obtained from fitting VTVH MCD data collected in the absence or presence of the inhibitor D-captopril

	AIM-1		**AIM-1 + captopril**	
nm	491	504	491	504
J	0.12 cm^{-1}	0.11 cm^{-1}	0.20 cm^{-1}	0.12 cm^{-1}
D_α	≥ 50	≥ 50	≥ 50	≥ 50
D_β	5.6 cm^{-1}	5.5 cm^{-1}	4.8 cm^{-1}	5.1 cm^{-1}
E	0	0	0	0

This observation contrasts the coordination environment of the two Zn^{2+} ions in the crystal structure of AIM-1 (Figure 5.3) and suggests that in the Co^{2+} derivative additional water molecules may complete the coordination sphere of the two metal ions. The addition of captopril to the resting enzyme quenches the observed MCD intensity slightly but does not affect the individual transitions associated with the two metal ions (Figure 5.11, inset). It thus appears that D-captopril binding does not perturb the electronic structure of the dinuclear Co^{2+} centre significantly, an interpretation that is

in agreement with cwEPR data (see below).[1] Variable temperature, variable field (VTVH) MCD data for the transitions at 489 nm and 504 nm (Figure 5.12) were analysed using the dimer model [(229)]. Both transitions originate from the O_h low symmetry splitting of the ${}^4T_{1g} \rightarrow {}^4T_{1g}(P)$ energy levels. Relevant parameters are summarised in Table 5.4, and indicate that the two Co^{2+} ions have axial geometry (E/D ~0) and are weakly ferromagnetically coupled, independent of the presence of D-captopril, with an exchange coupling constant J estimated to ~0.1-0.2 cm^{-1}.

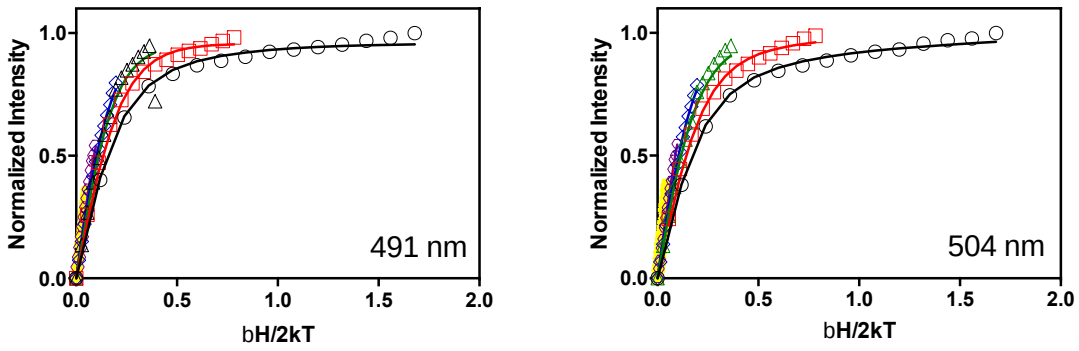

Figure 5.12: VTVH MCD data for the 489 nm and 504 nm transitions. Data were recorded at the following temperatures: 1.4, 3, 6, 12, 24 and 48 K (black, red, green, blue and yellow, respectively).

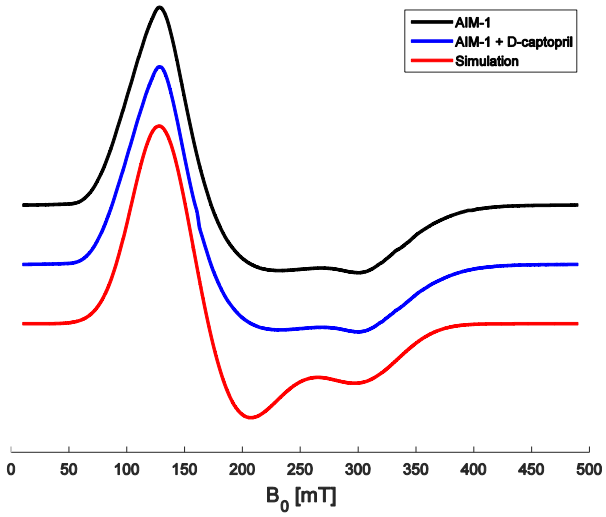

Figure 5.13: X-band cwEPR spectra of AIM-1 (top, black), AIM-1 + D-captopril (middle, blue), and a simulation assuming an effective S = 3/2 spin (bottom, red). Measurement conditions: T = 20 K, microwave power = 20 mW, modulation amplitude = 1 mT, modulation frequency = 100 kHz, microwave frequency = 9.619 GHz.

[1] An alternative explanation is that D-captopril occupies only a fraction of the available binding sites and induces strong antiferromagnetic coupling, leading to a reduction of the observed paramagnetism. However, with an estimated inhibition constant of ~20 μM it is estimated that the more than 500-fold excess of inhibitor will lead to almost complete saturation of the active sites.

EPR spectra for the Co^{2+}-derivative of AIM-1 were recorded as a function of microwave power in the absence and presence of D-captopril in both perpendicular and parallel mode (Figures 5.13 and 5.14). The representative spectra are shown in Figure 5.13, with and without the inhibitor D-captopril, and are very similar, a result consistent with the MCD data. This indicates that the interaction of the inhibitor with the paramagnetic centres is weak and below detection limits, probably as a result of the large linewidth of the cwEPR spectra. The data were simulated employing a Spin Hamiltonian model with an S = 3/2 spin, where the zero-field splitting is much greater than the electron Zeeman interaction, *i.e.* $|D| >> |\beta gBS|$ (in agreement with MCD data; Table 5.4). This model assumes that the interaction between the two Co^{2+} centres is small and below the large cwEPR linewidth. Optimisation of the principal g-values and the corresponding linewidths yielded the estimates $g_{\perp} = 2.35$, $\Delta g_{\perp} = 1.0$, and $g_{||} = 2.30$, $\Delta g_{||} = 0.9$, where D was found to be positive. Consequently, the EPR signal arises from transitions between the $M_s = \pm ½$ electron spin manifolds. The rhombicity of the zero-field splitting was found to be small, $E/D < 0.03$, again in good agreement with the MCD data. These parameters, in particular the sign of D, are indicative of a five- or six-coordinate Co^{2+} complex [128]. The EPR spectra and parameters for AIM-1 are similar to those from NDM-1, Bla2 from *Bacillus anthracis* and L1 from *Stenotrophomonas maltophilia* when loaded with two Co^{2+} ions [128,233].

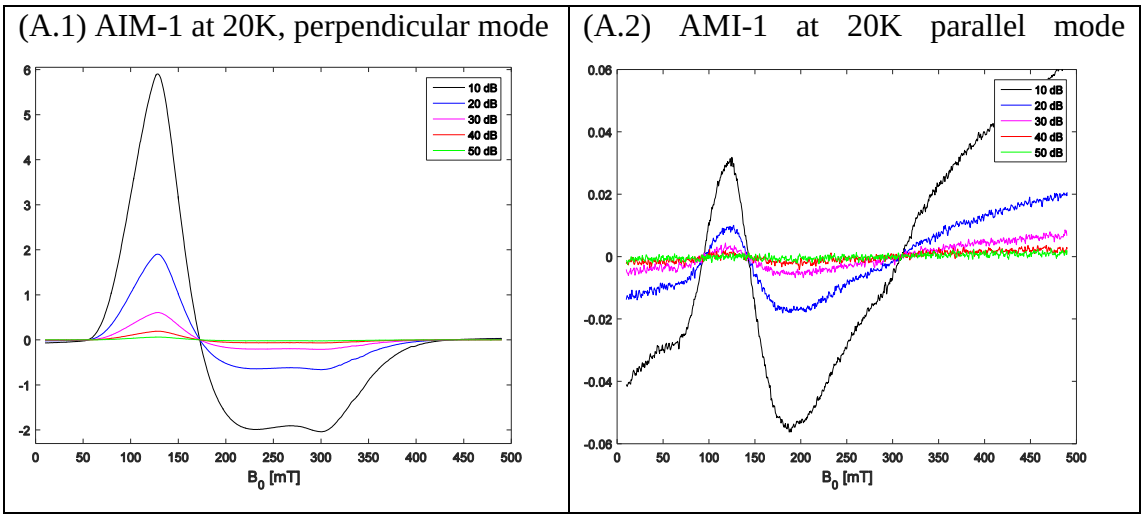

(A.3) AIM-1, 4.5K, perpendicular mode

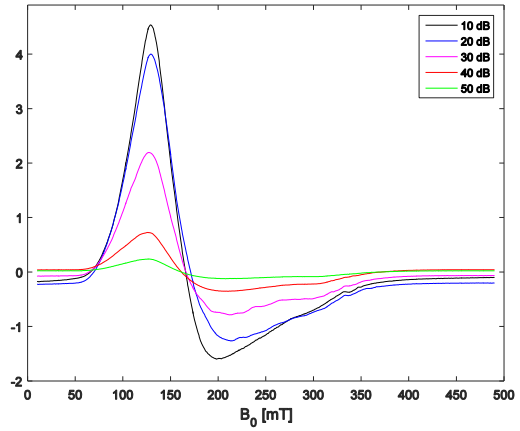

(A.4) AMI-1 at 4.5K parallel mode

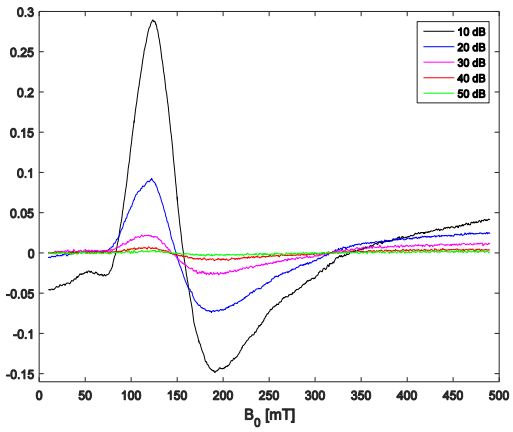

(B.1) AIM-1 + captopril, 20K, perpendicular mode

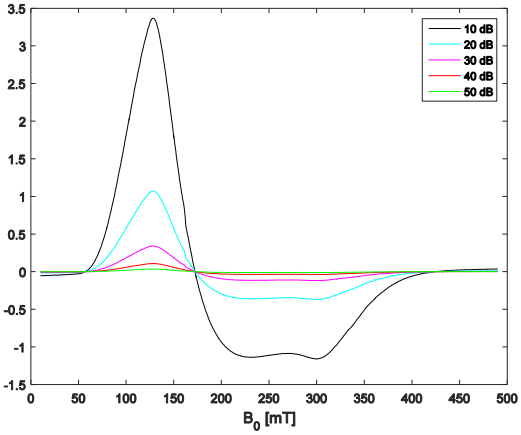

(B.2) AMI-1 + captopril, 20K, parallel mode

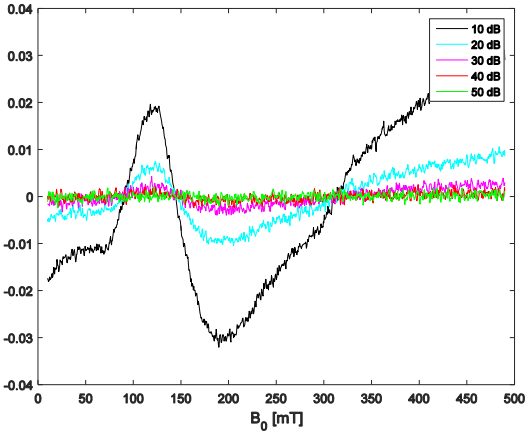

(B.3) AIM-1 + captopril, 4.5K, perpendicular mode

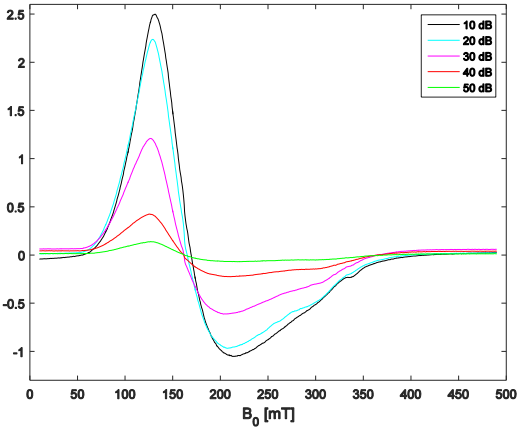

(B.4) AMI-1 + captopril, 4.5K, parallel mode

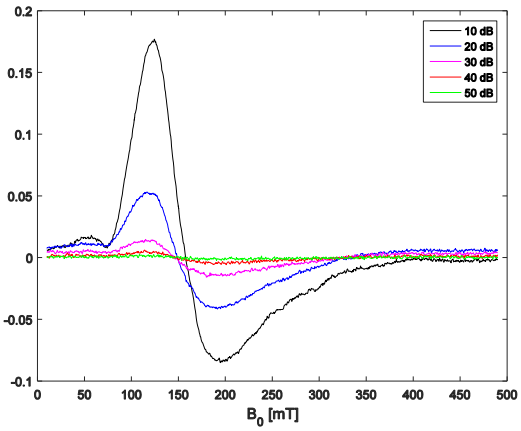

Figure 5.14: cwEPR spectra of AIM-1 without (A) and with (B) D-captopril measured at 4.5 K and 20 K, and at a range of microwave powers as indicated. Qualitatively similar results were obtained in both perpendicular and parallel modes. In perpendicular mode the cwEPR spectra at 20 K were not saturated (spectrum strength increases linearly with the square

root of the microwave power) over the range of microwave power, whereas at 4.5 K the spectrum at the highest microwave power of 20 mW (10dB) is saturated. In parallel mode no saturation is observed.

Since Cu^{2+} has an inhibitory effect on AIM-1 activity, displaying both a competitive and uncompetitive binding mode (see above and Figure 5.7) the EPR spectrum of the catalytically inactive Cu^{2+} derivative of AIM-1 was recorded to assess if two metal ions may bind in close vicinity (Figure 5.15). The lack of an apparent EPR signal indicates that the two Cu^{2+} ions are strongly antiferromagnetically coupled.

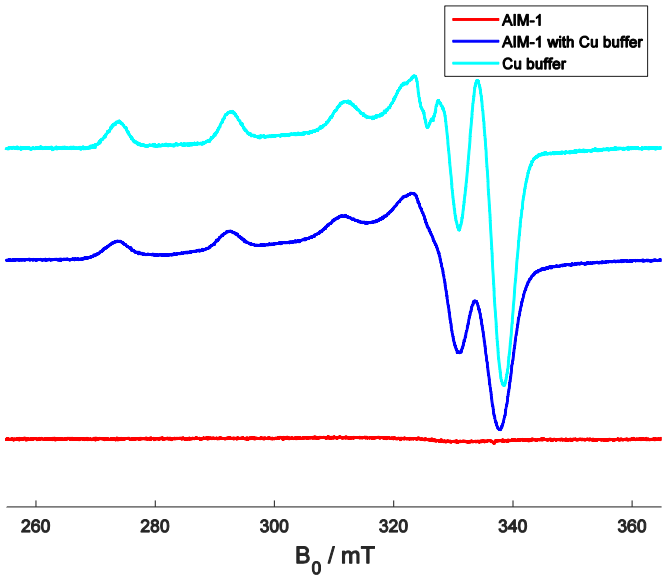

Figure 5.15: X-band (9.43 GHz) cwEPR spectra recorded at 130 K using a microwave power of 6.315 mW (15 dB), modulation amplitude of 0.1 mT and a modulation frequency of 100 kHz. The Cu^{2+}-loaded buffer is shown on top (cyan). In the middle (blue) a sample of apo-AIM-1 in the presence of excess Cu^{2+} is shown. The spectrum on the bottom (red) was recorded for the enzyme sample after the removal of excess Cu^{2+} on a gel filtration column. The lack of any signal is consistent with the presence of a strongly antiferromagnetically coupled dinuclear Cu^{2+} centre.

5.4.4 Rapid kinetics measurements

Pre-steady state kinetic data for the reaction of AIM-1 with the substrate nitrocefin were acquired in order to probe the initial phase of the catalytic cycle, but also to compare the mechanism of action with that of other MBLs, notably Bla2, NDM-1 and L1[128,233]. The reaction was monitored for 500 ms using a diode array detector (Figure 5.16, top panel). Three distinct transitions are observed; the bands at 390 nm and 485 nm are associated with intact and hydrolysed nitrocefin, respectively. The feature at 665 nm was previously associated with the ring-opened anionic intermediate of the reaction [234]. The concentration of the reaction intermediate reaches a maximum after ~50 ms and is below the limits of detection after ~250 ms. Progress curves for substrate depletion (390 nm), product formation (485 nm), and the emergence and disappearance of the intermediate (665 nm) were

simulated using KIMSIM with the models A and B shown in Figure 5.16. Suitable guess values were used as initial parameters for data fitting using the program FITSIM [235-237]. The values of k_1 and k_{-4} were set to the diffusion-controlled limit (10^8 $M^{-1}.s^{-1}$). The remaining parameters obtained from a global analysis (using either Model A or B) are listed in Table 5.5. The main difference between the two models is that the steps leading to the formation and decay of the intermediate (*i.e.* k_2 and k_3, Figure 5.16) are assumed reversible in Model A and irreversible in Model B (Model A has previously been employed to analyse comparable data for the MBLs L1 and NDM-1 [102,128]). While the formation rate for the intermediate differs in the two models (~170 s^{-1} *vs* ~240 s^{-1} in Models A and B, respectively), the decay rate remains virtually unchanged (~22 s^{-1}). For comparison, corresponding values reported for the related B3 subgroup MBL L1 are 190 s^{-1} and 38 s^{-1}, respectively [123].

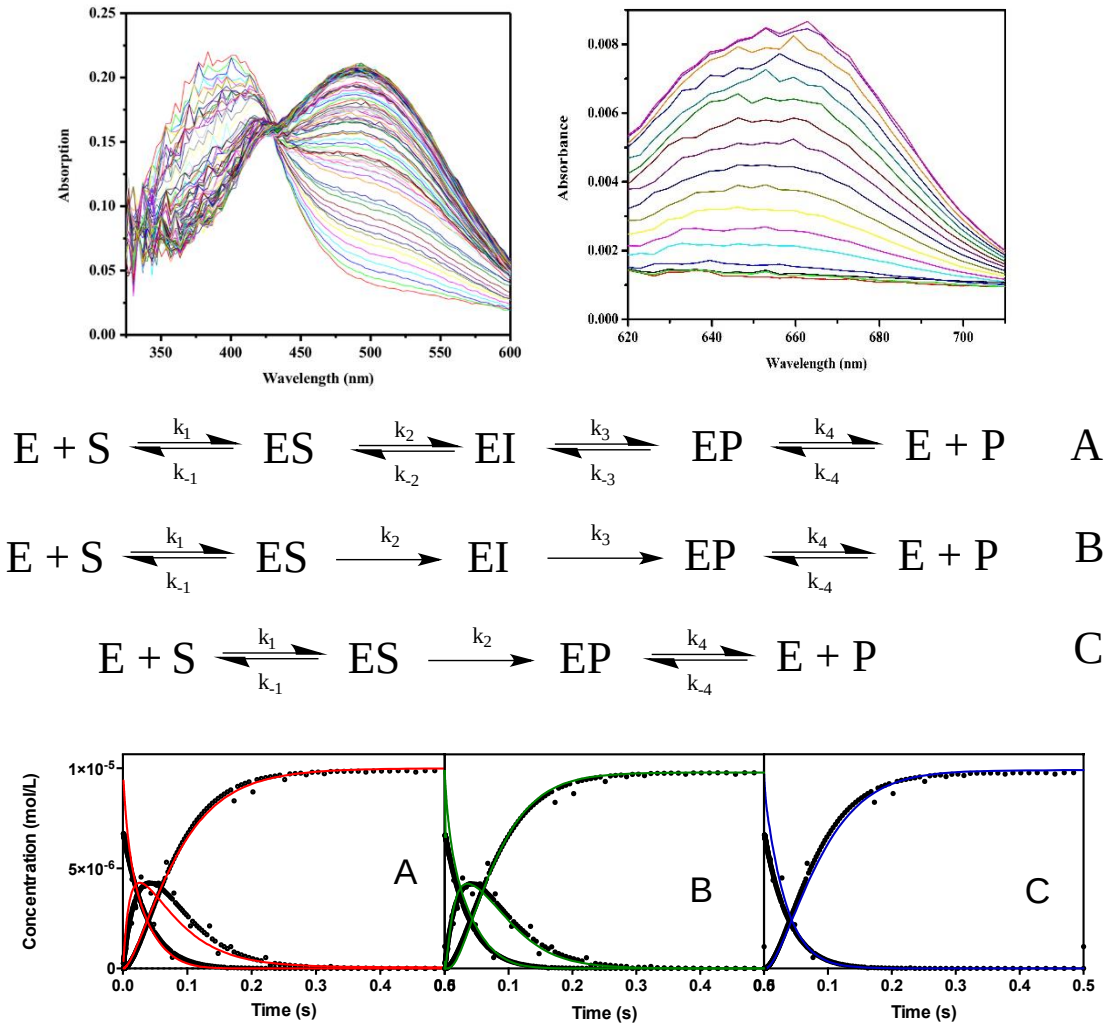

Figure 5.16: Rapid scan UV-Vis stopped-flow measurements at room temperature under single turnover conditions (10 μM AIM-1 and 16 μM nitrocefin). Experimental data are shown in the top row, recorded over a period of 0.5 s. The experimental data were analysed using several mechanistic models (middle row), and the corresponding fits to the time course of the concentrations for the substrate (measured at λ = 390 nm), the product (λ = 485 nm) and the reaction intermediate (λ = 665 nm) are shown in the bottom row.

Table 5.5: Rate constants for the reaction of AIM-1 with nitrocefin. The rate constants were obtained using the mechanistic schemes illustrated in Figure 5.16. kcat and KM represent the theoretical values calculated using the King-Altman approach to derive rate equations for the reactions illustrated in Models A, B and C.

	Model A	Model B	Model C
k_1 (M^{-1} s^{-1})	$1.0x10^8$	$1.0x10^8$	$1.0x10^8$
k_{-1} (s^{-1})	1078(51)	18.7(5)	252.0(15)
k_2 (s^{-1})	168.1(7)	238.4(10)	228.0(32)
k_{-2} (s^{-1})	0.2(0.1)		
k_3 (s^{-1})	22.8(3)	21.4(7)	
k_{-3} (s^{-1})	0.5(0.3)		
k_4 (s^{-1})	3500(25)	184.8(12)	200(21)
k_{-4} (M^{-1} s^{-1})	$1.0x10^8$	$1.0x10^8$	$1.0x10^8$
k_{cat} (s^{-1})[a]	20	18	106
K_M (µM)	1.7	50	30

[a]The corresponding k_{cat} and K_M values determined from steady-state measurements are 240 s^{-1} and 125 µM, respectively.

The microscopic rate constants listed in Table 5.5 can be used to calculate theoretical values for k_{cat} and K_m employing equations derived using the approach by King and Altman [228]. For both NDM-1 and L1 there is reasonable agreement between those theoretical values and the corresponding values measured in steady-state kinetic assays [102,128]. For AIM-1 neither model A nor Model B led to a good agreement between theoretical and experimental parameters (Table 5.5). Indeed, using a model that by-passes the intermediate altogether (Model C in Figure 5.16) leads to theoretical k_{cat} and K_m values that are in far better agreement with the corresponding experimental parameters (Table 5.5). The same model was previously employed to analyse the catalytic parameters for Bla2, an MBL for which no intermediate during the turnover of nitrocefin (*i.e.* no spectral changes at ~665 nm) was observed [233].

Previous studies with the MBLs NDM-1 and L1 demonstrated that fluorescence measurements may be used to monitor substrate binding [102,128]. The change in fluorescence during this reaction is associated with a tryptophan residue in the vicinity of the active site, *i.e.* Trp93 and Trp38 in NDM-1 and L1, respectively. This residue is conserved in AIM-1 (Trp38). The corresponding fluorescence

progress curve for the reaction with nitrocefin, recorded under single turnover conditions, is shown in Figure 5.17. A very rapid quench in fluorescence during the first ~10 ms of the reaction is followed by a slower recovery, complete after ~100 ms. The two transients were individually fitted to a single exponential resulting in k_{obs} values of 443(10) s^{-1} and 50(3) s^{-1} for the decay and return of the fluorescence, respectively. While the rate of decay is similar to that observed for NDM-1 and L1, the rate of regaining fluorescence intensity is considerably more rapid in AIM-1 than in the other enzymes (*i.e.* ~50 s^{-1} *vs* ~5 s^{-1}). Furthermore, since the rate of product formation (see k_2 for Model C in Table 5.5) exceeds that of the decay of the intermediate (*i.e.* k_3 for Models A and B) it appears that the mechanistic pathway via the observed intermediate is a possible albeit not an optimal route for substrate conversion for AIM-1. In summary, it appears that AIM-1 is capable of facilitating two alternative variants of a mechanism to convert nitrocefin to its product, one that resembles the strategy employed by L1 and NDM-1 in which the protonation of the ring-opened reaction intermediate is rate-limiting, and one that resembles the mechanism used by Bla2, where the protonation of the intermediate is not rate-limiting (and hence the intermediate is not observed experimentally). This interpretation may indicate distinct binding modes for the substrate in the active site and highlights a mechanistic flexibility available specifically to AIM-1.

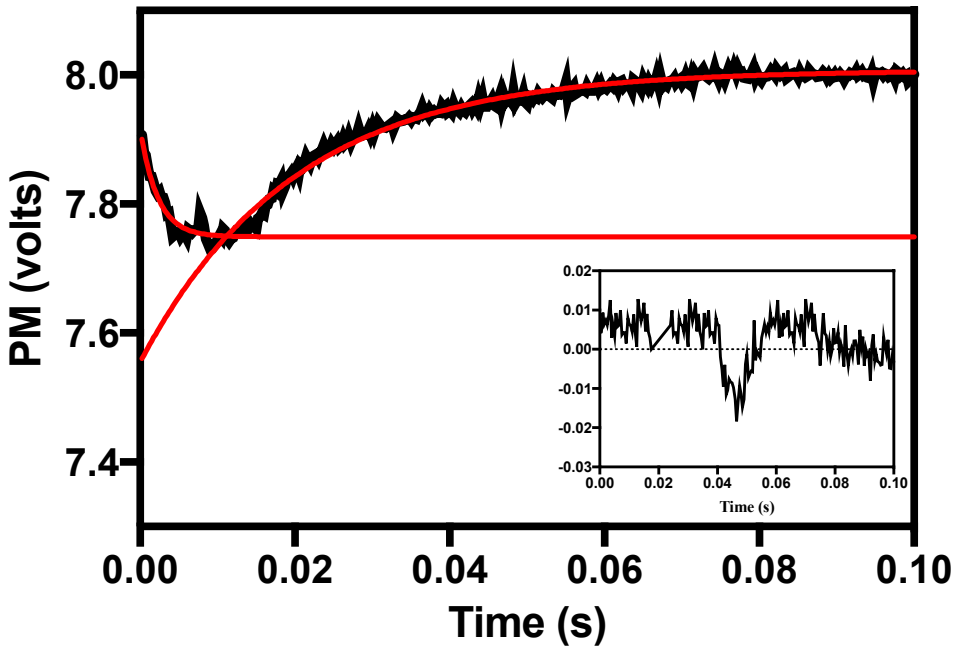

Figure 5.17: Pre-steady state stopped-flow fluorescence measurement recorded at room temperature under single turnover conditions (10 μM AIM-1 and 16 μM nitrocefin). Two distinct transients are observed, an initial rapid quench followed by a more gradual regain of fluorescence intensity (the inset shows the residuals of the fitting process).

5.5 Discussion

MBLs pose a considerable risk to global health, not least due to their broad substrate specificities, a reflection of structural plasticity in the vicinity of the catalytic centres of these enzymes. This plasticity may (i) prove beneficial for MBLs to adapt their mechanisms rapidly to new challenges (*i.e.* novel β-lactam antibiotics) and also (ii) hinder the design of clinically promising universal MBL inhibitors that may be developed into drugs to combat antibiotic resistance [238]. The mechanistic diversity of MBLs is illustrated in a comparison between the enzyme Bla2 from *B. anthracis* and L1 from *S. maltophilia* [128,233]. While Bla2 converts the substrate nitrocefin directly to its corresponding product (*i.e.* no intermediate is observed experimentally), L1 employs a mechanism whereby a metal ion-bound anionic intermediate is formed, the decay of which is the rate-limiting step of the reaction. Other MBLs, including NDM-1, CcrA from *B. fragilis* or BcII from *B. subtilis* appear to employ a mechanism similar to that of L1 [99,102,151,233,234]. Mechanistic diversity in MBLs is also observed when their catalytic properties are investigated at various pH values with a range of different substrates. Specifically, it was observed that MIM-1 and MIM-2, two MBLs from environmental microorganisms, display distinctly different pH optima, with MIM-1 preferring high pH values and MIM-2 a more acidic environment [26,227]. Furthermore, catalytically relevant protonation equilibria for reactions carried out with representatives from three of the major β-lactam substrates (*i.e.* ampicillin, cefuroxime and biapenem) vary significantly, and each of these substrates also inhibits the reaction at sufficiently high concentrations. These observations were interpreted in terms of variations with respect to substrate binding in the active sites of these enzymes and also in terms of the presence of a second, inhibitory binding site for the substrates [227].

5.5.1 AIM-1 is inhibited by its substrates and displays substrate-dependent mechanistic variations.

The steady-state catalytic parameters recorded for AIM-1 are consistent with the above interpretation. Similar to MIM-1, MIM-2 or CcrA, AIM-1 displays substrate inhibition (Figure 5.4). Furthermore, pH affects catalysis in a substrate-dependent manner (Figure 5.6). Interestingly, the behaviour of AIM-1 lies in between those of MIM-1 and MIM-2; while the hydrolysis of cephalosporin (*i.e.* cefuroxime) and carbapenam (*i.e.* meropenem) representatives are optimal at low pH (as observed for MIM-2) the reaction with ampicillin prefers high pH values (as observed for MIM-1). For the reaction with meropenem and cefuroxime, the respective pK_{es2} values are 9.4 and 7.7 (Table 5.1). While an unambiguous assignment of pK_a values in a complex environment such as the active site of an enzyme is rarely possible, the above values are consistent with a water molecule that is coordinated

to one of the metal ions in the catalytic site, *i.e.* Zn2 in Figure 5.3 [227,239,240]. In its deprotonated form, this water ligand would be likely to affect the catalytic rate, especially if it occupies a position that is needed for optimal substrate binding (due to reduced ligand exchange rates). Since the deprotonation event leads to an increase in reactivity towards ampicillin the corresponding equilibrium (pK_{es1} ~ 6.9) is likely to be associated with a residue different from that ascribed to the reactions with the above substrates. A possible candidate is a water molecule that bridges the two Zn^{2+} ions in the active site, the proposed nucleophile that initiates bond breakage [15,16,150,208]. Since the corresponding slope in the pH profile is less than 1 the chemical step in the reaction with ampicillin is, at best, only partially rate-limiting. The absence of the corresponding pK_{es1} in the reaction with cefuroxime and meropenem then, by analogy, indicates that here the chemical step (*i.e.* hydrolysis) is not contributing to the rate-limiting step at all. Thus, it is evident that different substrates interact in distinctly different modes with the active site leading to variations in the reaction mechanism. This conclusion is further supported by the analysis of the effect of pH on the reaction with nitrocefin (Figure 5.6). The observed behaviour appears to be a combination of those recorded for the other three substrates. Both acidic (pK_{es1}) and alkaline (pK_{es2}) limbs are present and their corresponding protonation equilibria contribute to the rate-limiting step (with slopes approximating unity). This interpretation is consistent with the rapid kinetics data (recorded at optimal pH) that indicate that the rate of substrate decay (*i.e.* k_2 in Table 5.5) is similar to the steady-state rate constant (*i.e.* k_{cat}) for this reaction (~200 s^{-1} *vs* ~240 s^{-1}).

The substrate-dependent catalytic behaviour discussed in the previous section highlights the mechanistic diversity and flexibility of MBLs. The substrate-induced inhibition observed for some of the reactants (except nitrocefin) then suggests the presence of more than one binding site or mode for those reactants. The possibility of two (or more) distinct binding sites of a substrate in the vicinity of the active centre of AIM-1 is also supported by the observed mixed-type inhibition by D-captopril (Figure 5.6). Furthermore, the presence of multiple binding sites or modes for substrates is consistent with the concentration-dependent lag in catalysis observed for the reaction with biapenem at substrate concentrations above K_m (Figure 5.5). While it is currently not known why this behaviour is only observed with biapenem (a rather poor substrate for AIM-1, with k_{cat} ~ 0.8 s^{-1}; Figure 5.5) the direct proportionality between substrate concentrations (in the range between 0.2 – 2 mM, *i.e.* above the K_m value for biapenem) and the lag period indicates a first-order process whereby a catalytically non-competent state may be populated at increasing substrate concentrations. This state could be a non-productive enzyme-substrate complex.

5.5.2 AIM-1 activity can be reconstituted with Co^{2+} but is inhibited by Cu^{2+}.

Metal ion replacement studies are frequently employed to probe the mechanism of metal ion-dependent enzymes. Here, we focussed mainly on Co^{2+} since (i) it is a convenient spectroscopic probe and (ii) it facilitates a comparison with Co^{2+}-derivatives of other MBLs (*i.e.* L1, Bla2, NDM-1) [102,128,233]. Similar to those MBLs AIM-1 is catalytically active in its Co^{2+}-substituted form (*vide supra*). To our knowledge there are no ITC data available for other MBLs that compare binding interactions of different metal ions. Our analysis indicates that the apoform of AIM-1 binds two Zn^{2+} ions with comparable affinity (~170 nM; Figure 5.9 and Table 5.2), whereas it binds one Co^{2+} with high affinity (~7 nM) and a second with considerably weaker affinity (~2 μM). A similar observation was previously reported for the B1-type MBLs BcII and Bla2; using spectrophotometric titrations it was shown that Co^{2+} binds with different affinities to the two binding sites in the active centre, although the difference appears to be no more than one order of magnitude [233,241]. The affinity of the weaker bound Co^{2+} is similar to the K_d value of this metal ion determined for MIM-1 and MIM-2 by measuring the catalytic activity as a function of added Co^{2+} [227]. The observation of varying metal ion affinities for Co^{2+} thus indicates that a bimetallic centre needs to be formed in order to reconstitute an active form of AIM-1.

According to the crystal structure of the Zn^{2+}-derivative of AIM-1 (Figure 5.3) the two metal ions (*i.e.* Zn1 and Zn2) are four- and five-coordinate, respectively, and are connected via a water molecule (the likely nucleophile in the reaction). Zn2 contains an additional water ligand and consequently it adopts a distorted trigonal bipyramid geometry, whereas Zn1 is tetrahedral. In contrast, MCD and EPR data (Figures 5.11 and 5.13) indicate that both Co^{2+} ions are six-coordinate; it is likely that extra water molecules complement the octahedral arrangement of the two metal ions. The change in geometry resulting from the metal ion replacement is consistent with variations in the observed K_m for cefuroxime (*i.e.* ~20 μM *vs* 60 μM for the Zn^{2+}- and Co^{2+}-derivatives of AIM-1, respectively). Surprisingly, the interaction of the Co^{2+}-derivative of AIM-1 with the inhibitor D-captopril does not lead to significant spectral changes (Figures 5.11 and 5.13). This may suggest that the inhibitor does not bind directly to any of the metal ions in the active site, or coordinates via its carboxyl group to one or both metal ions. This interpretation is in contrast to the available crystal structure of the complex between D-captopril and the MBL L1 (in its native Zn^{2+} form) that demonstrates that in that enzyme the thiol sulfur atom of the inhibitor displaces the bridging water ligand from the active site [76], but is in agreement with the mixed-type of inhibition observed for this compound (*vide supra*).

In contrast to Co^{2+}, Cu^{2+} is not able to reconstitute activity of apoAIM-1. Furthermore, a mixed-type of inhibition was observed when the effect of Cu^{2+} ions on native AIM-1 was probed (Figure 5.7). Since addition of Cu^{2+} to the metal-free apoform of AIM-1 did not reconstitute catalytic activity an uncompetitive mode of inhibition was expected, whereby the copper ions occupy the location of the Zn^{2+} ions in the catalytically active native form of the enzyme. The competitive mode of inhibition by Cu^{2+} is more difficult to reconcile with a mechanistic explanation but may be indicative of an alternative binding site for Cu^{2+}; upon binding of the metal to this site a conformational change may occur that prevents the substrate from binding to the active centre. The heat changes associated with Cu^{2+} titrations to both the apo and native forms of AIM-1 were too small to yield reliable estimates of the stoichiometry and affinity of bound Cu^{2+} (data not shown). However, cwEPR data of a sample of apoAIM-1 following the addition of Cu^{2+} indicates that two metal ions in close vicinity are bound, as evidenced by their strong antiferromagnetic coupling (*i.e.* the resulting spectrum is EPR-silent; Figure 5.15). This interpretation is in agreement with a study of MIM-1 and MIM-2 that demonstrated that close to two Cu^{2+} binds to tthose enzymes [227]. However, in contrast to AIM-1 the Cu^{2+}-derivatives of those enzymes are catalytically still active. These observations are thus another illustration of the mechanistic versatility inherent to MBLs. Independent of the precise mechanism of Cu^{2+}-promoted inhibition of AIM-1, the observation that this metal ion interferes with the activity of this enzyme raises the possibility that antibiotic-resistant pathogens expressing particular MBLs (such as AIM-1) may return to their sensitive state in presence of Cu^{2+}.

5.5.3 Substrate positioning may affect the rate of the AIM-1-catalysed hydrolysis of the substrate nitrocefin.

The above discussion highlights the fact that the active site of AIM-1 is versatile with respect to binding substrates and inhibitors, and that there may be more than one binding mode and/or locus for these reactants. This flexibility is also reflected in the reaction mechanism employed by this enzyme. Current mechanistic models for dinuclear MBLs are exemplified by Bla2 and L1/NDM-1, respectively [102,128,233]. Specifically, for the reaction with the substrate nitrocefin Bla2 catalyses a direct, one-step conversion of the substrate to product, whereas a two-step mechanism is operational in L1 and NDM-1, whereby a ring-opened anionic intermediate is formed. The decay of this intermediate is the rate-limiting step in the reaction. In each of the MBLs compared the rate of fluorescence quenching is two- to threefold more rapid than the rate of substrate consumption (in the case of AIM-1 the corresponding rates are ~450 s^{-1} vs ~200 s^{-1}; *vide supra*). This indicates that initially a catalytically non-competent ES complex is formed that is then transformed into an active Michaelis complex. From that point onward a variation is observed between L1/NDM-1 (with an

observed reaction intermediate) and Bla2 (no observed intermediate), a variation that may be associated with the protonation rate of the anionic intermediate[99,102,128,233]; in L1 and NDM-1 this protonation is rate-limiting, in Bla2 it is not. Insofar, AIM-1 appears to be unique in that both options appear to be operational (Figure 5.16). Thus, while in NDM-1, L1 and Bla2 nitrocefin may be positioned in a distinct conformation relative to the donor source of the proton (possibly a histidine residue in the active site), in AIM-1 the substrate may be bound in more than one orientation (hence affecting the rate of proton transfer). In the absence of a crystal structure with bound nitrocefin the precise position of these alternative binding modes remain obscure, however their existence may yet be another demonstration of the structural plasticity inherent to MBLs that may allow these enzymes to adapt rapidly to an ever increasing number of antibiotics. In this context it is also interesting to point out that a recent study with the MBLs BcII and VIM-2, two representatives from subgroup B1, indicated that metal ion composition may also affect the precise mechanism employed by these enzymes. In their native Zn^{2+}-form BcII behaves like Bla2 (*i.e.* no reaction intermediate observed), whereas VIM-2 resembles NDM-1 and L1 with an intermediate observable at 665 nm[242]. Upon replacement of Zn^{2+} by Fe^{2+} an intermediate is observed only in BcII. Hence, MBLs have indeed the ability to alter/adapt their mechanism of action, an observation which will have a profound effect on the design of potent and persisting inhibitors.

5.6 Conclusion

A major aim of current medicinal chemistry is to develop a universal inhibitor for MBLs as a strategy to combat antibiotic resistance. So far limited success has been achieved, largely due to differences in active site geometries and the resulting variations in substrate specificities, metal ion stoichiometry's and reaction mechanisms. AIM-1 may serve as a paradigm to illustrate these variations, facilitating the binding of substrates in different modes and/or sites, some catalytically competent, others inhibitory. Furthermore, in alignment with these different binding modes the enzyme may also employ mechanistic variations to convert substrates into products. As pointed out in an earlier study residue Gln157, unique in AIM-1 among known MBLs, may play an important role in mediating interactions with both the substrate and product [216]. While the precise origin of the mechanistic flexibility observed specifically for AIM-1 remains obscure it places this enzyme in an ideal position as a crucial target to identify or develop potentially universal MBL inhibitors. The search for inhibitors that bind to the enzyme under different conditions (*i.e.* different pH, different metal ion composition) may facilitate the design of compounds that are not easily rendered ineffective by small alterations in the substrate binding pocket. Furthermore, since AIM-1 encompasses

functional elements common for many MBLs such compounds may prove successful against most of the commonly targeted MBLs. In addition, at least for AIM-1, the observed inhibition by Cu^{2+} may provide an alternative avenue to devise strategies to reduce the impact of this enzyme on antibiotic resistance. As a step towards the design of leads it is now essential to obtain crystal structures of Co^{2+}- and Cu^{2+}-derivatives of AIM-1, in free form as well as in complex with D-captopril and, for the latter, in presence of substrates. Steps towards these aims are currently in progress.

5.7 Experimental Section

5.7.1 Materials

The AIM::pJ411 was cloned into the commercial vector (DNA 2.0). *Escherichia coli* BL21 (DE3) cells used for protein expression were purchased from New England BioLabs. All chemicals used, unless stated otherwise, were purchased from Sigma-Aldrich.

5.7.2 Recombinant expression and purification:

Wild-type AIM-1 was expressed and purified using a modified protocol of a previously published procedure [216]. In brief, BL21 (DE3) cells were transformed with the AIM-1-encoding plasmid PJ411. Cells were then grown in LB medium (containing 50 µg/ml kanamycin) at 37 °C until the OD_{600} reached 0.4-0.6. AIM-1 expression was induced by adding 50 µg/ml IPTG and lowering the temperature to 18 °C. The culture was then grown for another 48 hours.

The following steps for the protein purification were performed at 4 °C. Cells were harvested by centrifugation at 5000 rpm and then re-suspended in 20 mM HEPES buffer, 0.15 mM $ZnCl_2$, pH 7.5, accompanied with 60 mg of lysozyme and 30 mg protease inhibitor (EDTA-free) Roche. The cells were then lysed by sonication using five 30-second bursts of 60% maximum output power, and the supernatant was loaded onto a Hitrap Q FF 5 ml column. A linear NaCl gradient (0-1 M) was applied to elute proteins over two column volumes. Fractions containing activity against ampicillin were combined, concentrated and subsequently loaded onto a Hiprep 16-60 sephacryl S-300 HR gel filtration column, previously equilibrated with 20 mM HEPES buffer, 0.15 mM $ZnCl_2$, pH 7.2. Purified AIM-1 was stored in 10% glycerol at -20 °C. The protein concentration was determined by measuring the absorption at 280 nm (ε = 38,305 $M^{-1}cm^{-1}$ per monomer). An average purification yields approximately 1.5 mg of protein per litre of cell culture medium.

5.7.3 Generation of the Co^{2+} derivative:

The metal ion-free form of AIM-1 was prepared by incubation of 0.10 mg/mL of enzyme with 5 mM EDTA in 20 mM HEPES buffer (pH 7.0). The enzyme solution was allowed to stand for 24 hours at 4 °C. The chelating agent was then removed using an Econo-Pac 10DG (Bio-Rad) desalting column, previously treated with 20 mM buffer HEPES buffer, pH 7.2. The enzyme was then incubated with 100-fold excess of the desired metal ion (*i.e.* Co^{2+}) for 24 hours at 4 °C.

5.7.4 Steady-state catalytic assays:

Steady-state kinetic assays were performed at 25 °C using a Cary 50 Bio Varian UV-Vis spectrophotometer. The hydrolysis of cefuroxime (ε_{235nm} = 9,320 $M^{-1}cm^{-1}$), biapenem (ε_{293nm} = 7,600 $M^{-1}cm^{-1}$), ampicillin ($\varepsilon_{235\ nm}$= 820 $M^{-1}cm^{-1}$), nitrocefin (ε_{485nm} = 17,400 $M^{-1}cm^{-1}$) and meropenem (ε_{300nm} = 6,500$M^{-1}cm^{-1}$) was monitored by detecting the degradation of the substrate at the indicated wavelengths. The pH of the assays ranged from 5.5 to 10 and was adjusted using a multi-component buffer system which included 100 mM acetate, 100 mM MES, 100 mM HEPES, 100 mM CHES and 100 mM CAPS. Catalytic rates were measured as a function of the substrate concentration. The data was analysed by non-linear regression (Prism 6 software) using either the standard Michaelis-Menten equation (i.e. Equation 5.1) or a modified equation that takes into account the binding of a second substrate molecule to an inhibitory site (Equation 5.2) [228]:

Equation 5.1
$$v = \frac{V_{max} \cdot S}{K_M + S}$$

Equation 5.2
$$v = \frac{V_{max} \cdot S}{\left(K_M + S\left(1 + \frac{S}{K_i}\right)\right)}$$

In these equations v and V_{max} represent the measured and limiting rate, respectively. S is the substrate concentration while K_M and K_i represent the Michaelis and substrate inhibition constants, respectively. The pH dependence of k_{cat} and k_{cat}/K_m were analysed by fitting respective data to equations derived for mono- or diprotic systems (*i.e.* Equations 5.3 and 5.4, respectively), where H represents the proton concentration, K is the acid dissociation constant, and c is the pH independent value of y (*i.e.* k_{cat}) [228,243]

Equation 5.3 $$\text{Log (y)} = \frac{c}{1+\frac{H}{K}}$$

Equation 5.4 $$\text{Log (y)} = \frac{V\left(1+\frac{K_2}{H}\right)}{1+\left(\frac{H}{K_1}\right)+\left(\frac{K_2}{H}\right)}$$

Inhibition assays were conducted in the same manner as described above with the exception that increasing amounts of an inhibitor (*i.e.* captopril, Cu^{2+}) were added. The assays were performed in 20 mM HEPES buffer, pH 7.5, using the substrate cefuroxime. The enzyme concentration was 2.7 nM, and the inhibitor concentration ranged from 0 - 800 µM. The data were fitted to a general inhibition equation that allows for both a competitive and uncompetitive mode of inhibitor binding (Equation 5.5) [228]. K_{ic} and K_{iuc} represent the inhibitor dissociation constants for competitive and uncompetitive binding, respectively.

Equation 5.5 $$V = \frac{V[S]}{K_m\left(1+\frac{[I]}{K_{ic}}\right)+\left(1+\frac{[I]}{K_{iu}}\right)[S]}$$

5.7.5 Isothermal titration calorimetery:

The binding affinity and stoichiometry of Zn^{2+} and Co^{2+} for AIM-1 were determined by isothermal titration calorimetry (ITC). The experiments were performed with an ITC_{200} instrument from Microcal. The reaction cell was filled with 33 µM apoenzyme in 20 mM HEPES buffer, pH 7.5, under constant stirring at 1000 rpm at 25 °C. A solution of 5 mM of the desired metal ion was then titrated into the reaction cell, with a spacing of 60 s between injections to allow the heat in the cell to return to the baseline. The data were analysed using MicroCal Origin 7.0 software using an approach described elsewhere [195,231]. The heat released during each injection was fitted to an equation that was derived from a model including two individual binding sites [195,231].

5.7.6 Stopped flow UV-Vis and fluorescence measurements:

Stopped-flow kinetic measurements in both the absorbance and fluorescence mode were performed on an Applied Photophysics SX20 Stopped-Flow spectrophotometer equipped with a photodiode array and fluorometer detector. All experiments were carried out in Chelex-treated 20 mM HEPES buffer, pH 7.5, at 25 °C. Data were recorded using nitrocefin as the substrate under single turn-over conditions (*i.e.* final concentrations before triggering the reaction were 16 μM AIM-1 and 20 μM nitrocefin). The transients observed in the fluorescence measurements were analysed by fitting them to first order exponential equations included in the Applied Photophysics software package. The absorbance data were converted into concentrations using 1 cm as cell path length and the extinction coefficients for nitrocefin (ε_{390nm} = 11,500 $M^{-1}cm^{-1}$**)**, its product (ε_{485nm} = 17,420 $M^{-1}cm^{-1}$**)** and a previously observed reaction intermediate (ε_{665nm} = 32,000 $M^{-1}cm^{-1}$**)** [99,102,128,233,244]. The data were simulated using KIMSIM software and fitted using FITSIM [235,236,245]. The models used for fitting are shown in Figure 5.16.

5.7.7 Magnetic circular dichroism:

The Co^{2+} derivative of AIM-1 was prepared as described above. The excess of Co^{2+} was removed using a desalting column, pre-equilibrated with 50 mM Tris.HCl buffer, pH 8.0. The derivative was then diluted with glycerol to a final concentration of 60%/40% (v/v) glycerol/buffer. The final protein concentration in the samples used to record magnetic circular dichroism (MCD) spectra was ~0.7 mM. The sample was placed into a 0.62 cm path length nickel-plated copper sample cell with quartz windows. Data were acquired with a JASCO J815 spectropolarimeter, equipped with an Oxford Instruments SM4000 cryostat/magnet. Standard spectra were measured at 7.0 T and 1.3 K. Variable-temperature, variable-field (VTVH) MCD data were collected at increments of 0.5 T from 0 to 7.0 T and at temperatures of 1.4, 3, 6, 12, 24 and 48 K. The final spectra were converted to wavenumbers and fitted to a minimum number of Gaussian peaks to achieve the final composite spectrum using GRAMS AI software package. The data were analysed as described elsewhere [22,218-220,229-232].

5.7.8 Electron paramagnetic resonance spectroscopy:

Low temperature X-Band EPR spectra were recorded on a Bruker Elexys E600 EPR spectrometer equipped with an Oxford Instruments ESR900 helium flow cryostat. Spectra were recorded at 9.64 GHz ($B_0 \perp B_1$) and 9.38 GHz ($B_0 \,||\, B_1$) using an ER4116DM dual-mode cavity, with 10 G (1 mT) magnetic field modulation at 100 kHz. Spin Hamiltonian parameters were estimated from computer simulations carried out using XSophe (Bruker Biospin), assuming $H_0 = \beta B_0 g\hat{S}/\hbar + \hat{S}D\hat{S}$, where S =

3/2, $|D| >> |\beta gBS/\hbar|$, and where $D > 0$ implies the $M_S = \pm 1/2$ Kramers doublet lies lowest and all observed EPR transitions are from this doublet, and $D < 0$ implies the $M_S = \pm 3/2$ Kramers doublet lie lowest and all observed EPR transitions are from this doublet.

5.8 Acknowledgements.

This research was supported by Project Grants from the NH&MRC (APP1084778) and Australian Research Council (DP150104358) and Future Fellowships (FT120100694 and FT120100421) awarded to GS and JH, respectively. CS acknowledges financial support in form of an APA Scholarship from the University of Queensland and NM is grateful to the Science Foundation Ireland for funding in form of a President of Ireland young Researcher Award (SFI-PIYRA). JAL and WH thank the National Science Foundation (USA) for financial support from grants CHE1303852 and CHE0820965 (MCD instrument).

Chapter 6

Comparison of the active site structures of several BMHs using magnetic circular dichroism (MCD)

Publications associated with this chapter:

A) **Reaction mechanism of the metallohydrolase CpsB from Streptococcus pneumoniae, a promising target for novel antimicrobial agents.**

Dalton Trans.; accepted, epub ahead of print, May 26, 2017: DOI: 10.1039/c7dt01350g. http://dx.doi.org/10.1039/C7DT01350G

Marcelo Monteiro Pedroso, **Christopher Selleck,** Jessica Bilyj, Jeffrey R. Harmer, Lawrence R. Gahan, Nataša Mitić, Alistair Standish, David L. Tierney, James L. Larrabee, Gerhard Schenk.

B) **Characterization of a highly efficient antibiotic-degrading metallo-β-lactamase obtained from an uncultured member of a permafrost community.**

Metallomics; accepted, epub ahead of print, Jul 27, 2017: DOI:10.1039/c7mt00195a.

http://dx.doi.org/10.1039/C7MT00195A

Marcelo M. Pedroso, **Christopher Selleck,** Charmaine Enculescu, Jeffrey R. Harmer, Nataša Mitić, Whitney R. Craig, Waleed Helweh, Philip Hugenholtz, Gene W. Tyson, David L. Tierney, James A. Larrabee, Gerhard Schenk.

[1]School of Chemistry and Molecular Biosciences, The University of Queensland, St. Lucia, Queensland, 4072, Australia
[2]Department of Chemistry and Biochemistry, Middlebury College, Middlebury, Vermont 05753, USA
[3]Centre for Advanced Imaging, The University of Queensland, St. Lucia, Queensland, 4072, Australia
[4]Department of Chemistry, Maynooth University, Maynooth, Co. Kildare, Ireland
[5]Research School of Chemistry, Australian National University of Canberra, ACT, 0200, Australia
[6]Department of Chemistry and Biochemistry, Miami University, Oxford, Ohio 45056, USA

6.1 Abstract:

Magnetic circular dichroism (MCD) is a technique that can provide information about the coordination environment of metal ions within proteins. Importantly, MCD may provide insight into the in-solution active site structure of a metalloenzymes when artefacts in the corresponding solid-state structure are suspected due to the crystallisation process. In previous chapters it was demonstrated that BMHs with rather diverse functions (*i.e.* phosphatases and MBLs) employ similar mechanistic strategies for their reactions. Here, we expand this analysis to compare the active site structures of several BMHs by MCD. One of these enzymes is LRA-8, identified in a microbial community in the remote and frozen environment of Alaska. LRA-8 has a substrate profile and catalytic properties similar to well-known MBLs, despite emerging from an environment that has been subjected to minimal human interference. Also included are MIM-1 and MIM-2 (who's crystal structures were discussed in Chapter 4), two enzymes with potent MBL activity despite originating from marine microorganisms that would have experienced minimal exposure to anthropogenic pollution. Furthermore, MIM-1 and MIM-2 have also been shown to be potent lactonases. This comparative study also included CpsB from *Streptococcus pneumoniae*, a phosphatase that has become a promising target for the development of novel chemotherapeutics to combat antibiotic resistance. As a suitable paramagnetic probe for MCD studies Co^{2+} was employed. Despite considerable functional differences between the four enzymes, an analysis of their coordination environment by MCD demonstrates that the immediate active site geometry in these enzymes is rather similar, thus demonstrating that a common active site motif is capable of supporting a diverse range of catalytic reactions.

6.2 Introduction

Magnetic circular dichroism (MCD) provides a convenient avenue to probe the structure and function of metalloenzymes by spectroscopic techniques. In particular, MCD has been demonstrated to be useful in structure/function studies of a range of BMH (see Chapter 5 for an example) [1,246-252] and provides insights into the geometric and electronic structure of these systems in solution. MCD is valuable as both supportive information for other spectroscopic techniques and may be used to provide structural information in cases where crystal structures are not available.

MCD arises from the difference in absorption between left and right circularly polarised light ($\Delta A = A_{(-)} - A_{(+)}$) by a sample positioned within a strong magnetic field that is orientated parallel to the emitted light source. While CD requires an optically active sample and relies on structural features

(chirality) to distribute the electronic charge, MCD arises purely from the electromagnetic interactions between the charges within the sample and the externally applied field. Furthermore, the ΔA in the MCD results from a magnetic perturbation of the electronic states involved in the absorption transition by the Zeeman effect, defined by the magnetic optical rotation observed when a plane of linear polarized light is rotated in a collinear magnetic field in terms of B and C leading to Equation 6.1 [253,254].

Equation 6.1
$$\frac{\Delta A}{E} = \gamma\beta H\left[A_1\left(\frac{-\partial f(E)}{\partial E}\right) + \left(B_0 + \frac{C_0}{\kappa T}\right) f(E)\right]$$

Equation 6.1 is derived from the "Born-Oppenheimer" approximation, where $f(E)$ is the linear shape of the function of the energy. It describes the observed Franck-Condon envelope of the absorption band. The A, B and C terms are quite complex, involving the electric and magnetic dipole operator matrix elements with the particular electronic state involved in the transitions, and will be discussed below.

The A-terms arise when excited state degeneracy occurs (*i.e.* the allowed atomic transitions from the allowed $^1S_0 \rightarrow {}^1P_{-1,0,+1}$ include $0 \rightarrow +1$ and $0 \rightarrow -1$). In the absence of a magnetic field the absorption bands for the polarized light A_L and A_R coincide and $\Delta A = 0$. Under an applied magnetic field, the excited state of ^1P_j levels split with energy given by the following relation: $\Delta E = g\beta H$ (Zeeman splitting). If g is positive $^1P_{-1}$ level will be the lowest and the ΔA will be negative. For higher energies $^1S_0 \rightarrow {}^1P_{+1}$ and ΔA will be positive.

The B-terms arise from a mixing of the applied magnetic field with the zero-field wave-functions, where both the excited and the ground state wave-functions can be affected. In these cases, the degeneracy can be removed by placing the paramagnetic centre (*e.g.* Co^{2+}) in a low symmetry environment (*i.e.* enzyme ligands), in which, the angular momentum is "quenched" by low symmetry field imposed by the bound ligands.

The C-terms are similar to the A-terms with the exception that the degeneracy is in the ground state. Consequently, the transition is strongly temperature-dependent. In this chapter, I will focus on enzyme samples whose active sites contain reconstituted bimetallic Co^{2+} centres. Apart from being paramagnetic, Co^{2+}-reconstituted metal ion centres have been studied for a number of BMHs and

related model complexes, and thus they provide a well-studied platform for structural comparisons [23,144,254-258].

Co^{2+} displays coordination flexibility, encompassing the ability to form octahedral, tetrahedral, square pyramidal, trigonal bipyramidal and trigonal prismatic complexes [259]. This coordination flexibility makes Co^{2+} particularly useful for analysing the electronic structures of active sites within metalloenzymes. Relevant to this study, MCD allows for the simple distinction between five- and six-coordinate Co^{2+} centres in metallo-systems of interest. Five-coordinate Co^{2+} species with N and O ligands typically have multiple negative MCD bands between 650 and 450 nm, with a maximum around 550 nm (±30 nm). In contrast, six-coordinate Co^{2+} with similar ligands have a sharp and intense negative MCD band at 500 nm (±15 nm), which is often split in low symmetry environments [254]. The general shape and intensities of these MCD bands are typically conserved for both monomeric and dimeric active sites, as demonstrated in recently reported MCD investigations of a series of model complexes [72,144,258,260-265]. Variable temperature, variable field (VTVH) MCD data provide, apart from zero-field splitting parameters of the cobalt species, also insight into the exchange coupling in a dimeric centre [254].

In this Chapter MCD spectroscopy was employed to garner mechanistic and structural insights of various BMHs. CpsB (a phosphatase) represents an interesting case where the available crystal structure information suggests the presence of a third metal weakly bound in the active site, a result conflicting with metal ion binding data [266] (associated publication A). MIM-1 and MIM-2 (previously introduced in Chapter 4) have been shown by crystallography to have an active site structure very similar to that of the B3-subgroup MBL AIM-1 (introduced in Chapter 5); however, in contrast to AIM-1 MIM-1 and MIM-2 originate from environmental, non-pathogenic microorganism and possess an alternative function in form of lactonase activity [26]. Similar to the two MIM proteins, LRA-8, described in more detail below, originates from a non-pathogenic microbial environment, the permanently frozen tundra in Alaska. Previous studies (associated publication B) have demonstrated that this enzyme is indeed a potent MBL, and in absence of crystallographic data we investigated its active site structure with MCD.

6.3 Materials and methods

6.3.1 Materials:

All chemicals used, unless stated otherwise, were purchased from Sigma-Aldrich. *Escherichia coli* BL21 (DE3) cells used for protein expression of MIM-1, MIM-2 and LRA-8 were purchased from New England BioLabs. Similarly, *E. coli* LEMO21(DE3) host cells purchased from New England BioLabs were used for the protein expression of CpsB.

6.3.2 Expression and purification of CpsB

CpsB(SP0347; TIGR4) cloned under the control of a pBAD promoter (pWQ553) was transformed into *E. coli* Lemo21(DE3) for expression via heat shock. The cells were then grown in LB medium containing ampicillin (50 µg/mL) and chloramphenicol (30 µg/mL) at 37 °C until the OD_{600} reached 0.4-0.6. Recombinant protein expression was induced by adding L-arabinose (0.1 % m/v) whilst maintaining the incubation temperature at 30 °C with constant shaking (200 rpm) for 24 h.

The following steps for the protein purification were performed at 4 °C. Cells were harvested by centrifugation and lysed using a French press (1000 psi). The CpsB construct contains an N-terminal hexahistidine tag allowing purification of the soluble fraction via a Ni^{2+} affinity column (Ni^{2+}-IMAC resin), equilibrated with buffer containing 50 mM Tris HCl, pH 8.5, 5 mM of mercaptoethanol, 150 mM sodium chloride and 20 mM imidazole.

The protein was eluted with an isocratic gradient utilising the previous buffer solution with increased concentration of imidazole (200 mM) and 10% glycerol. The final protein concentration was measured via UV at 280 nm using ε_{280} = 20400 $M^{-1}.cm^{-1}$ (monomeric unit). Approximately 30mg of purified protein were recovered per litre of LB medium.

6.3.3 Expression of MIM-1, MIM-2 and LRA-8

MIM-1, MIM-2 and LRA-8 were expressed and purified using a previously published procedure [137]. *E. coli* BL21 (DE3) cells were transformed with the plasmid PJ411 (containing encoding genes for each enzyme, respectively) via heat shock. PJ411 plasmids were purchased from DNA 2.0. Cells were then grown in LB medium (containing 50 µg/ml kanamycin) at 37 °C until the OD_{600} reached 0.4-0.6. Recombinant protein expression was induced by adding 50 µg/ml IPTG and reducing the incubating temperature to 18 °C for 48 hours with shaking (200 rpm).

6.3.4 Purification of MIM-1 and MIM-2

The following steps for the protein purification were performed at 4 °C and were detailed in Chapter 4. *E. coli* cells were harvested by centrifugation at 5000 rpm and then re-suspended in 20 mM Hepes buffer, 0.15 mM $ZnCl_2$, pH 7.5. 60 mg of lysozyme and 30 mg protease inhibitor (EDTA-free) were added to the protein solution with stirring for 20 minutes. The cells were then lysed by sonication using five 30-second bursts of 60% maximum output power, and the supernatant was loaded onto a Hitrap Q FF 5 ml column. A linear NaCl gradient (0-1 M) was applied to elute proteins over two column volumes.

Fractions containing activity against cefuroxime were combined, concentrated and subsequently loaded onto a Hiprep 16-60 sephacryl S-300 HR gel filtration column, previously equilibrated with 50 mM TRIS buffer, 0.15 mM $ZnCl_2$, pH 7.2. Purified protein was stored in 10% glycerol at -20 °C. Protein concentration was determined via UV at 280 nm (ε = 36,815 $M^{-1}cm^{-1}$ and 41,285 $M^{-1}cm^{-1}$ per monomer for MIM-1 and MIM 2 respectively). The polypeptide was recovered without the periplasmic sequence attached and yielded roughly 5mg of protein per litre of LB medium.

6.3.5 Purification of LRA-8

The following steps for the protein purification were performed at 4 °C. Cells were harvested by centrifugation at 5000 rpm and then re-suspended in 50 mM Tris.HCl, pH 8.5, 5 mM β-mercaptoethanol, 150 mM NaCl buffer. 1 mg/mL protease inhibitor (ETDA free) and 60 mg lysozyme were added with stirring for 20 minutes and then the cells were lysed via sonication.

The LRA-8 construct also contained an N-terminal hexa-histidine tag allowing for initial purification of the supernatant on a 25 mL HiTrapQ FF Ni^{2+} affinity column (Ni^{2+}-IMAC resin; GE Healthcare), equilibrated with 50 mM Tris.HCl buffer, pH 8.5, containing 150 mM NaCl, 5 mM β-mercaptoethanol and 20 mM imidazole. The protein was eluted with an isocratic gradient utilising the previous buffer solution with increased concentration of imidazole (500 mM) and 10% glycerol.

Fractions containing MBL activity were combined, concentrated and further purified via loading onto a Hiprep 16-60 sephacryl S-300 HR gel filtration column, previously equilibrated with 50 mM Tris.HCL buffer, pH 8.5, 0.2 M NaCl and 0.15 mM $ZnCl_2$. The final protein concentration was measured via UV at 280 nm using ε_{280} = 42315 $M^{-1}.cm^{-1}$ (monomeric unit). An average expression resulted in a yield of 12 mg of purified LRA-8 per litre of LB medium.

6.3.6 MCD spectroscopy

Prior to recording MCD data Co^{2+} derivatives of each of the protein samples had to be prepared. The preparation of the apo-enzyme was performed following a previously published procedure [267-269] by adding 10 mM EDTA in 20 mM Hepes buffer, pH 7.0, to the purified enzyme (CpsB, MIM-1, MIM-2 and LRA8). After 24 h incubation at 4 °C the chelating agent was removed using a desalting column (Econo-Pac 10DG from Bio-Rad) that was equilibrated with 20 mM Hepes buffer, pH 7.0. Subsequently, three equivalents of Co^{2+} were added to the metal-free protein solution and the mixture was incubated over night at 4 °C. The excess of Co^{2+} was removed using a desalting column pre-equilibrated with 50 mM Tris.HCl buffer, pH 8.0.

For spectroscopic measurements this solution was diluted with glycerol to a final concentration of ~ 0.7 mM (*i.e.* a 3:2 glycerol:buffer mixture). The samples were transferred to a 0.62 cm path length nickel-plated copper sample cell with quartz windows. The MCD system used has a JASCO J815 spectropolarimeter and an Oxford Instruments SM4000 cryostat/magnet. Data were initially collected at 7.0 T and 1.4 K. Variable-temperature, variable-field (VTVH) data were measured at increments of 0.5 T from 0 to 7.0 T and at temperatures of 1.4, 3, 6, and 12, 24 and 48K. The experimental spectra were plotted as a function of wavenumbers and fitted to a minimum number of Gaussian peaks to achieve the final composite spectrum using the GRAMS AI software package. The data were subsequently analysed as described in detail elsewhere [268-274].

6.4 Results and discussion

6.4.1 Active site structure of CpsB

CpsB is a metal-dependent protein tyrosine phosphatase that belongs to the polymerase and histidinol phosphatase (PHP) enzyme family, whose metal ion composition remains ambiguous [275,276]. Reported crystal structures for CpsB suggest three Mn^{2+} ions (M1, M2 and M3 in Figure 6.1) are prevalent in the active site [52]. The electron density suggests that the third metal ion (M3) might be weakly bound due to its lower occupancy. Although uncommon, catalytic active sites possessing more than two metal ion have been seen before for some metallohydrolases [231].

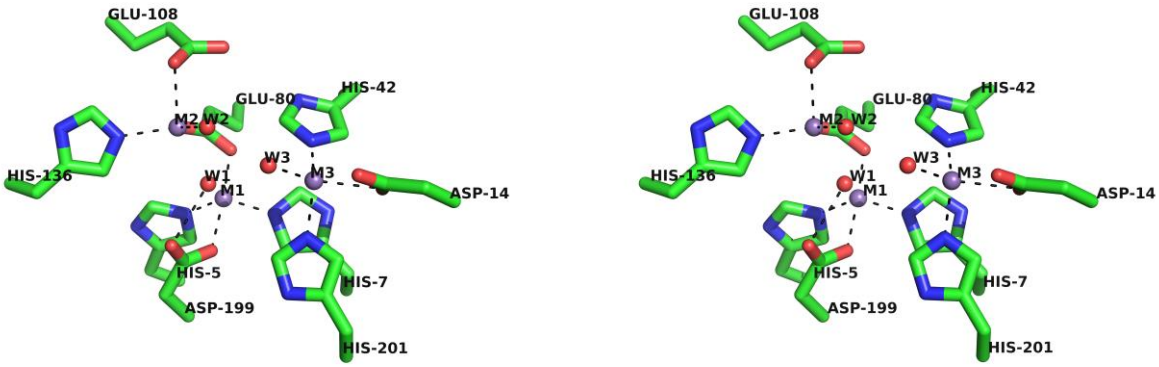

Figure 6.1: Metal binding site of CpsB (stereo pair). Residues that interact with metal ions M1, M2 and M3 (purple spheres) are shown. The water ligands W1, W2 and W3 are depicted as red spheres.

In terms of the reaction mechanism it has been proposed that the catalytic cycle in CpsB involves an esterolysis-initiating hydroxide nucleophile that is doubly Lewis-activated by coordination to M1 and M2. This is similar to related phosphotriesterases [5], MBLs [15,206], ureases[14] arginases [238] and some PAPs [161]. The presence of the third metal ion within the active site was proposed to play an important role in substrate recognition [52].

In order to probe the active site of CpsB the MCD spectrum of the Co^{2+}-derivative of the enzyme was recorded; the resulting spectrum could be fitted to no fewer than seven transitions between 400 to 600 nm (Fig. 6.2; Table 6.1). Calculations using the angular overlap model (AOM) were used to assign the individual transitions as described in detail elsewhere.[229] The coordinates for the calculations were taken from the crystal structure (PDB code 2WJE) and each metal site was treated separately. The calculations indicate that the seven transitions are linked to the presence a six-coordinate (6C) and a five-coordinate (5C) Co^{2+} species, similar to what was observed for the glycerophosphate diesterase GpdQ.[220,273]

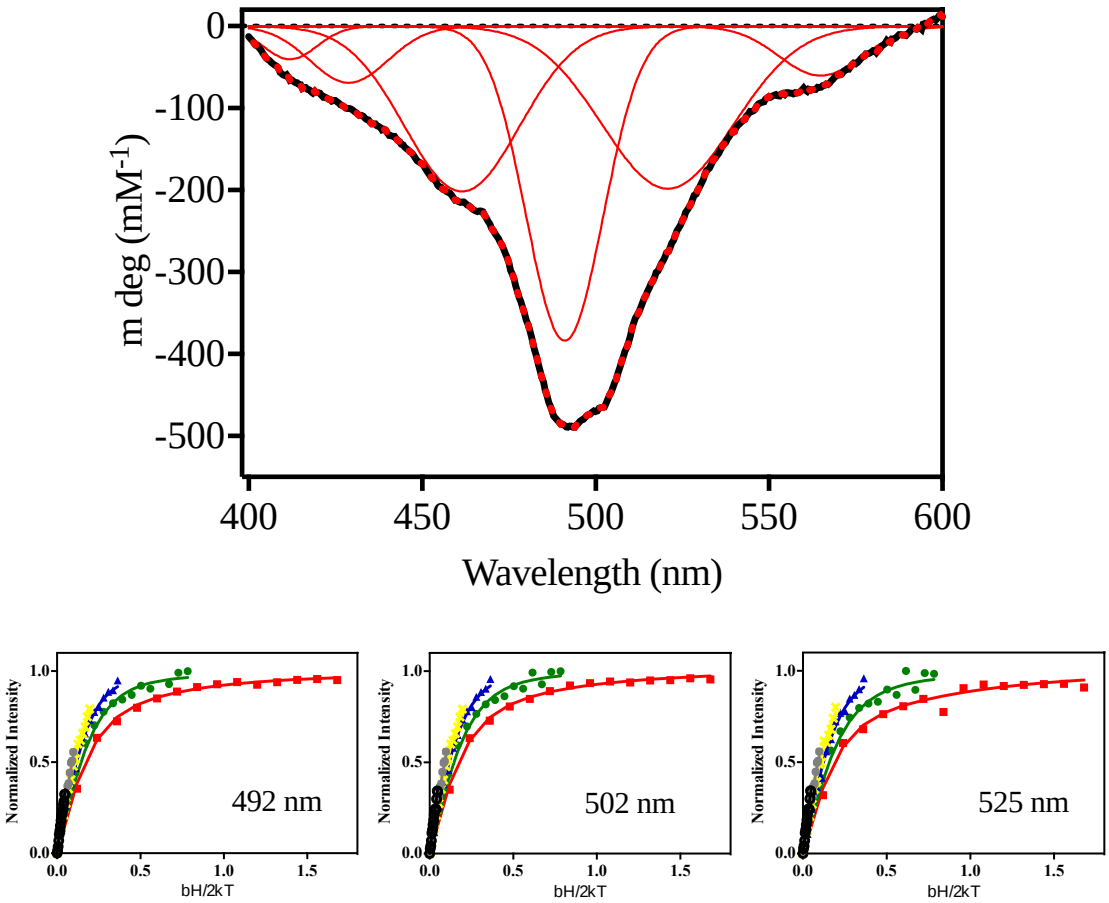

Figure 6.2: MCD spectrum (7 T, 1.4 K) of CpsB at pH 8.5 (top) and fitted VTVH MCD data (bottom) for the transitions observed at 492, 502 and 525 nm. Temperatures of red, green, blue, yellow, grey, black represent data collected at 1.4, 3.0, 6.0, 12.0, 24.0 and 48.0 K, respectively

The VTVH MCD data for each of the seven transitions were extracted and assessed for quality; only those bands which gave rise to high-quality data (*i.e.* those at 492, 502, and 520 nm) were selected for fitting, using the dimer model (Figure 6.2; Table 6.2).[229] Based on its energy and fitted electronic parameter ($D\alpha \geq 50$ cm^{-1}), the transition at 492 nm arises from the $^4T_{1g} \rightarrow {}^4T_{1g}(P)$ transition in the parent O_h symmetry of a high-spin 6C Co^{2+} ion. The structure is distorted, causing the 6C peak to split into two bands (*i.e.* 461 and 492 nm). The two small peaks at higher energy (*i.e.* 411 and 428 nm) are due to spin-forbidden doublet transitions in this Co^{2+} species, whose energies are enhanced through spin-orbit coupling. The VTVH MCD analysis of the 492 nm band indicates that the corresponding cobalt species is exchange-coupled (J = 0.12 cm^{-1}) to a 5C Co^{2+} associated with both the 502 nm and the 520 nm transitions (both of which have identical electronic structural parameters; Table 6.2). This assignment is also supported by the VTVH MCD analysis of the 502 and 520 nm bands, resulting in a $D\beta$ = 7.7 cm-1 (Table 6.2), a value typical for 5C Co^{2+} species.[229] Similar to the MBL AIM-1 (Chapter 5) the dimetallic Co^{2+} centre in CpsB is thus weakly ferromagnetically

coupled.[201,277] The AOM calculations also support the assignment of the 565 nm transition to a 5C cobalt.

Table 6.1: Summary of ligand field calculations*

Species	Origin in O_h or D_{3h}	*d-d* transition (nm)	
		Observed	Calculated
α- Co^{2+}	$^4T_{1g} \rightarrow {}^2T_{1g}(G)$	411	406
(B = 890, $\varepsilon\sigma$ = 3,020)	$^4T_{1g} \rightarrow {}^2T_{1g}(G)$	428	429
	$^4T_{1g} \rightarrow {}^4T_{1g}(P)$	461	450
	$^4T_{1g} \rightarrow {}^4T_{1g}(P)$	492	483
β- Co^{2+}	$^4A_2 \rightarrow {}^2E``(P)$	520	535
(B = 710, $\varepsilon\sigma$ = 4,030)	$^4A_2 \rightarrow {}^4A_2(P)$	565	560

These values correspond to transitions arising from a 6C, α, and a 5C, β, species. The Racah parameter C was fitted according to C = 4.6B. The units for B, C and εσ are cm^{-1}

Table 6.2: Spectroscopic parameters obtained from fitting VTVH MCD data using the dimer model.

Parameter	492 nm	502 nm	520 nm
J (cm^{-1})	0.12	0.11	0.11
Dα (6C) (cm^{-1})	≥ 50	≥ 50	≥ 50
Dβ (5C) (cm^{-1})	6.28	7.7	7.7
E (α, β metal) (cm^{-1})	0	0	0

Interestingly, the catalytically active Co^{2+}-reconstituted CpsB does not provide and spectroscopic evidence of a third metal ion, indicating that the binding of the third metal ion (coordinated to Glu108, His136, Glu80 and W2 in Figure 6.1) may in fact be a crystallographic artefact only, and does not represent the enzyme active site in solution.

6.4.2 Active site structures of MBL-like proteins from environmental microorganisms

Antibiotic resistance is rapidly increasing with an increasing number of organisms displaying the ability to produce β–lactamases, and hence resist commonly used β-lactam antibiotics. The number of MBL-like proteins identified through functional metagenomics studies is rising in parallel to increasing antimicrobial resistance in bacteria generally. The distribution of these enzymes within soil and water samples appears to be widespread ranging from densely populated areas to the remote wilderness of uninhabited places. The prevalence of MBL-like enzymes that can confer resistance to

enzymes is alarming, and adds complexity to the fight against antimicrobial resistance globally. Examples of such enzymes include MIM-1 from *N. pentaromativorans*, MIM-2 from *S. agarivorans* (both discussed in Chapter 4) and LRA-8, identified among several β-Lactam Resistance in Alaskan soil genes, respectively [26,136].

Kinetically, the MIM enzymes are proficient Penicillinases, with MIM-1 typically preferring alkaline conditions whilst MIM-2 prefers acidic conditions [26]. Similarly, LRA-8 confers resistance towards various cephalosporin- and penicillin-type antibiotics (see Chapter 6, associated publication B). The MIM proteins in particular have been shownto be functionally promiscuous; In addition to their MBL activity they are efficient lactonases (most similar to N-acylhomoserine lactonases[26]). MIM-1 appears to be the first of this class of enzymes to be catalytically efficient with Ca ions as cofactors [26].

Crystallographic investigations of the two MIM proteins were reported in Chapter 4. The enzyme are most similar to B3-type MBLs, containing a dimetallic Zn^{2+} active site. The metal ion ligands are His116, His118 and His196, and Asp120, Cis221 and His263 for the Zn1 and Zn2 ions, respectively (identical to the ligands of AIM-1; see Chapter 5). The two metal ions are bridged by a water molecule, whilst a second water is terminally coordinated to Zn2. No crystal structure of LRA-8 is yet available. However, based on sequence homology it was expected that LRA-8 would have an active site highly similar to that of B3-type MBLs (Figure 6.3).

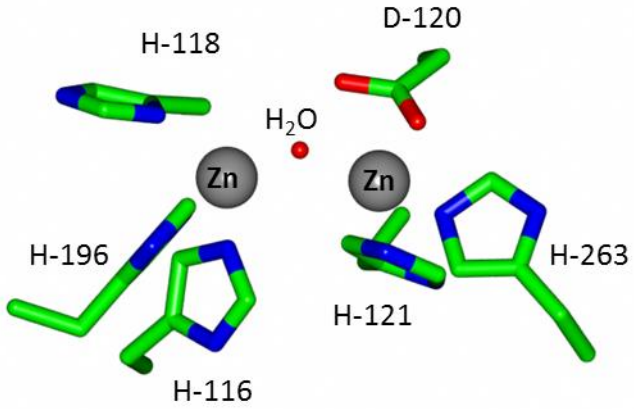

Figure 6.3: : Active site of a typical B3-type MBL (reference structure: AIM-1 (PDB 4AWY).[216,278]

The native Zn^{2+} ions could easily be replaced with paramagnetic Co^{2+}, and similar to other MBLs, the replacement of Zn^{2+} by Co^{2+} leads to an active form of these enzymes with moderately reduced

catalytic activity, a slight impact on substrate binding and reduced competitive inhibitory effect of D-captropril [26]. Irrespective of the catalytic changes, MIM-1, MIM-2 and LRA-8 were suitable candidates for spectroscopic investigation via our previously mentioned and reported methodology.

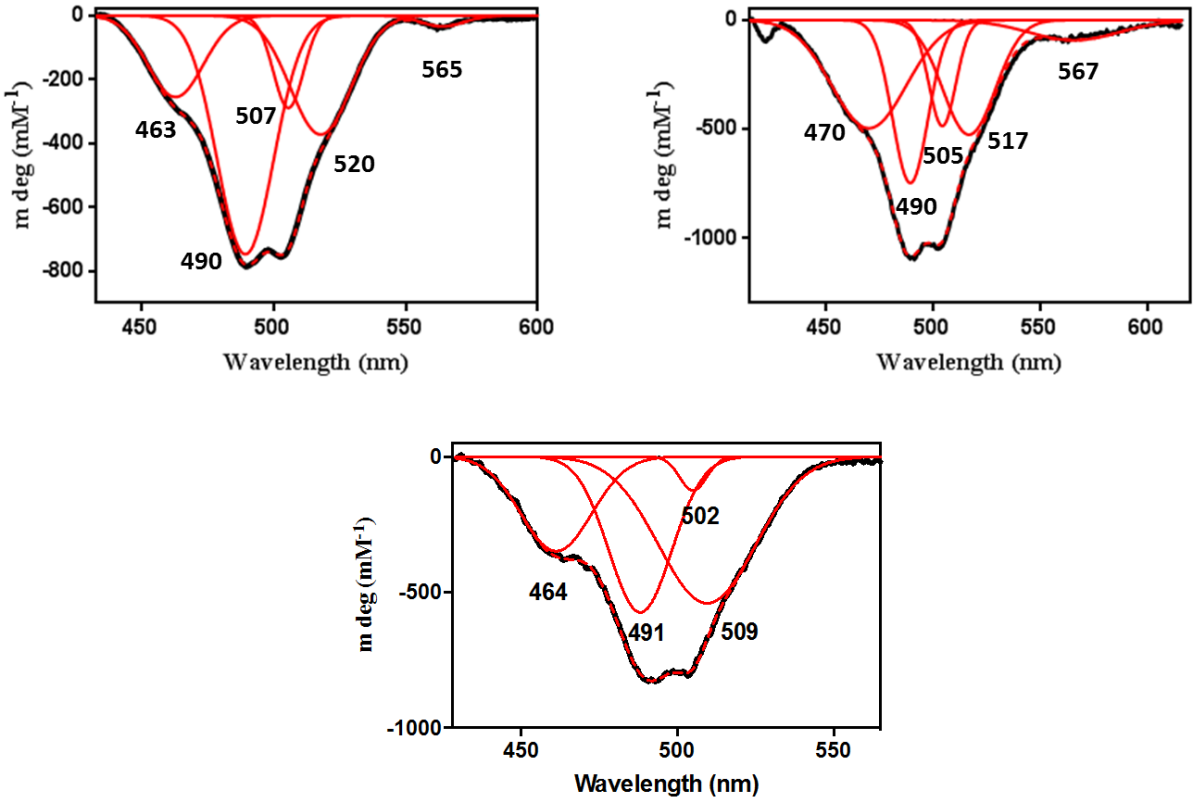

Figure 6.4: Gaussian-resolved MCD spectra (7 T, 1.4 K) of the B3-type MBLs from environmental microorganisms; MIM-1 (top left), MIM-2 (top right) and LRA-8 (bottom).

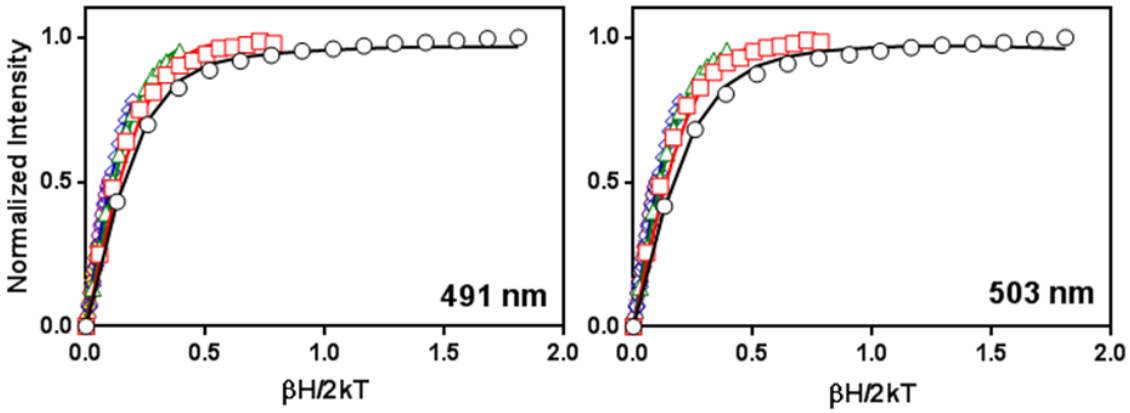

Figure 6.5: Examples of VTVH MCD data with corresponding fits for the transitions observed at 491 and 503 nm in MIM-1. Points coloured red, green, blue, yellow, grey, black represent data collected at 1.4, 3.0, 6.0, 12.0, 24.0 and 48.0 K, respectively.

The MCD spectra for the MIM proteins and LRA-8 required five and four Gaussians to resolve the spectra between 400-600 nm, respectively (Figure 6.4; Table 6.3).

Calculations using AOM were used to assign these transitions, and VTVH MCD data associated with these transitions were extracted and analysed using the dimer model as described elsewhere [270]. Relevant fitting parameters are summarised in Table 6.4.

Table 6.3: Summary of ligand field calculations

	Origin in O_h	*d-d* transition (nm)	
		Observed	Calculated
MIM-1			
	$^4T_{1g} \rightarrow {}^2T_{1g}(G)$	463	469
	$^4T_{1g} \rightarrow {}^4T_{1g}(P)$	490	487
	$^4T_{1g} \rightarrow {}^4T_{1g}(P)$	507	503
	$^4T_{1g} \rightarrow {}^4T_{1g}(P)$	520	512
	$^4T_{1g} \rightarrow {}^4A_{2g}$	565	559
MIM-2			
	$^4T_{1g} \rightarrow {}^2T_{1g}(G)$	470	465
	$^4T_{1g} \rightarrow {}^4T_{1g}(P)$	490	490
	$^4T_{1g} \rightarrow {}^4T_{1g}(P)$	505	506
	$^4T_{1g} \rightarrow {}^4T_{1g}(P)$	517	518
	$^4T_{1g} \rightarrow {}^4A_{2g}$	567	566
LRA-8			
	$^4T_{1g} \rightarrow {}^2T_{1g}(G)$	464	460
	$^4T_{1g} \rightarrow {}^4T_{1g}(P)$	491	495
	$^4T_{1g} \rightarrow {}^4T_{1g}(P)$	502	503
	$^4T_{1g} \rightarrow {}^4T_{1g}(P)$	509	517

Table 6.4: Spectroscopic parameters obtained from fitting VTVH MCD data using the dimer model.

	MIM-1			MIM-2			LRA-8		
Parameter	463 nm	490 nm	507 nm	470 nm	490 nm	505 nm	464 nm	491 nm	509 nm
J (cm^{-1})	0.29	0.27	0.26	0.31	0.27	0.27	0.29	0.31	0.27
D_α (6-coordinate) (cm^{-1})	≥ 50	≥ 50	≥ 50	≥ 50	≥ 50	≥ 50	≥ 50	≥ 50	≥ 50
D_β (6-coordinate) (cm^{-1})	-	-	-	-	-	-	-	-	-
E (α,β metal) (cm^{-1})	0.0	0.0	0.0	0.0	0.0	0.0	0.0	0.0	0.0

The major transitions in MIM-1, MIM-2 and LRA-8 are 490/520 nm, 490/517 nm and 491/509 nm, respectively, and arise from spin-allowed $^4T_{1g}$(P) transitions associated with a six-coordinate Co^{2+} ions in the active site. Importantly, fitting the VTVH MCD data of the major resolved transitions in all three protein samples indicates that in each case two six-coordinate Co^{2+} ions are weakly

ferromagnetically exchange-coupled (J ~ 0.2 cm^{-1}). Insofar, MIM-1, MIM-2 and LRA-8 have an active site electronic structure that is very similar to that of the B3-type MBL AIM-1 [269].

6.5 Conclusion

In the present study spectroscopic properties of the metalloenzymes CpsB, MIM-1, MIM-2 and LRA-8 with a view to (i) gaining insights into their metal ion centres and (ii) comparing these properties with other members of the large family of BMHs were investigated using MCD.

Collectively, while the present study establishes a similar dimetallic metal ion centre in CpsB, LRA-8, MIM-1 and MIM-2, it also highlights some of the disparity in metal binding that may exist between crystallographic (solid state) studies and 'in solution' investigations. According to available crystal structures for CpsB, the active site of this enzyme was proposed to be a trinuclear Mn^{2+} centre, whereby two of the closely spaced metal ions activate a water molecule for a nucleophilic attack on the phosphate moiety of a substrate. The third metal ion was proposed to be involved in substrate binding.[52] However, MCD data have demonstrated that active CpsB contains only a dimetallic metal centre in solution. This is supported by recently published atomic absorption measurements of Mn^{2+} or Co^{2+}-reconstituted CpsB and ITC data, which also indicate the presence of only two bound metal ions in the active enzyme[266]. The metal ion affinities, determined by ITC, are similar to those of the well-characterised antibiotic-degrading MBL AIM-1 [72] (see also Chapter 5) and cyclic nucleotide diesterases,[257] but significantly weaker than those recorded for phosphotriesterases.[232] To date the *in vivo* metal ion composition of CpsB remains obscure, but Mn^{2+} appears to be the most likely candidate, based on optimal catalytic performance combined with bioavailability.

Recent crystallographic investigations of MIM-1 and MIM-2 (presented in chapter 4) indicate that the native Zn^{2+}-bound enzymes contain a five- and a six-coordinate metal ion in the active site, linked via a μ-OH which is believed to be the nucleophile for hydrolysis. In contrast, MCD data of the Co^{2+}-substituted derivatives suggest the presence of two six-coordinate metal centres, an observation also seen for the homologous AIM-1 (Chapter 5). It is reasonable to attribute the additional ligand to the presence of an additional, terminally coordinated water molecule. The observed variation in coordination number may be a reflection of different coordination chemical properties of zinc and cobalt ions, or it may be caused as a consequence of a crystallographic artefact. However, considering the fact that the catalytic properties of the Co^{2+}-derivatives of MIM-1, MIM-2, LRA-8 and AIM-1

are similar to those of their Zn^{2+}-containing counterparts it is likely that the variation in the coordination number has little effect on the function of these enzymes.

For LRA-8 no crystallographic data are available for comparison. Hence, the spectroscopic data presented here provide a first insight into the active site of this enzyme, and they demonstrate that LRA-8 is likely to have an active site structure and catalytic mechanism characteristic for MBLs.

Thus, while spectroscopic studies demonstrate that several BMHs that may differ in function, at the molecular level they operate in a rather conserved manner. However, it needs to be remembered that in order to carry out this comparison Co^{2+} derivatives of each of these enzymes were generated. Since cobalt is not the native metal ion in any of these enzymes the question remains how metal ion selectivity may affect the function of these enzymes. We know already that MIM-1 and MIM-2 operate optimally as MBLs when Zn^{2+} is bound, but Ca^{2+} promotes their lactonase activity.[26] Furthermore, different metal ions may affect the immediate geometry of the coordination environment in different ways as evidenced by the significant variations in entropy observed when different metal ions bind to a particular active site[268,279]. Thus, while my studies demonstrate that under identical conditions diverse enzyme from the BMH superfamily may operate in a conserved manner, the question as to how metal ion selectivity (and thus function) may be modulated remains to be solved.

Chapter 7
Conclusions and direction for further work

This thesis has examined the kinetic, structural, spectroscopic and mechanistic features of several BMHs that share similarities in their active site geometry, yet differ in their associated primary functions.

In Chapter 2 the reaction trajectory, including the transition state, of the PAP-catalysed reaction were investigated. Specifically, the averaged geometry of two alternate conformations for bound phosphate, a product and substrate mimic, represented a good model for the structure of the transition state. The high-resolution crystal structure of this complex also highlighted a hydrogen bond between the metal ion bridging μ-OH and an oxygen atom of the bound phosphate group. This observation indicates that at least in this complex the μ-OH does not act as the reaction-initiating nucleophile but instead assist the binding and orientation of the substrate and transition state during the catalytic cycle. Given the similarity in the active site between this enzyme and numerous other BMHs, it is likely that a similar transition state may be present in all these enzymes. Hence, the structural insight gained here may be exploited in the design of transition state mimics as leads of future chemotherapeutics, targeted against various ailments associated with BMHs.

Chapter 3 provided insights into the high resolution (1.3 Å) structure for fluoride-inhibited OpdA, and discussed the significance of an extensive hydrogen bonding network for the mechanism employed by this enzyme. Specifically, the structure shows two alternative conformations of several residues in the substrate binding pocket when the fluoride-bound and free form of OpdA were compared. Interestingly, although the structural changes imposed on the first coordination sphere by fluoride binding to the two metal ions is small, their effect on the outer sphere is significant. In contrast, in the homologous enzyme OPH, which has a first coordination sphere identical to that of OpdA, fluoride does not act as an inhibitor, most likely because in this enzyme no extensive hydrogen bonding network is present that connects the metal ion binding site with the substrate binding pocket. It is currently unclear how minimal structural changes in the first coordination sphere are capable of imposing a significant effect on catalysis in OpdA. Computational studies combining density functional approaches with molecular dynamics calculations may provide essential insight into this fine-tuning mechanism.

In Chapter 4 the crystal structures of two novel, non-pathogenic MBL-like proteins from marine environments are described (*i.e.* MIM-1 and MIM-2). Although functionally different from the phosphatases described in the preceding Chapters, these enzymes share structrual simialrities that include the presence of a binuclear active site, whose metal ions are bridged by a water/OH molecule (the expected nucleophile for hydrolysis). While produced in an environment remote from direct human influence, MIM-1 and MIM-2 were shown to be structurally very similar to membes of the B3 subgroup of MBLs. Being non-pathogenic in origin yet sharing structural and mechanistic features with pathogenic MBLs, the MIM proteins are particularly interesting for continued efforts toward inhibitor developments. The fact that these enzymes have also displayed functional promiscuity in the form of lactonase activity, suggests that further structural investigations of substrate binding may lead to a greater understanding of the origins and evolution of MBL activity.

In Chapter 5 a comprehensive kinetic and spectroscopic investigation of the pathogenic B3 subgroup MBL AIM-1 from *Pseudomonas aeruginosa* was presented. This enzyme is of particular clinical importance and our research has provided information on this enzyme's mechanistic flexibility. Specifically, AIM-1 was shown to be capable of employing two alternative mechanistic strategies, likely to be due to a certain degree of freedom in binding the substrate. This observation may be useful in the design of potent inhibitors as binding flexibility may be taken into account to generate a group of compounds that bind reliably and persistently.

Towards this aim, our group has commenced in synthesising a group of inhibitors as leads towards future drug design. Specifically, I tested several compounds produced by A/Prof. Ross McGeary's group for their *in vitro* inhibitory effect on AIM-1 (Figure 7.1 and Table 7.1; see also paper recently published by EJMECH; https://doi.org/10.1016/j.ejmech.2017.05.061). The inhibitors were quite efficient with K_i values in the low μM range. The dominating mode of inhibition is competitive, although several compounds have a considerable contribution from an uncompetitive binding mode. This observation is in agreement with the mechanistic flexibility observed for AIM-1.

Table 7.1: Inhibition data for selected inhibitors of AIM-1

Inhibitor	AIM-1	
	K_{ic} (μM)	K_{iuc} (μM)
68	9.3± 2.2	30.19 ± 9.89
70	10.85 ± 2.71	47.31 ± 13
72	2.24 ± 0.33	12.48 ± 2.16
39	2.27 ± 0.34	12.31 ± 2.11
67	3.04 ± 0.86	9.79 ± 2.44
30	3.04 ± 0.86	9.79 ± 2.44

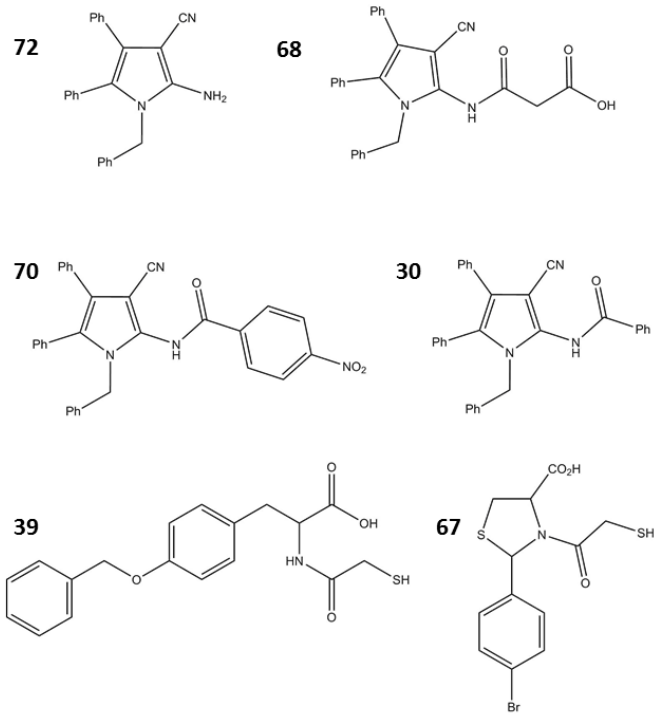

Figure 7.1: Structures of inhibitors tested on AIM-1

Current efforts in the group focus thus on obtaining crystal structures of AIM-1 in complex with some of these inhibitors. Some preliminary crystals are shown in Figures 7.2 and 7.3 although to date, no reasonable diffraction data have been obtained.

Figure 7.2: Selected crystals for AIM-1 co-crystallised with the inhibitor captopril. Associated crystallisation screens and well conditions include: peg rx-G6 (left), peg ion-H8 (centre), peg ion-A5 (right).

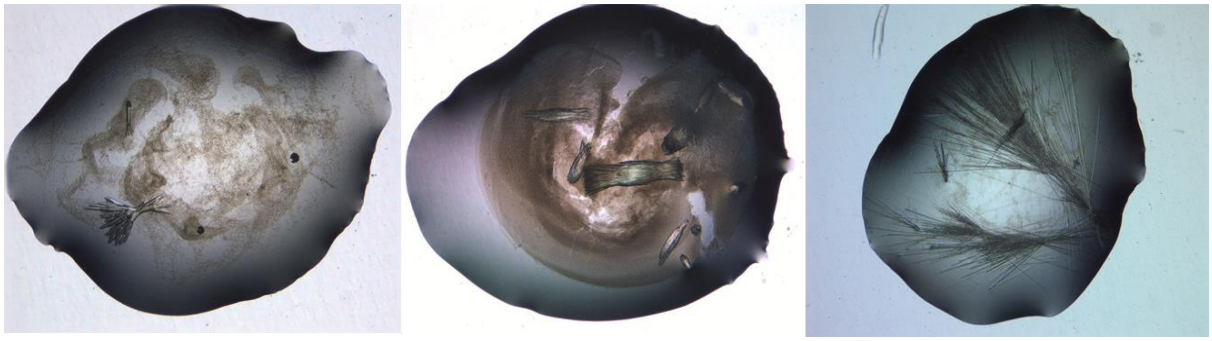

Figure 7.3: Selected crystals for AIM-1 co-crystallised with inhibitor 70. Associated crystallisation screens and well conditions include: peg ion-D5 (left), peg ion-H8 (centre), peg ion-H4 (right).

In Chapter 6 'in solution' metal ion coordination investigations of several BMHs were discussed. The method of choice was MCD, largely because it provides a simple approach towards gaining insight into the active site structure of Co^{2+} derivatives ofthese enzymes. Apart from providing functional insight such studies may also demonstrate how ligand binding (*i.e.* inhibitors or substrates) affects the active site structure, thus providing guidance in the development or improvement of antagonists that may inform the development of potent future drug leads. My investigations demonstrated, however, that the non-clinical inhibitor D-captopril does not appear to perturb the electronic structure of the di-Co^{2+} centre, suggesting that it may not bind directly to the metal ions. This is in contrast to available crystal structures of MBLs with bound D-captopril, which demonstrate that the inhibitor binds to both metal ions via its thiol group. This potential differences in lignad binding may point to a crystallographic artefact, and it is thus prudent to analyse inhibitor binding with a range of available

techniques. Similarly, my spectroscopic data demonstrated that CpsB, a promising target for novel antimicrobial agents, is indeed a BMH; the third metal ion observed in the active site of the crystallised enzyme is also likely to be a crystallographic artefact.

Studies like the ones on MIM-1 and MIM-2 (Chapters 4 and 6) or LRA-8 (Chapter 6) are interesting since they provide functional insight on novel enzymes that may be of relevance for the development of chemotherapeutics although their host organisms are not immediately pathogenic. I thus extended this approach to search for other MBL-like proteins and identified an MBL homolog in *Salmonella typhimurium* (*i.e.* SIM-1). I successfully expressed this enzyme in *E.coli* and purified it following the same procedure outlined for LRA-8 in Chapter 6. The purified enzyme was used in crystallisation trials and some crystals were obtained (Figure 7.4). No suitable diffraction data have yet been collected. I also collected preliminary MCD data for the Co^{2+}-substituted variant of SIM-1 (Figure 7.5). While data collection is not yet complete an initial analysis of the spectral data indicates that the active site contains two six-coordinate Co^{2+} ions similar to other MBLs (as discussed in Chapters 5 and 6). Future efforts will continue toward completing this investigation, defining SIM-1 as a novel target to combat antibiotic resistance in *S. typhimurium*.

Thus, to conclude, this thesis presented an in-depth analysis of the active site structure and mechanism of a range of related BMH, and the insight gained may be instrumental for future developments of inhibitors that can be introduced as lead treatments for a range of human ailments.

Figure 7.4: Selected crystals of the putative B3 subgroup MBL SIM-1.

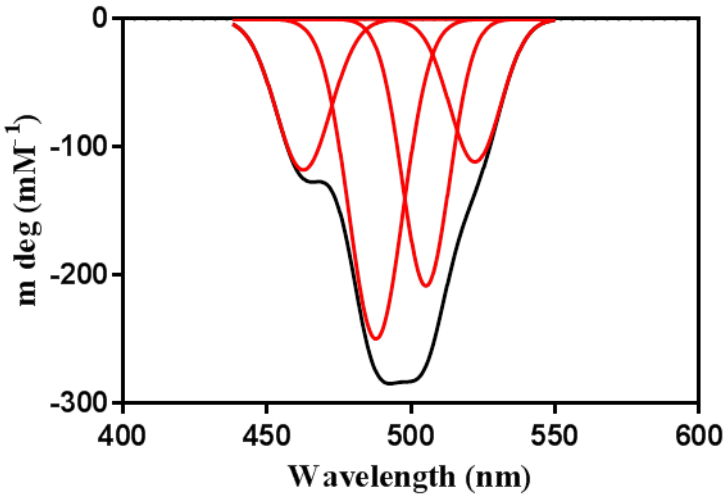

Figure 7.5: Gaussian-resolved MCD spectrum of SIM-1 at 7 T and 1.4 K.

References:

1. Mitić, N., Smith, S. J., Neves, A., Guddat, L. W., Gahan, L. R., and Schenk, G. (2006) The catalytic mechanisms of binuclear metallohydrolases. *Chemical reviews* **106**, 3338-3363
2. Schenk, G., Mitić, N., Gahan, L. R., and Ollis, D. L. (2012) Binuclear metallohydrolases: complex mechanistic strategies for a simple chemical reaction. *Accounts of chemical …*
3. Phelan, E. K., Miraula, M., Selleck , C., Ollis, D. L., Schenk, G., and Mitić, N. (2014) Metallo-β-lactamases: a major threat to human health. *American Journal of Molecular Biology*, *in press*
4. Schenk, G., Mitic, N., Hanson, G. R., and Comba, P. (2013) Purple acid phosphatase: A journey into the function and mechanism of a colorful enzyme. *Coordination Chemistry Reviews* **257**, 473-482
5. Schenk, G., Mateen, I., Ng, T.-K., Pedroso, M. M., Mitić, N., Jafelicci, M., Marques, R., Gahan, L. R., and Ollis, D. L. (2016) Organophosphate-degrading Metallohydrolases: Structure and Function of Potent Catalyst for Applications in Bioremediation. *Coordination Chemistry Reviews* **317**, 122-131
6. Jackson, C., Kim, H. K., Carr, P. D., Liu, J. W., and Ollis, D. L. (2005) The structure of an enzyme-product complex reveals the critical role of a terminal hydroxide nucleophile in the bacterial phosphotriesterase mechanism. *Biochim Biophys Acta* **1752**, 56-64
7. Leiros, H. K., Borra, P. S., Brandsdal, B. O., Edvardsen, K. S., Spencer, J., Walsh, T. R., and Samuelsen, O. (2012) Crystal structure of the mobile metallo-beta-lactamase AIM-1 from Pseudomonas aeruginosa: insights into antibiotic binding and the role of Gln157. *Antimicrob Agents Chemother* **56**, 4341-4353
8. Strater, N., Klabunde, T., Tucker, P., Witzel, H., and Krebs, B. (1995) Crystal structure of a purple acid phosphatase containing a dinuclear Fe(III)-Zn(II) active site. *Science* **268**, 1489-1492
9. Uppenberg, J., Lindqvist, F., Svensson, C., Ek-Rylander, B., and Andersson, G. (1999) Crystal structure of a mammalian purple acid phosphatase. *Journal of Molecular Biology* **290**, 201-211
10. McGeary, R. P., Schenk, G., and Guddat, L. W. (2014) The applications of binuclear metallohydrolases in medicine: recent advances in the design and development of novel drug leads for purple acid phosphatases, metallo-b-lactamases and arginases. *European journal of medicinal chemistry* **76**, 132-144
11. McGeary, R. P., Tan, D. T. C., and Schenk, G. (2017) Progress toward inhibitors of metallo-β-lactamases. *Future Medicinal Chemistry*
12. Schenk, G., Mateen, I., Ng, T. K., Pedroso, M. M., and Mitić, N. (2016) Organophosphate-degrading metallohydrolases: Structure and function of potent catalysts for applications in bioremediation. *Coordination Chemistry …*
13. Valdez, C. E., and Alexandrova, A. N. (2012) Why urease is a di-nickel enzyme whereas the CcrA -lactamase is a di-zinc enzyme. *The Journal of Physical Chemistry B* **116**, 10649-10656
14. Zambelli, B., Musiani, F., Benini, S., and Ciurli, S. (2011) Chemistry of Ni2+ in urease: sensing, trafficking, and catalysis. *Accounts of chemical research* **44**, 520-530
15. Mitic, N., Miraula, M., Selleck, C., Hadler, K. S., Uribe, E., Pedroso, M. M., and Schenk, G. . (2014) Catalytic mechanisms of metallohydrolases containing two metal ions. *Advances in protein chemistry and structural biology* **97**, 49-81

16. Karsisiotis, A. I., Damblon, C. F., and Roberts, G. C. (2014) A variety of roles for versatile zinc in metallo-β-lactamases. *Metallomics : integrated biometal science* **6**, 1181-1197
17. Pettinati, I., Brem, J., Lee, S. Y., and McHugh, P. J. (2016) The chemical biology of human metallo-β-lactamase fold proteins. *Trends in biochemical …*
18. McCall, K. A., Huang, C., and Fierke, C. A. (2000) Function and mechanism of zinc metalloenzymes. *The Journal of nutrition*
19. Wang, Z., Fast, W., Valentine, A. M., and Benkovic, S. J. (1999) Metallo-β-lactamase: structure and mechanism. *Current Opinion in Chemical Biology* **3**, 614-622
20. Mitic, N., Hadler, K. S., Gahan, L. R., Hengge, A. C., and Schenk, G. (2010) The divalent metal ion in the active site of uteroferrin modulates substrate binding and catalysis. *Journal of the American Chemical Society* **132**, 7049-7054
21. Cox, R. S., Schenk, G., Mitic, N., Gahan, L. R., and Hengge, A. C. (2007) Diesterase activity and substrate binding in purple acid phosphatases. *Journal of the American Chemical Society* **129**, 9550-9551
22. Ely, F., Hadler, K. S., Gahan, L. R., Guddat, L. W., Ollis, D. L., and Schenk, G. (2010) The organophosphate-degrading enzyme from Agrobacterium radiobacter displays mechanistic flexibility for catalysis. *The Biochemical Journal* **432**, 565-573
23. Hadler, K. S., Tanifum, E. A., Yip, S. H., Mitic, N., Guddat, L. W., Jackson, C. J., Gahan, L. R., Nguyen, K., Carr, P. D., Ollis, D. L., Hengge, A. C., Larrabee, J. A., and Schenk, G. (2008) Substrate-promoted formation of a catalytically competent binuclear center and regulation of reactivity in a glycerophosphodiesterase from *Enterobacter aerogenes*. *Journal of the American Chemical Society* **130**, 14129-14138
24. Baier, F., Chen, J., Solomonson, M., Strynadka, N., and Tokuriki, N. (2015) Distinct Metal Isoforms Underlie Promiscuous Activity Profiles of Metalloenzymes. *ACS Chemical Biology* **10**, 1684-1693
25. Miraula, M., Brunton, C. S., Schenk, G., and Mitić, N. (2013) Identification and preliminary characterization of novel B3-type metallo-β-lactamases. *Identification and preliminary characterization of novel B3-type metallo-β-lactamases*
26. Miraula, M., Whitaker, J. J., Schenk, G., and Mitic, N. (2015) beta-Lactam antibiotic-degrading enzymes from non-pathogenic marine organisms: a potential threat to human health. *J Biol Inorg Chem* **20**, 639-651
27. Bononi, A., Agnoletto, C., Marchi, D. E., and Marchi, S. (2011) Protein kinases and phosphatases in the control of cell fate. *Enzyme …*
28. Bowls, B. J., Freeman, J. M., and Luna, J. A. (2003) Oral treatment of organophosphate poisoning in mice. *… emergency medicine*
29. Kovacic, P. (2003) Mechanism of organophosphates (nerve gases and pesticides) and antidotes: electron transfer and oxidative stress. *Current medicinal chemistry*
30. Pimentel, D., and Levitan, L. (1986) Pesticides: amounts applied and amounts reaching pests. *Bioscience*
31. Kazemi, M., , A. M. T., , R. V., , A. A. N., and Soni, a. A. (2012) Organophosphate pesticides: A general review. *Agricultural Science Research Journals* **Vol. 2(9**, 512-522
32. Murray, D., Piola, J. C., Senanayake, N., Sheriff, R., and Singh, S. (2002) Pesticide poisoning in the developing world—a minimum pesticides list. *The Lancet*
33. Lotti, M. (2002) Promotion of organophosphate induced delayed polyneuropathy by certain esterase inhibitors. *Toxicology*
34. Council, U. N.-H. R. (2017) Human Rights Council, Thirty-fourth session - Agenda item 3Report of the Special Rapporteur on the right to food 2017 - 27 February-24 March 2017.

35. Hoskin, F. C. G., Walker, J. E., and Dettbarn, W. D. (1995) Hydrolysis of tetriso by an enzyme derived from Pseudomonas diminuta as a model for the detoxication of O-ethyl S-(2-diisopropylaminoethyl) …. *Biochemical pharmacology*
36. Lai, K., Stolowich, N. J., and Wild, J. R. (1995) Characterization of PS bond hydrolysis in organophosphorothioate pesticides by organophosphorus hydrolase. *Archives of biochemistry and biophysics*
37. Schofield, D. A., Westwater, C., and Barth, J. L. (2007) Development of a yeast biosensor–biocatalyst for the detection and biodegradation of the organophosphate paraoxon. *Applied microbiology and …*
38. Schofield, D. A., and DiNovo, A. A. (2010) Generation of a mutagenized organophosphorus hydrolase for the biodegradation of the organophosphate pesticides malathion and demeton-S. *Journal of applied microbiology*
39. Mulchandani, A., and Kaneva, I. (1999) Detoxification of organophosphate nerve agents by immobilized Escherichia coli with surface-expressed organophosphorus hydrolase. *Biotechnology and …*
40. Raushel, F. M. (2002) Bacterial detoxification of organophosphate nerve agents. *Current Opinion in Microbiology* **5**, 288-295
41. Hoskin, F. C. G., Walker, J. E., and Stote, R. (1999) Degradation of nerve gases by CLECS and cells: kinetics of heterogenous systems. *Chemico-biological interactions*
42. Schenk, G., Gahan, L. R., Carrington, L. E., Mitic, N., Valizadeh, M., Hamilton, S. E., de Jersey, J., and Guddat, L. W. (2005) Phosphate forms an unusual tripodal complex with the Fe-Mn center of sweet potato purple acid phosphatase. *Proceedings of the National Academy of Sciences of the United States of America* **102**, 273-278
43. Beck, J. L., Keough, D. T., De Jersey, J., and Zerner, B. (1984) Enzymatically active zinc, copper and mercury derivatives of the one-iron form of pig allantoic fluid acid phosphatase. *Biochim Biophys Acta* **791**, 357-363
44. Schenk, G., Carrington, L. E., Hamilton, S. E., de Jersey, J., and Guddat, L. W. (1999) Crystallization and preliminary X-ray diffraction data for a purple acid phosphatase from sweet potato. *Acta Crystallogr D Biol Crystallogr* **55**, 2051-2052
45. Hadler, K. S., Huber, T., Cassady, A. I., Weber, J., Robinson, J., Burrows, A., Kelly, G., Guddat, L. W., Hume, D. A., Schenk, G., and Flanagan, J. U. (2008) Identification of a non-purple tartrate-resistant acid phosphatase: an evolutionary link to Ser/Thr protein phosphatases? *BMC research notes* **1**, 78
46. Lindqvist, Y., Johansson, E., Kaija, H., Vihko, P., and Schneider, G. (1999) Three-dimensional structure of a mammalian purple acid phosphatase at 2.2 angstrom resolution with a m-(hydr)oxo bridged di-iron center. *Journal of Molecular Biology* **291**, 135-147
47. Schenk, G., Ge, Y., Carrington, L. E., Wynne, C. J., Searle, I. R., Carroll, B. J., Hamilton, S., and de Jersey, J. (1999) Binuclear Metal Centers in Plant Purple Acid Phosphatases: Fe-Mn in Sweet Potato and Fe-Zn in Soybean. *Archives of Biochemistry and Biophysics* **370**, 183-183
48. Kim, H. S., Lee, S. J., Yoon, H. J., An, D. R., Kim do, J., Kim, S. J., and Suh, S. W. (2011) Crystal structures of YwqE from Bacillus subtilis and CpsB from Streptococcus pneumoniae, unique metal-dependent tyrosine phosphatases. *J Struct Biol* **175**, 442-450
49. Geno, A. K., Hauser, J. R., Gupta, K., and Yother, J. (2014) Streptococcus pneumoniae phosphotyrosine phosphatase CpsB and alterations in capsule production resulting from changes in oxygen availability. *Journal of bacteriology* **196**, 1992-2003

50. Ghanem, E., Li, Y., Xu, C., and Raushel, F. M. (2007) Characterization of a phosphodiesterase capable of hydrolyzing EA 2192, the most toxic degradation product of the nerve agent VX. *Biochemistry* **46**, 9032-9040
51. Daumann, L. J., McCarthy, B. Y., Hadler, K. S., Murray, T. P., Gahan, L. R., Larrabee, J. A., Ollis, D. L., and Schenk, G. (2013) Promiscuity comes at a price: catalytic versatility vs efficiency in different metal ion derivatives of the potential bioremediator GpdQ. *Biochimica et biophysica acta* **1834**, 425-432
52. Hagelueken, G., Huang, H., Mainprize, I. L., Whitfield, C., and Naismith, J. H. (2009) Crystal structures of Wzb of Escherichia coli and CpsB of Streptococcus pneumoniae, representatives of two families of tyrosine phosphatases that regulate capsule assembly. *Journal of molecular biology* **392**, 678-688
53. Times, N. Y. (1945) Fleming A. Penicillin's finder assays its future. in *New York Times*, USA
54. Van Boeckel, T. P., Brower, C., Gilbert, M., Grenfell, B. T., Levin, S. A., Robinson, T. P., Teillant, A., and Laxminarayan, R. (2015) Global trends in antimicrobial use in food animals. *Proc Natl Acad Sci U S A* **112**, 5649-5654
55. Hu, Y., Yang, X., Li, J., Lv, N., Liu, F., and Wu, J. (2016) The transfer network of bacterial mobile resistome connecting animal and human microbiome. *Applied and …*
56. Hasman, H., Hammerum, A. M., Hansen, F., Hendriksen, R. S., Olesen, B., Agersø, Y., Zankari, E., Leekitcharoenphon, P., Stegger, M., Kaas, R. S., Cavaco, L. M., Hansen, D. S., Aarestrup, F. M., and Skov, R. L. (2015) Detection ofmcr-1encoding plasmid-mediated colistin-resistantEscherichia coliisolates from human bloodstream infection and imported chicken meat, Denmark 2015. *Eurosurveillance* **20**
57. Falgenhauer, L., Waezsada, S. E., and Yao, Y. (2016) Colistin resistance gene mcr-1 in extended-spectrum β-lactamase-producing and carbapenemase-producing Gram-negative bacteria in Germany. *The Lancet infectious …*
58. Walsh, T. R., Weeks, J., and Livermore, D. M. (2011) Dissemination of NDM-1 positive bacteria in the New Delhi environment and its implications for human health: an environmental point prevalence study. *The Lancet infectious …*
59. Poirel, L., Lagrutta, E., Taylor, P., and Pham, J. (2010) Emergence of metallo-β-lactamase NDM-1-producing multidrug-resistant Escherichia coli in Australia. *Antimicrobial agents …*
60. Livermore, D. M., and Woodford, N. (2006) The beta-lactamase threat in Enterobacteriaceae, Pseudomonas and Acinetobacter. *Trends in microbiology* **14**, 413-420
61. Livermore, D. M., Warner, M., and Mushtaq, S. (2011) What remains against carbapenem-resistant Enterobacteriaceae? Evaluation of chloramphenicol, ciprofloxacin, colistin, fosfomycin, minocycline, nitrofurantoin, …. *International journal of …*
62. Gazin, M., Paasch, F., and Goossens, H. (2012) Current trends in culture-based and molecular detection of extended-spectrum-β-lactamase-harboring and carbapenem-resistant Enterobacteriaceae. *Journal of clinical …*
63. Yong, D., Toleman, M. A., Bell, J., Ritchie, B., Pratt, R., Ryley, H., and Walsh, T. R. (2012) Genetic and biochemical characterization of an acquired subgroup B3 metallo-beta-lactamase gene, blaAIM-1, and its unique genetic context in Pseudomonas aeruginosa from Australia. *Antimicrob Agents Chemother* **56**, 6154-6159
64. Garau, G., García-Sáez, I., Bebrone, C., Anne, C., Mercuri, P., Galleni, M., Frère, J.-M., and Dideberg, O. (2004) Update of the standard numbering scheme for class B β-lactamases. *Antimicrobial Agents and Chemotherapy* **48**, 2347-2349

65. Bebrone, C. (2007) Metallo-β-lactamases (classification, activity, genetic organization, structure, zinc coordination) and their superfamily. *Biochemical Pharmacology* **74**, 1686-1701
66. Mitic, N., Miraula, M., Selleck, C., Hadler, K. S., Uribe, E., Pedroso, M. M., and Schenk, G. (2014) Catalytic mechanisms of metallohydrolases containing two metal ions. *Advances in protein chemistry and structural biology* **97**, 49-81
67. Heinz, U., and Adolph, H. W. (2004) Metallo-b-lactamases: two binding sites for one catalytic metal ion? *Cellular and molecular life sciences : CMLS* **61**, 2827-2839
68. Badarau, A., and Page, M. I. (2008) Loss of enzyme activity during turnover of the Bacillus cereus β-lactamase catalysed hydrolysis of β-lactams due to loss of zinc ion. *JBIC Journal of Biological Inorganic Chemistry* **13**, 919-928
69. Mollard, C., Moali, C., Papamicael, C., Damblon, C., Vessilier, S., Amicosante, G., Schofield, C. J., Galleni, M., Frere, J. M., and Roberts, G. C. (2001) Thiomandelic acid, a broad spectrum inhibitor of zinc beta-lactamases: kinetic and spectroscopic studies. *J Biol Chem* **276**, 45015-45023
70. Wachino, J., Yamaguchi, Y., Mori, S., Kurosaki, H., Arakawa, Y., and Shibayama, K. (2013) Structural insights into the subclass B3 metallo-beta-lactamase SMB-1 and the mode of inhibition by the common metallo-beta-lactamase inhibitor mercaptoacetate. *Antimicrob Agents Chemother* **57**, 101-109
71. Wachino, J., Yamaguchi, Y., Mori, S., Jin, W., Kimura, K., Kurosaki, H., and Arakawa, Y. (2016) Structural Insights into Recognition of Hydrolyzed Carbapenems and Inhibitors by Subclass B3 Metallo-beta-Lactamase SMB-1. *Antimicrob Agents Chemother* **60**, 4274-4282
72. Selleck, C., Larrabee, J. A., Harmer, J., Guddat, L. W., Mitić, N., Helweh, W., Ollis, D. L., Craig, W. R., Tierney, D. L., Monteiro Pedroso, M., and Schenk, G. (2016) AIM-1: An Antibiotic-Degrading Metallohydrolase That Displays Mechanistic Flexibility. *Chemistry (Weinheim an der Bergstrasse, Germany)* **22**, 17704-17714
73. Brem, J., van Berkel, S. S., Zollman, D., and Lee, S. Y. (2016) Structural basis of metallo-β-lactamase inhibition by captopril stereoisomers. *Antimicrobial agents …*
74. Toney, J. H., Hammond, G. G., Fitzgerald, P. M., Sharma, N., Balkovec, J. M., Rouen, G. P., Olson, S. H., Hammond, M. L., Greenlee, M. L., and Gao, Y. D. (2001) Succinic acids as potent inhibitors of plasmid-borne IMP-1 metallo-beta-lactamase. *J Biol Chem* **276**, 31913-31918
75. Toney, J. H., Fitzgerald, P. M., Grover-Sharma, N., Olson, S. H., May, W. J., Sundelof, J. G., Vanderwall, D. E., Cleary, K. A., Grant, S. K., Wu, J. K., Kozarich, J. W., Pompliano, D. L., and Hammond, G. G. (1998) Antibiotic sensitization using biphenyl tetrazoles as potent inhibitors of Bacteroides fragilis metallo-beta-lactamase. *Chem Biol* **5**, 185-196
76. Nauton, L., Kahn, R., Garau, G., Hernandez, J.-F., and Dideberg, O. (2008) Structural insights into the design of inhibitors for the L1 metallo- -lactamase from Stenotrophomonas maltophilia. *Journal of molecular biology* **375**, 257-269
77. Smith, W. H. T., and Ball, S. G. (2000) ACE inhibitors in heart failure: an update. *Basic Research in Cardiology* **95**
78. Buttar, H. S. (1997) An overview of the influence of ACE inhibitors on fetal-placental circulation and perinatal development. *Molecular and cellular biochemistry*
79. Sabath, L. D., and Abraham, E. P. (1966) Zinc as a cofactor for cephalosporinase from Bacillus cereus 569. *Biochem J* **98**, 11C-13C
80. Bandoh, K., Watanabe, K., Muto, Y., Tanaka, Y., Kato, N., and Ueno, K. (1992) Conjugal transfer of imipenem resistance in Bacteroides fragilis. *J Antibiot (Tokyo)* **45**, 542-547

81. Cornaglia, G., Giamarellou, H., and Rossolini, G. M. (2011) Metallo-beta-lactamases: a last frontier for beta-lactams? *Lancet Infect Dis* **11**, 381-393
82. Prevention, U. D. o. H. a. H. S.-C. f. D. C. a. (2013) Antibiotic Resistance Threats in the United Stated 2013. Centres for Disease Control and Prevention, Unites States
83. Papp-Wallace, K. M., Endimiani, A., Taracila, M. A., and Bonomo, R. A. (2011) Carbapenems: past, present, and future. *Antimicrob Agents Chemother* **55**, 4943-4960
84. Cofre, J., Montes, P., Vallejos, A., Benitez, J., Garcia, D., Martinez-Oyanedel, J., Carvajal, N., and Uribe, E. (2014) Further insight into the inhibitory action of a LIM/double zinc-finger motif of an agmatinase-like protein. *Journal of inorganic biochemistry* **132**, 92-95
85. Llarrull, L. I., Tioni, M. F., and Vila, A. J. (2008) Metal Content and Localization during Turnover inB. cereusMetallo-β-lactamase. *Journal of the American Chemical Society* **130**, 15842-15851
86. Rasia, R. M., and Vila, A. J. (2002) Exploring the role and the binding affinity of a second zinc equivalent in B. cereus metallo-beta-lactamase. *Biochemistry* **41**, 1853-1860
87. Laraki, N., Franceschini, N., and Rossolini, G. M. (1999) Biochemical Characterization of the Pseudomonas aeruginosa 101/1477 Metallo-β-Lactamase IMP-1 Produced byEscherichia coli. *Antimicrobial agents …*
88. Iyobe, S., Kusadokoro, H., Ozaki, J., Matsumura, N., Minami, S., Haruta, S., Sawai, T., and O'Hara, K. (2000) Amino Acid Substitutions in a Variant of IMP-1 Metallo-beta -Lactamase. *Antimicrobial Agents and Chemotherapy* **44**, 2023-2027
89. Yamaguchi, Y., Ding, S., Murakami, E., and Imamura, K. (2011) A Demetallation Method for IMP-1 Metallo-β-Lactamase with Restored Enzymatic Activity Upon Addition of Metal Ion (s). *…*
90. Cornaglia, G., Mazzariol, A., and Lauretti, L. (2000) Hospital outbreak of carbapenem-resistant Pseudomonas aeruginosa producing VIM-1, a novel transferable metallo-β-lactamase. *Clinical infectious …*
91. Tsakris, A., Pournaras, S., and Woodford, N. (2000) Outbreak of infections caused by Pseudomonas aeruginosa producing VIM-1 carbapenemase in Greece. *Journal of clinical …*
92. Papafraggas, E., and Malamou-Lada, H. (2003) VIM-1 metallo-β-lactamase-producing Klebsiella pneumoniae strains in Greek hospitals. *Journal of Clinical …*
93. Pournaras, S., Maniati, M., and Petinaki, E. (2003) Hospital outbreak of multiple clones of Pseudomonas aeruginosa carrying the unrelated metallo-β-lactamase gene variants blaVIM-2 and blaVIM-4. *Journal of …*
94. Miriagou, V., Tzelepi, E., and Gianneli, D. (2003) Escherichia coli with a self-transferable, multiresistant plasmid coding for metallo-β-lactamase VIM-1. *Antimicrobial agents …*
95. Docquier, J.-D., Lamotte-Brasseur, J., Galleni, M., Amicosante, G., Frère, J.-M., and Rossolini, G. M. (2003) On functional and structural heterogeneity of VIM-type metallo-beta-lactamases. *The Journal of antimicrobial chemotherapy* **51**, 257-266
96. Yong, D., Toleman, M. A., Giske, C. G., and Cho, H. S. (2009) Characterization of a new metallo-β-lactamase gene, blaNDM-1, and a novel erythromycin esterase gene carried on a unique genetic structure in Klebsiella …. *Antimicrobial agents …*
97. Jr, M. R. C. (2010) NDM-1—a cause for worldwide concern. *New England Journal of Medicine*
98. Yang, H., Aitha, M., Hetrick, A. M., Richmond, T. K., Tierney, D. L., and Crowder, M. W. (2012) Mechanistic and spectroscopic studies of metallo-beta-lactamase NDM-1. *Biochemistry* **51**, 3839-3847

99. Yang, H., Aitha, M., Hetrick, A. M., Richmond, T. K., Tierney, D. L., and Crowder, M. W. (2012) Mechanistic and spectroscopic studies of metallo-β-lactamase NDM-1. *Biochemistry* **51**, 3839-3847
100. Gottig, S., Hamprecht, A. G., Christ, S., Kempf, V. A., and Wichelhaus, T. A. (2013) Detection of NDM-7 in Germany, a new variant of the New Delhi metallo-beta-lactamase with increased carbapenemase activity. *J Antimicrob Chemother* **68**, 1737-1740
101. Yang, H., Aitha, M., Marts, A. R., Hetrick, A., Bennett, B., Crowder, M. W., and Tierney, D. L. (2014) Spectroscopic and mechanistic studies of heterodimetallic forms of metallo-beta-lactamase NDM-1. *J Am Chem Soc* **136**, 7273-7285
102. Yang, H., Aitha, M., Marts, A. R., Hetrick, A., Bennett, B., Crowder, M. W., and Tierney, D. L. (2014) Spectroscopic and mechanistic studies of heterodimetallic forms of metallo-β-lactamase NDM-1. *Journal of the American Chemical Society* **136**, 7273-7285
103. de Seny, D., Heinz, U., Wommer, S., Kiefer, M., Meyer-Klaucke, W., Galleni, M., Frere, J. M., Bauer, R., and Adolph, H. W. (2001) Metal ion binding and coordination geometry for wild type and mutants of metallo-b-lactamase from *Bacillus cereus* 569/H/9 (BcII): a combined thermodynamic, kinetic, and spectroscopic approach. *The Journal of Biological Chemistry* **276**, 45065-45078
104. Llarrull, L. I., Tioni, M. F., Kowalski, J., Bennett, B., and Vila, A. J. (2007) Evidence for a dinuclear active site in the metallo-β-lactamase BcII with substoichiometric Co(II): A new model for metal uptake. *Journal of Biological Chemistry* **282**, 30586-30595
105. Abriata, L. A., Gonzalez, L. J., and Llarrull, L. I. (2008) Engineered Mononuclear Variants in *Bacillus cereus* Metallo-b-lactamase BcII are Inactive. *Biochemistry* **47**, 8590
106. Badarau, A., and Page, M. I. (2006) The variation of catalytic efficiency of *Bacillus cereus* metallo-b-lactamase with different active site metal ions. *Biochemistry* **45**, 10654-10666
107. Dal Peraro, M., Vila, A. J., and Carloni, P. (2004) Substrate binding to mononuclear metallo-b-lactamase from *Bacillus cereus*. *Proteins* **54**, 412-423
108. Green, V. L., Verma, A., and Owens, R. J. (2011) Structure of New Delhi metallo-β-lactamase 1 (NDM-1). *… Section F: Structural …*
109. Bebrone, C., Delbrück, H., Kupper, M. B., Schlömer, P., Willmann, C., Frère, J.-M., Fischer, R., Galleni, M., and Hoffmann, K. M. V. (2009) The structure of the dizinc subclass B2 metallo-b-lactamase CphA reveals that the second inhibitory zinc ion binds in the histidine site. *Antimicrobial Aagents and Chemotherapy* **53**, 4464-4471
110. Hernandez Valladares, M., Rossolini, G. M., Amicosante, G., Adolph, H.-W., Kiefer, M., Heinz, U., Paul Soto, R., Meyer-Klaucke, W., Nolting, H. F., Zeppezauer, M., Galleni, M., and Frère, J.-M. (2000) Kinetic and spectroscopic characterization of native and metal-substituted β-lactamase from Aeromonas hydrophila AE036. *FEBS letters* **467**, 221-225
111. Massidda, O., Rossolini, G. M., and Satta, G. (1991) The Aeromonas hydrophila cphA gene: molecular heterogeneity among class B metallo-beta-lactamases. *Journal of Bacteriology* **173**, 4611-4617
112. Garau, G., Bebrone, C., Anne, C., Galleni, M., Frère, J.-M., and Dideberg, O. (2005) A metallo-b-lactamase enzyme in action: crystal structures of the monozinc carbapenemase CphA and its complex with biapenem. *Journal of Molecular Biology* **345**, 785-795

113. Xu, D., Zhou, Y., Xie, D., and Guo, H. (2005) Antibiotic Binding to Monozinc CphA β-Lactamase from Aeromonas h ydropila: Quantum Mechanical/Molecular Mechanical and Density Functional Theory Studies. *Journal of medicinal chemistry*
114. Bebrone, C. (2005) Dramatic Broadening of the Substrate Profile of the Aeromonas hydrophila CphA Metallo- -lactamase by Site-directed Mutagenesis. *Journal of Biological Chemistry* **280**, 28195-28202
115. Bebrone, C., Frère, J.-M., Galleni, M., Anne, C., Kerff, F., Garau, G., De Vriendt, K., Lantin, R., Devreese, B., Van Beeumen, J., and Dideberg, O. (2008) Mutational analysis of the zinc- and substrate-binding sites in the CphA metallo-b-lactamase from *Aeromonas hydrophila*. *The Biochemical Journal* **414**, 151-159
116. Simona, F., Magistrato, A., Peraro, D. M., and Cavalli, A. (2009) Common Mechanistic Features among Metallo-β-lactamases A COMPUTATIONAL STUDY OF AEROMONAS HYDROPHILA CphA ENZYME. *Journal of biological …*
117. Wu, C. J., Chen, P. L., Wu, J. J., Yan, J. J., Lee, C. C., Lee, H. C., Lee, N. Y., Chang, C. M., Lin, Y. T., Chiu, Y. C., and Ko, W. C. (2012) Distribution and phenotypic and genotypic detection of a metallo-beta-lactamase, CphA, among bacteraemic Aeromonas isolates. *J Med Microbiol* **61**, 712-719
118. Maria José, S., Luísa, P., João Carlos, S., Isabel, H., Artur, A., and António, C. (2003) Sfh-I, a Subclass B2 Metallo-β-Lactamase from a *Serratia fonticola* Environmental Isolate. *Antimicrobial Agents and Chemotherapy* **47**, 2330-2333
119. Fonseca, F., Bromley, E. H. C., and Saavedra, M. J. (2011) Crystal structure of Serratia fonticola Sfh-I: activation of the nucleophile in mono-zinc metallo-β-lactamases. *Journal of molecular …*
120. Stuttgart, U. o. (2017) The Metallo Beta Lactamase Engineering Database.
121. Crowder, M. W., Walsh, T. R., Banovic, L., Pettit, M., and Spencer, J. (1998) Overexpression, purification, and characterization of the cloned metallo-β-lactamase L1 from *Stenotrophomonas maltophilia*. *Antimicrobial Agents and Chemotherapy* **42**, 921-926
122. Ullah, J. H., Walsh, T. R., Taylor, I. A., Emery, D. C., Verma, C. S., Gamblin, S. J., and Spencer, J. (1998) The crystal structure of the L1 metallo-beta-lactamase from *Stenotrophomonas maltophilia* at 1.7 A resolution. *Journal of Molecular Biology* **284**, 125-125
123. McManus-Munoz, S., and Crowder, M. W. (1999) Kinetic mechanism of metallo-beta-lactamase L1 from Stenotrophomonas maltophilia. *Biochemistry* **38**, 1547-1553
124. Spencer, J., Clarke, A. R., and Walsh, T. R. (2001) Novel Mechanism of Hydrolysis of Therapeutic β-Lactams by *Stenotrophomonas maltophilia* L1 Metallo-β-lactamase. *Journal of Biological Chemistry* **276**, 33638-33644
125. Carenbauer, A. L., Garrity, J. D., Periyannan, G., Yates, R. B., and Crowder, M. W. (2002) Probing substrate binding to metallo-beta-lactamase L1 from Stenotrophomonas maltophilia by using site-directed mutagenesis. *BMC Biochem* **3**, 4
126. Simm, A. M., Higgins, C. S., Carenbauer, A. L., Crowder, M. W., Bateson, J. H., Bennett, P. M., Clarke, A. R., Halford, S. E., and Walsh, T. R. (2002) Characterization of monomeric L1 metallo-beta -lactamase and the role of the N-terminal extension in negative cooperativity and antibiotic hydrolysis. *J Biol Chem* **277**, 24744-24752
127. Garrity, J. D., Pauff, J. M., and Crowder, M. W. (2004) Probing the dynamics of a mobile loop above the active site of L1, a metallo-beta-lactamase from Stenotrophomonas maltophilia, via site-directed mutagenesis and stopped-flow fluorescence spectroscopy. *J Biol Chem* **279**, 39663-39670

128. Garrity, J. D., Bennett, B., and Crowder, M. W. (2005) Direct evidence that the reaction intermediate of metallo-beta-lactamase L1 is metal bound. *Biochemistry* **44**, 1078-1087
129. Magdalena, S., Jean-Marie, F., Gian Maria, R., and Jean-Denis, D. (2006) Postgenomic Scan of Metallo-β-Lactamase Homologues in *Rhizobacteria*: Identification and Characterization of BJP-1, a Subclass B3 Ortholog from *Bradyrhizobium japonicum*. *Antimicrobial Agents and Chemotherapy* **50**, 1973-1981
130. Docquier, J. D., Benvenuti, M., Calderone, V., Stoczko, M., Menciassi, N., Rossolini, G. M., and Mangani, S. (2010) High-resolution crystal structure of the subclass B3 metallo-beta-lactamase BJP-1: rational basis for substrate specificity and interaction with sulfonamides. *Antimicrob Agents Chemother* **54**, 4343-4351
131. Wang, X., Randall, C. R., True, A. E., and Que, L., Jr. (1996) X-ray absorption spectroscopic studies of the FeZn derivative of uteroferrin. *Biochemistry* **35**, 13946-13954
132. Paola Sandra, M., Moreno, G., Fabrice, B., Letizia, B., Josette, L.-B., Gianfranco, A., Bart, D., Jozef van, B., Jean-Marie, F., and Gian Maria, R. (2001) Biochemical Characterization of the FEZ-1 Metallo-β-Lactamase of *Legionella gormanii* ATCC 33297T Produced in Escherichia coli. *Antimicrobial Agents and Chemotherapy* **45**, 1254-1262
133. Garcia-Saez, I., Mercuri, P. S., Papamicael, C., Kahn, R., Frere, J. M., Galleni, M., Rossolini, G. M., and Dideberg, O. (2003) Three-dimensional structure of FEZ-1, a monomeric subclass B3 metallo-beta-lactamase from Fluoribacter gormanii, in native form and in complex with D-captopril. *J Mol Biol* **325**, 651-660
134. Mercuri, P. S., Garcia-Saez, I., De Vriendt, K., Thamm, I., Devreese, B., Van Beeumen, J., Dideberg, O., Rossolini, G. M., Frere, J. M., and Galleni, M. (2004) Probing the specificity of the subclass B3 FEZ-1 metallo-beta-lactamase by site-directed mutagenesis. *J Biol Chem* **279**, 33630-33638
135. Salimraj, R., Zhang, L., Hinchliffe, P., Wellington, E. M., Brem, J., Schofield, C. J., Gaze, W. H., and Spencer, J. (2016) Structural and Biochemical Characterization of Rm3, a SubClass B3 Metallo-beta-Lactamase Identified from a Functional Metagenomic Study. *Antimicrob Agents Chemother*
136. Allen, H. K., Moe, L. A., Rodbumrer, J., Gaarder, A., and Handelsman, J. (2009) Functional metagenomics reveals diverse beta-lactamases in a remote Alaskan soil. *The ISME journal* **3**, 243-251
137. Hou, D. (2014) *Structural characterisation and directed evolution of AIM-1.* PhD, ANU
138. Vella, P., Miraula, M., Phelan, E., Leung, E. W., Ely, F., Ollis, D. L., McGeary, R. P., Schenk, G., and Mitic, N. (2013) Identification and characterization of an unusual metallo-b-lactamase from *Serratia proteamaculans*. *Journal of biological inorganic chemistry : JBIC : a publication of the Society of Biological Inorganic Chemistry* **18**, 855-863
139. Wang, Z., Fast, W., and Benkovic, S. J. (1999) On the mechanism of the metallo-beta-lactamase from Bacteroides fragilis. *Biochemistry* **38**, 10013-10023
140. Kaminskaia, N. V., Spingler, B., and Lippard, S. J. (2001) Intermediate in beta-lactam hydrolysis catalyzed by a dinuclear zinc(II) complex: relevance to the mechanism of metallo-beta-lactamase. *Journal of the American Chemical Society* **123**, 6555-6563
141. Concha, N. O., Rasmussen, B. A., Bush, K., and Herzberg, O. (1996) Crystal structure of the wide-spectrum binuclear zinc beta-lactamase from Bacteroides fragilis. *Structure (London, England : 1993)* **4**, 823-836
142. Jackson, C. J., Hadler, K. S., Carr, P. D., Oakley, A. J., Yip, S., Schenk, G., and Ollis, D. L. (2008) Malonate-bound structure of the glycerophosphodiesterase from *Enterobacter aerogenes* (GpdQ) and characterization of the native Fe(II) metal-ion

preference. *Acta crystallographica. Section F, Structural biology and crystallization communications* **64**, 681-685
143. Mirams, R. E., Smith, S. J., Hadler, K. S., Ollis, D. L., Schenk, G., and Gahan, L. R. (2008) Cadmium(II) complexes of the glycerophosphodiester-degrading enzyme GpdQ and a biomimetic N,O ligand. *Journal of biological inorganic chemistry : JBIC : a publication of the Society of Biological Inorganic Chemistry* **13**, 1065-1072
144. Hadler, K. S., Mitic, N., Yip, S. H., Gahan, L. R., Ollis, D. L., Schenk, G., and Larrabee, J. A. (2010) Electronic structure analysis of the dinuclear metal center in the bioremediator glycerophosphodiesterase (GpdQ) from *Enterobacter aerogenes*. *Inorganic chemistry* **49**, 2727-2734
145. Hadler, K. S., Mitic, N., Yip, S. H., Gahan, L. R., Ollis, D. L., Schenk, G., and Larrabee, J. A. (2010) Electronic structure analysis of the dinuclear metal center in the bioremediator glycerophosphodiesterase (GpdQ) from Enterobacter aerogenes. *Inorg Chem* **49**, 2727-2734
146. Bebrone, C., Lassaux, P., Vercheval, L., Sohier, J. S., Jehaes, A., Sauvage, E., and Galleni, M. (2010) Current Challenges in Antimicrobial Chemotherapy Focus on beta-Lactamase Inhibition. *DRUGS* **70**, 651-679
147. García-Sáez, I., Mercuri, P. S., Papamicael, C., Kahn, R., Frère, J. M., Galleni, M., Rossolini, G. M., and Dideberg, O. (2003) Three-dimensional structure of FEZ-1, a monomeric subclass B3 metallo-beta-lactamase from Fluoribacter gormanii, in native form and in complex with D-captopril. *Journal of molecular biology* **325**, 651-660
148. Pollini, S., Maradei, S., Pecile, P., and Olivo, G. (2013) FIM-1, a new acquired metallo-β-lactamase from a Pseudomonas aeruginosa clinical isolate from Italy. *Antimicrobial agents …*
149. Page, M. I., and Badarau, A. (2008) The mechanisms of catalysis by metallo β-lactamases. *Bioinorganic Chemistry and Applications* **2008**, 1-14
150. Crowder, M. W., Spencer, J., and Vila, A. J. (2006) Metallo-b-lactamases: novel weaponry for antibiotic resistance in bacteria. *Accounts of Chemical Research* **39**, 721-728
151. Rasia, R. M., and Vila, A. J. . (2002) Exploring the role and the binding affinity of a second zinc equivalent in B. cereus metallo- -lactamase. *Biochemistry* **41**, 1853-1860
152. Paul-Soto, R., Zeppezauer, M., Adolph, H.-W., Bauer, R., Frère, J.-M., Galleni, M., Meyer-Klaucke, W., Nolting, H., Rossolini, G. M., De Seny, D., and Hernandez-Valladares, M. (1999) Mono- and binuclear Zn(II)-β-lactamase. Role of the conserved cysteine in the catalytic mechanism. *Journal of Biological Chemistry* **274**, 13242-13249
153. Palzkill, T. (2013) Metallo-beta-lactamase structure and function. *Ann N Y Acad Sci* **1277**, 91-104
154. Wilcox, D. E. (1996) Binuclear metallohydrolases. *Chemical Reviews* **96**, 2435-2458
155. Schenk, G., Mitić, N., Gahan, L. R., Ollis, D. L., McGeary, R. P., and Guddat, L. W. (2012) Binuclear Metallohydrolases: Complex Mechanistic Strategies for a Simple Chemical Reaction. *Accounts of Chemical Research* **45**, 15931603
156. Fisher, J. F., Meroueh, S. O., and Mobashery, S. (2005) Bacterial resistance to beta-lactam antibiotics: compelling opportunism, compelling opportunity. *Chem Rev* **105**, 395-424
157. Crowder, M. W., Spencer, J., and Vila, A. J. (2006) Metallo-beta-lactamases: novel weaponry for antibiotic resistance in bacteria. *Acc. Chem. Res.* **39**, 721-728
158. Yong, D., Toleman, M. A., Bell, J., Ritchie, B., Pratt, R., Ryley, H., and Walsh, T. R. . (2012). *Antimicrobial agents and chemotherapy* **56**, 6154-6159
159. Schramm, V. L. (2007) Enzymatic transition state theory and transition state analogue design. *The Journal of Biological Chemistry* **282**, 28297-28300

160. Schramm, V. L. (2013) Transition States, analogues, and drug development. *ACS chemical biology* **8**, 71-81
161. Schenk, G., Mitić, N., Hanson, G. R., and Comba, P. (2013) Purple acid phosphatase: A journey into the function and mechanism of a colorful enzyme. *Coord. Chem. Rev.* **257**, 473-482
162. Oddie, G. W., Schenk, G., Angel, N. Z., Walsh, N., Guddat, L. W., de Jersey, J., Cassady, A. I., Hamilton, S. E., and Hume, D. A. (2000) Structure, function, and regulation of tartrate-resistant acid phosphatase. *Bone* **27**, 575-584
163. Mitić, N., Valizadeh, M., Leung, E. W. W., de Jersey, J., Hamilton, S., Hume, D. A., Cassady, A. I., and Schenk, G. (2005) Human tartrate-resistant acid phosphatase becomes an effective ATPase upon proteolytic activation. *Archives of biochemistry and biophysics* **439**, 154-164
164. Bernhardt, P. V., Schenk, G., and Wilson, G. J. (2004) Direct electrochemistry of porcine purple acid phosphatase (uteroferrin). *Biochemistry* **43**, 10387-10392
165. Guddat, L. W., McAlpine, A. S., Hume, D., Hamilton, S., de Jersey, J., and Martin, J. L. (1999) Crystal structure of mammalian purple acid phosphatase. *Structure* **7**, 757-767
166. Lindqvist, Y., Johansson, E., Kaija, H., Vihko, P., and Schneider, G. (1999) Three-dimensional structure of a mammalian purple acid phosphatase at 2.2 Å resolution with a -(hydr) oxo bridged di-iron center. *Journal of molecular biology* **291**, 135-147
167. Schenk, G., Gahan, L. R., Carrington, L. E., Mitic, N., Valizadeh, M., Hamilton, S. E., Jersey, J., and Guddat, L. W. (2005) Phosphate forms an unusual tripodal complex with the Fe-Mn center of sweet potato purple acid phosphatase. *Proceedings of the National Academy of Sciences* **102**, 273-278
168. Strater, N., Jasper, B., Scholte, M., Krebs, B., Duff, A. P., Langley, D. B., Han, R., Averill, B. A., Freeman, H. C., and Guss, J. M. (2005) Crystal structures of recombinant human purple Acid phosphatase with and without an inhibitory conformation of the repression loop. *Journal of Molecular Biology* **351**, 233-246
169. Schenk, G., Elliott, T., Leung, E., Carrington, L., Mitic, N., Gahan, L., and Guddat, L. (2008) Crystal structures of a purple acid phosphatase, representing different steps of this enzyme's catalytic cycle. *BMC Struct. Biol.* **8**, 6
170. Merkx, M., and Averill, B. A. (1998) The activity of oxidized bovine spleen purple acid phosphatase is due to an Fe (III) Zn (II)'impurity'. *Biochemistry* **37**, 11223-11231
171. Merkx, M., Pinkse, M. W. H., and Averill, B. A. (1999) Evidence for Nonbridged Coordination of *p*-Nitrophenyl Phosphate to the Dinuclear Fe(III),Mn(II) Center in Bovine Spleen Purple Acid Phosphatase during Enzymatic Turnover. *Biochem.* **38**, 9914-9925
172. Funhoff, E. G., Klaassen, C. H. W., and Samyn, B. (2001) The highly exposed loop region in mammalian purple acid phosphatase controls the catalytic activity. *Chembiochem.* **4**, 355-363
173. Twitchett, M. B., Schenk, G., Aquino, M. A. S., and Yiu, D. T. Y. (2002) Reactivity of MII metal-substituted derivatives of pig purple acid phosphatase (Uteroferrin) with phosphate. *Inorganic …*
174. Mitić, N., Hadler, K. S., Gahan, L. R., Hengge, A. C., and Schenk, G. (2010) The divalent metal ion in the active site of uteroferrin modulates substrate binding and catalysis. *Journal of the American Chemical Society* **132**, 7049-7054
175. Yang, Y.-S., McCormick, J. M., and Solomon, E. I. (1997) Circular dichroism and magnetic circular dichroism studies of the mixed-valence binuclear non-heme iron active site in uteroferrin and its anion complexes. *Journal of the American Chemical Society* **119**, 11832-11842

176. Wang, X., Ho, R. Y. N., Whiting, A. K., and Que, L. (1999) Spectroscopic Characterization of a Ternary Phosphatase, Substrate, Fluoride Complex. Mechanistic Implications for Dinuclear Hydrolases. *J. Am. Chem. Soc.* **121**, 9235-9236
177. Smoukov, S. K., Quaroni, L., Wang, X., Doan, P. E., Hoffman, B. M., and Que, L. (2002) Electron-Nuclear Double Resonance Spectroscopic Evidence for a Hydroxo-Bridge Nucleophile Involved in Catalysis by a Dinuclear Hydrolase. *J. Am. Chem. Soc.* **124**, 2595-2603
178. Mitic, N., Noble, C. J., Gahan, L. R., Hanson, G. R., and Schenk, G. (2009) Metal-Ion Mutagenesis: Conversion of a Purple Acid Phosphatase from Sweet Potato to a Neutral Phosphatase with the Formation of an Unprecedented Catalytically Competent MnIIMnII Active Site. *J. Am. Chem. Soc.* **131**, 8173-8179
179. McPhillips, T. M., McPhillips, S. E., Chiu, H. J., Cohen, A. E., Deacon, A. M., Ellis, P. J., Garman, E., Gonzalez, A., Sauter, N. K., and Phizackerley, P. R. (2002) Blu-Ice and the Distributed Control System: software for data acquisition and instrument control at macromolecular crystallography beamlines. *Journal of synchrotron radiation* **9**, 401-406
180. Otwinowski, Z., and Minor, W. (1997) [20] Processing of X-ray diffraction data collected in oscillation mode. *Methods in enzymology* **276**, 307-326
181. Adams, P. D., Afonine, P. V., Bunkóczi, G., Chen, V. B., Davis, I. W., Echols, N., Headd, J. J., Hung, L.-W. W., Kapral, G. J., Grosse-Kunstleve, R. W., McCoy, A. J., Moriarty, N. W., Oeffner, R., Read, R. J., Richardson, D. C., Richardson, J. S., Terwilliger, T. C., and Zwart, P. H. (2010) PHENIX: a comprehensive Python-based system for macromolecular structure solution. *Acta crystallographica. Section D, Biological crystallography* **66**, 213-221
182. Emsley, P., Lohkamp, B., and Scott, W. G. (2010) Features and development of Coot. *… Section D: Biological …*
183. Painter, J., and Merritt, E. A. (2006) Optimal description of a protein structure in terms of multiple groups undergoing TLS motion. *Acta crystallographica. Section D, Biological crystallography* **62**, 439-450
184. Neves, A., Lanznaster, M., Bortoluzzi, A. J., Peralta, R. A., Casellato, A., Castellano, E. E., Herrald, P., Riley, M. J., and Schenk, G. (2007) An Unprecedented $Fe^{III}Zn^{II}$ Complex that Mimics the Structural and Functional Properties of Purple Acid Phosphatases. *Journal of the American Chemical Society* **129**, 7486-7487
185. Comba, P., Gahan, L. R., Hanson, G. R., Mereacre, V., Noble, C. J., Powell, A. K., Prisecaru, I., Schenk, G., and Zajaczkowski-Fischer, M. (2012) Monoesterase activity of a purple acid phosphatase mimic with a cyclam platform. *Chemistry (Weinheim an der Bergstrasse, Germany)* **18**, 1700-1710
186. Bosch, S., Comba, P., Gahan, L. R., Hanson, G. R., Noble, C., Schenk, G., and Wadepohl, H. (2015) Selective Coordination of Gallium(III), Zinc(II), and Copper(II) by an Asymmetric Dinucleating Ligand: A Model for Metallophosphatases. *Chemistry (Weinheim an der Bergstrasse, Germany)* **21**, 18269-18279
187. Miller, G. T. J. (2002) *Living in the enviroment*, 12th ed., Belmont: Wadsworth/Thomson Learning
188. Sethunathan, N., and Yoshida, T. (1973) A Flavobacterium sp. that degrades diazinon and parathion. *Canadian Journal of Microbiology* **19**, 873-875
189. Horne, I., Sutherland, T. D., Harcourt, R. L., Russell, R. J., and Oakeshott, J. G. (2002) Identification of an OPD (Organophosphate Degradation) Gene in an *Agrobacterium* Isolate. *Appl. Environ. Microbiol.* **68**, 3371-3376

190. Kim, J., Tsai, P.-C., Chen, S.-L., Himo, F., Almo, S. C., and Raushel, F. M. (2008) Structure of Diethyl Phosphate Bound to the Binuclear Metal Center of Phosphotriesterase. *Biochemistry* **47**, 9497-9504
191. Jackson, C., Carr, P. D., Kim, H. K., Liu, J.-W., Herrald, P., Mitic, N., Schenk, G., Smith, C. A., and Ollis, D. L. (2006) Anomalous scattering analysis of *Agrobacterium radiobacter* phosphotriesterase: the prominent role of iron in the heterobinuclear active site. *Biochemistry Journal* **397**, 501-508
192. Aubert, S. D., Li, Y., and Raushel, F. M. (2004) Mechanism for the Hydrolysis of Organophosphates by the Bacterial Phosphotriesterase. *Biochem.* **43**, 5707-5715
193. Foo, J.-L., Jackson, C. J., Carr, P. D., Kim, H.-K., Schenk, G., Gahan, L. R., and Ollis, D. L. (2010) Mutation of outer-shell residues modulates metal ion co-ordination strength in a metalloenzyme. *The Biochemical journal* **429**, 313-321
194. Ely, F., Foo, J.-L., Jackson, C. J., Gahan, L. R., Ollis, D. L., and Schenk, G. (2007) Enzymatic Bioremediation: Organophosphate Degradation by Binuclear Metallo-Hydrolases. *Current Topics in Biochemical Research* **9**, 63-78
195. Pedroso, M. M., Ely, F., Mitić, N., Carpenter, M. C., Gahan, L. R., Wilcox, D. E., Larrabee, J. L., Ollis, D. L., and Schenk, G. (2014) Comparative investigation of the reaction mechanisms of the organophosphate-degrading phosphotriesterases from Agrobacterium radiobacter (OpdA) and Pseudomonas diminuta (OPH). *Journal of biological inorganic chemistry : JBIC : a publication of the Society of Biological Inorganic Chemistry* **19**, 1263-1275
196. Todd, M. J., and Hausinger, R. P. (2000) Fluoride inhibition of Klebsiella aerogenes urease: mechanistic implications of a pseudo-uncompetitive, slow-binding inhibitor. *Biochemistry* **39**, 5389-5396
197. Pethe, S., Boucher, J. L., and Mansuy, D. (2002) Interaction of anions with rat liver arginase: specific inhibitory effects of fluoride. *Journal of inorganic biochemistry* **88**, 397-402
198. Benini, S., Cianci, M., Mazzei, L., and Ciurli, S. (2014) Fluoride inhibition of Sporosarcina pasteurii urease: structure and thermodynamics. *JBIC Journal of Biological Inorganic Chemistry*
199. Elliott, T. W., Mitic, N., Gahan, L. R., Guddat, L. W., and Schenk, G. (2006) Inhibition studies of purple acid phosphatases: Implications for the catalytic mechanism. *Journal of the Brazilian Chemical Society* **17**, 1558-1565
200. Schenk, G., Elliott, T. W., Leung, E., Carrington, L. E., Mitic, N., Gahan, L. R., and Guddat, L. W. (2008) Crystal structures of a purple acid phosphatase, representing different steps of this enzyme's catalytic cycle. *BMC structural biology* **8**, 6
201. Ely, F., Hadler, K. S., Mitic, N., Gahan, L., Ollis, D. L., Larrabee, J. A., and Schenk, G. (2011) Electronic and geometric structure of the organophosphate-degrading enzyme from *Agrobacterium radiobacter* (OpdA). *J. Biol. Inorg. Chem.* **16**, 777-787
202. Ely, F., Pedroso, M. M., Gahan, L. R., Ollis, D. L., Guddat, L. W., and Schenk, G. (2012) Phosphate-bound structure of an organophosphate-degrading enzyme from Agrobacterium radiobacter. *Journal of inorganic biochemistry* **106**, 19-22
203. Holm, L., and Sander, C. (1997) An evolutionary treasure: unification of a broad set of amidohydrolases related to urease. *Proteins: Structure, Function, and Genetics* **28**, 72-82
204. Chen, L. (2017) Notes from the field: pan-resistant New Delhi metallo-beta-lactamase-producing Klebsiella pneumoniae—Washoe County, Nevada, 2016. *MMWR. Morbidity and mortality weekly report* **66**
205. Fisher, J. F., Meroueh, S. O., and Mobashery, S. (2005) Bacterial resistance to beta-lactam antibiotics: compelling opportunism, compelling opportunity. *Chemical reviews* **105**, 395-424

206. Crowder, M. W., Spencer, J., and Vila, A. J. (2006) Metallo-beta-lactamases: novel weaponry for antibiotic resistance in bacteria. *Accounts of chemical research* **39**, 721-728
207. Roy, S., Viswanathan, R., Singh, A. K., Das, P., and Basu, S. (2011) Sepsis in neonates due to imipenem-resistant Klebsiella pneumoniae producing NDM-1 in India. *J Antimicrob Chemother* **66**, 1411-1413
208. Phelan, E. K., Miraula, M., Selleck, C., Ollis, D. L., Schenk, G., and Mitić, N. (2014) Metallo-β-Lactamases: A Major Threat to Human Health. *American Journal of Molecular Biology* **04**, 89
209. Hawkey, P. M. (2015) Multidrug-resistant Gram-negative bacteria: a product of globalization. *J Hosp Infect* **89**, 241-247
210. Allen, H. K., Moe, L. A., Rodbumrer, J., Gaarder, A., and Handelsman, J. (2008) Functional metagenomics reveals diverse β-lactamases in a remote Alaskan soil. *The ISME Journal* **3**, 243-251
211. Allen, H. K., Donato, J., Wang, H., Cloud-Hansen, K. A., Davies, J., and Handelsman, J. (2010) Call of the wild: antibiotic resistance genes in natural environments. *Nature Reviews Microbiology*
212. Miraula, M., Schenk, G., and Mitić, N. (2015) Promiscuous metallo-β-lactamases: MIM-1 and MIM-2 may play an essential role in quorum sensing networks. *Journal of inorganic biochemistry*
213. Spencer, J., Read, J., Sessions, R. B., Howell, S., Blackburn, G. M., and Gamblin, S. J. (2005) Antibiotic recognition by binuclear metallo-beta-lactamases revealed by X-ray crystallography. *Journal of the American Chemical Society* **127**, 14439-14444
214. Bebrone, C. (2007) Metallo-beta-lactamases (classification, activity, genetic organization, structure, zinc coordination) and their superfamily. *Biochem. Pharmacol.* **74**
215. Hernandez Valladares, M., Rossolini, G. M., Amicosante, G., Adolph, H.-W., Kiefer, M., Heinz, U., Paul Soto, R., Meyer-Klaucke, W., Nolting, H. F., Zeppezauer, M., Galleni, M., and Frère, J.-M. . (2000). *FEBS letters* **467**, 221-225
216. Leiros, H. K., Borra, P. S., Brandsdal, B. O., Edvardsen, K. S., Spencer, J., Walsh, T. R., and Samuelsen, O. . (2012). *Antimicrobial agents and chemotherapy* **56**, 4341-4353
217. Vella, P., Miraula, M., Phelan, E., Leung, E. W., Ely, F., Ollis, D. L., McGeary, R. P., Schenk, G., and Mitic, N. (2013). *Journal of biological inorganic chemistry : JBIC : a publication of the Society of Biological Inorganic Chemistry* **18**, 855-863
218. Hadler, K. S., Tanifum, E. A., Yip, S. H., Mitic, N., Guddat, L. W., Jackson, C. J., Gahan, L. R., Nguyen, K., Carr, P. D., Ollis, D. L., Hengge, A. C., Larrabee, J. A., and Schenk, G. . (2008). *Journal of the American Chemical Society* **130**, 14129-14138
219. Hadler, K. S., Mitić, N., Ely, F., Hanson, G. R., Gahan, L. R., Larrabee, J. A., Ollis, D. L., and Schenk, G. (2009) Structural flexibility enhances the reactivity of the bioremediator glycerophosphodiesterase by fine-tuning its mechanism of hydrolysis. *Journal of the American Chemical Society* **131**, 11900-11908
220. Hadler, K. S., Mitić, N., Yip, S. H., Gahan, L. R., Ollis, D. L., Schenk, G., and Larrabee, J. A. (2010) Electronic structure analysis of the dinuclear metal center in the bioremediator glycerophosphodiesterase (GpdQ) from Enterobacter aerogenes. *Inorganic chemistry* **49**, 2727-2734
221. Perez-Llarena, F. J., and Bou, G. . (2009). *CURRENT MEDICINAL CHEMISTRY* **16**, 3740-3765
222. Livermore, D. M., and Woodford, N. (2006). *Trends in microbiology 1* **14**, 413-420
223. Lee, K., Yum, J. H., Yong, D., Lee, H. M., Kim, H. D., Docquier, J.-D., Rossolini, G. M., and Chong, Y. . (2005). *Antimicrobial agents and chemotherapy* **49**, 4485-4491

224. Maltezou, H. C. (2009). *International Journal of Antimicrobial Agents* **33**, 405
225. Perez, F., Hujer, A. M., Hujer, K. M., Decker, B. K., Rather, P. N., and Bonomo, R. A. . (2007). *Antimicrobial agents and chemotherapy* **51**, 3471-3484
226. Yanchak, M. P., Taylor, R. A., and Crowder, M. W. . (2000). *Biochemistry* **39**, 11330-11339
227. Miraula, M., Whitaker, J. J., Schenk, G., and Mitić, N. (2015) β-Lactam antibiotic-degrading enzymes from non-pathogenic marine organisms: a potential threat to human health. *Journal of biological inorganic chemistry : JBIC : a publication of the Society of Biological Inorganic Chemistry* **20**, 639-651
228. Segel, I. H. (1993) *Enzyme kinetics: Behaviour and analysis of rapid equilibrium and steady state enzyme systems*, Wiley and sons, United States of America
229. Larrabee, J. A., Schenk, G., Mitić, N., and Riley, M. J. (2015) Use of magnetic circular dichroism to study dinuclear metallohydrolases and the corresponding biomimetics. *European biophysics journal : EBJ* **44**, 393-415
230. Ely, F., Hadler, K. S., Mitic, N., Gahan, L. R., Ollis, D. L., Plugis, N. M., Russo, M. T., Larrabee, J. A., and Schenk, G. (2011). *Journal of biological inorganic chemistry : JBIC : a publication of the Society of Biological Inorganic Chemistry* **16**, 777-787
231. Pedroso, M. M., Larrabee, J. A., Ely, F., Gwee, S. E., Mitić, N., Ollis, D. L., Gahan, L. R., and Schenk, G. (2016) Ca(II) Binding Regulates and Dominates the Reactivity of a Transition-Metal-Ion-Dependent Diesterase from Mycobacterium tuberculosis. *Chemistry (Weinheim an der Bergstrasse, Germany)* **22**, 999-1009
232. Tadrowski, S., Pedroso, M. M., Sieber, V., Larrabee, J. A., Guddat, L. W., and Schenk, G. (2016) Metal Ions Play an Essential Catalytic Role in the Mechanism of Ketol-Acid Reductoisomerase. *Chemistry (Weinheim an der Bergstrasse, Germany)*
233. Hawk, M. J., Breece, R. M., Hajdin, C. E., Bender, K. M., Zhenxin, H., Costello, A. L., Bennett, B., Tierney, D. L., and Crowder, M. W. (2009) Differential binding of Co(II) and Zn(II) to metallo-b-lactamase Bla2 from *Bacillus anthracis*. *Journal of the American Chemical Society* **131**, 10753
234. Zhigang Wang , W. F., and Stephen J. Benkovic *. (1998) Direct Observation of an Enzyme-Bound Intermediate in the Catalytic Cycle of the Metallo-β-Lactamase from Bacteroides fragilis. *J. Am. Chem. Soc.* **120**, 10788–10789
235. Barshop, B. A., Wrenn, R. F., and Frieden, C. (1983) Analysis of numerical methods for computer simulation of kinetic processes: development of KINSIM--a flexible, portable system. *Analytical biochemistry* **130**, 134-145
236. Frieden, C. (1993) Numerical integration of rate equations by computer. *Trends Biochem Sci* **18**, 58-60
237. Frieden, C. (1994) Numerical integration of rate equations by computer: an update. *Trends Biochem Sci* **19**, 181-182
238. McGeary, R. P., Schenk, G., and Guddat, L. W. (2014) The applications of binuclear metallohydrolases in medicine: recent advances in the design and development of novel drug leads for purple acid phosphatases, metallo-β-lactamases and arginases. *European journal of medicinal chemistry* **76**, 132-144
239. Smith, S. J., Casellato, A., Hadler, K. S., Mitic, N., Riley, M. J., Bortoluzzi, A. J., Szpoganicz, B., Schenk, G., Neves, A., and Gahan, L. R. (2007) The reaction mechanism of the Ga(III)Zn(II) derivative of uteroferrin and corresponding biomimetics. *Journal of biological inorganic chemistry : JBIC : a publication of the Society of Biological Inorganic Chemistry* **12**, 1207-1220
240. Schenk, G., Peralta, R. A., Batista, S., Bortoluzzi, A. J., Szpoganicz, B., Dick, A. K., Herrald, P., Hanson, G. R., Szilagyi, R. K., and Riley, M. J. (2008) Probing the role of the divalent metal ion in uteroferrin using metal ion replacement and a comparison to isostructural biomimetics. *JBIC Journal of Biological Inorganic Chemistry* **13**, 139-155

241. Llarrull, L. I., Fabiane, S. M., Kowalski, J. M., Bennett, B., Sutton, B. J., and Vila, A. J. (2007) Asp-120 locates Zn2 for optimal metallo-beta-lactamase activity. *The Journal of Biological Chemistry* **282**, 18276-18285
242. Cahill, S. T., Tarhonskaya, H., Rydzik, A. M., Flashman, E., McDonough, M. A., Schofield, C. J., and Brem, J. (2016) Use of ferrous iron by metallo-β-lactamases. *Journal of inorganic biochemistry*
243. Kantacha A, B. R., Smith S.J, Schenk G, Gahan L.R. (2011) Phosphate ester cleavage promoted by a tetrameric iron(III) complex.
. *J Biol Inorg Chem.* **16**, 25-32
244. Spencer, J., Clarke, A. R., and Walsh, T. R. (2001) Novel mechanism of hydrolysis of therapeutic beta-lactams by Stenotrophomonas maltophilia L1 metallo-beta-lactamase. *The Journal of biological chemistry* **276**, 33638-33644
245. Dang, Q., and Frieden, C. (1997) New PC versions of the kinetic-simulation and fitting programs, KINSIM and FITSIM. *Trends in biochemical sciences* **22**, 317
246. Solomon, E. I., Neidig, M. L., and Schenk, G. (2004) Magnetic circular dichroism of paramagnetic species. *Elsevier/Pergamon*
247. Solomon, E. I., Brunold, T. C., Davis, M. I., Kemsley, J. N., Lee, S. K., Lehnert, N., Neese, F., Skulan, A. J., Yang, Y. S., and Zhou, J. (2000) Geometric and electronic structure/function correlations in non-heme iron enzymes. *Chem Rev* **100**, 235-350
248. Solomon, E. I. (1995) Magnetic
circular dichroism spectroscopy as a probe of the geometric and
electronic structure of non-heme ferrous enzymes. *Coord. Chem. Rev.* **144**, 369-460
249. Mason, W. R. (2007) Magnetic Circular Dichroism Spectroscopy. *Magnetic Circular Dichroism Spectroscopy*
250. Holz, R. C. (2002) The aminopeptidase from Aeromonas proteolytica: structure and mechanism of co-catalytic metal centers involved in peptide hydrolysis. *Coordination chemistry reviews*
251. Weston, J. (2005) Mode of action of bi-and trinuclear zinc hydrolases and their synthetic analogues. *Chemical reviews*
252. Schenk, G., Mitic, N., Gahan, L. R., Ollis, D. L., McGeary, R. P., and Guddat, L. W. (2012) Binuclear metallohydrolases: complex mechanistic strategies for a simple chemical reaction. *Accounts of Chemical Research* **45**, 1593-1603
253. Stephens, P. J. (1976) Magnetic circular dichroism. *Adv. Chem. Phys*
254. Larrabee, J. A., Schenk, G., Mitic, N., and Riley, M. J. (2015) Use of magnetic circular dichroism to study dinuclear metallohydrolases and the corresponding biomimetics. *Eur Biophys J* **44**, 393-415
255. Hadler, K. S., Mitic, N., Ely, F., Hanson, G. R., Gahan, L. R., Larrabee, J. A., Ollis, D. L., and Schenk, G. (2009) Structural flexibility enhances the reactivity of the bioremediator glycerophosphodiesterase by fine-tuning its mechanism of hydrolysis. *Journal of the American Chemical Society* **131**, 11900-11908
256. Ely, F., Hadler, K. S., Mitic, N., Gahan, L. R., Ollis, D. L., Plugis, N. M., Russo, M. T., Larrabee, J. A., and Schenk, G. (2011) Electronic and geometric structures of the organophosphate-degrading enzyme from *Agrobacterium radiobacter* (OpdA). *Journal of biological inorganic chemistry : JBIC : a publication of the Society of Biological Inorganic Chemistry* **16**, 777-787
257. Pedroso, M. M., Larrabee, J. A., Ely, F., Gwee, S. E., Mitic, N., Ollis, D. L., Gahan, L. R., and Schenk, G. (2016) Ca(II) Binding Regulates and Dominates the Reactivity of a Transition-Metal-Ion-Dependent Diesterase from Mycobacterium tuberculosis. *Chemistry* **22**, 999-1009

258. Larrabee, J. A., Johnson, W. R., and Volwiler, A. S. (2009) Magnetic circular dichroism study of a dicobalt(II) complex with mixed 5- and 6-coordination: a spectroscopic model for dicobalt(II) hydrolases. *Inorg Chem* **48**, 8822-8829
259. Brown. L, M. J., LeMay. H, Langford. S, Bursten. E, Sagatys. D. (2010) *Chemistry The Central Science: A broad perspective 2e*, 2 ed., Pearson, Australia
260. Daumann, L. J., Schenk, G., Ollis, D. L., and Gahan, L. R. (2014) Spectroscopic and mechanistic studies of dinuclear metallohydrolases and their biomimetic complexes. *Dalton Transactions*
261. Larrabee, J. A., Alessi, C. M., Asiedu, E. T., Cook, J. O., Hoerning, K. R., Klingler, L. J., Okin, G. S., Santee, S. G., and Volkert, T. L. (1997) Magnetic circular dichroism spectroscopy as a probe of geometric and electronic structure of cobalt(II)-substituted proteins: Ground-state zero- field splitting as a coordination number indicator. *Journal of the American Chemical Society* **119**, 4182-4196
262. Larrabee, J. A., Chyun, S. A., and Volwiler, A. S. (2008) Magnetic circular dichroism study of a dicobalt(II) methionine aminopeptidase/fumagillin complex and dicobalt II-II and II-III model complexes. *Inorg Chem* **47**, 10499-10508
263. Murray, K. S., Berry, K. J., and Larrabee, J. A. (2008) Dicobalt II− II, II− III, and III− III Complexes as Spectroscopic Models for Dicobalt Enzyme Active Sites. *Inorganic …*
264. Ostrovsky, S. M., Falk, K., Pelikan, J., and Brown, D. A. (2006) Orbital angular momentum contribution to the magneto-optical behavior of a binuclear cobalt (II) complex. *Inorganic …*
265. Ostrovsky, S., Tomkowicz, Z., and Haase, W. (2009) High-spin Co (II) in monomeric and exchange coupled oligomeric structures: Magnetic and magnetic circular dichroism investigations. *Coordination Chemistry Reviews*
266. Pedroso, M. M., Selleck, C., Bilyj, J., and Harmer, J. (2017) Reaction mechanism of the metallohydrolase CpsB, a promising target for novel antimicrobial agents. *Dalton …*
267. Pedroso, M. M., Ely, F., Lonhienne, T., Gahan, L. R., Ollis, D. L., Guddat, L. W., and Schenk, G. (2014) Determination of the catalytic activity of binuclear metallohydrolases using isothermal titration calorimetry. *J. Biol. Inorg. Chem.* **19**, 389-398
268. Pedroso, M. M., Ely, F., Mitic, N., Carpenter, M. C., Gahan, L. R., Wilcox, D. E., Larrabee, J. L., Ollis, D. L., and Schenk, G. (2014) Comparative investigation of the reaction mechanisms of the organophosphate-degrading phosphotriesterases from Agrobacterium radiobacter (OpdA) and Pseudomonas diminuta (OPH). *J Biol Inorg Chem* **19**, 1263-1275
269. Selleck, C. L., J. L., Harmer, J.; Guddat, L. W.; Mitić, N.; Helweh, W.; Ollis, D. L.; Craig, W. A.; Tierney, D. L.; Pedroso, M. M.; Schenk, G. (2016) AIM-1: An Antibiotic-Degrading Metallohydrolase That Displays Mechanistic Flexibility. *Chemistry - A Euroepan Journal **22***, 17704-17714
270. Larrabee, J. A., Schenk, G., Mitić, N., and Riley, M. J. (2015) Use of magnetic circular dichroism to study dinuclear metallohydrolases and the corresponding biomimetics. *European biophysics journal : EBJ*
271. Ely, F. (2010) *Structural and Functional Studies of the Organophosphate Degrading Enzyme (OpdA) and Other Related Phoshoesterases* PhD, The University of Queensland
272. Hadler, K. S., Mitic, N., Ely, F., Hanson, G. R., Gahan, L. R., Larrabee, J. A., Ollis, D. L., and Schenk, G. (2009) Structural Flexibility Enhances the Reactivity of the Bioremediator Glycerophosphodiesterase by Fine-Tuning Its Mechanism of Hydrolysis. *J. Am. Chem. Soc.* **131**, 11900-11908

273. Hadler, K. S., Tanifum, E. A., Yip, S. H.-C., Mitic, N., Guddat, L. W., Jackson, C. J., Gahan, L. R., Nguyen, K., Carr, P. D., Ollis, D. L., Hengge, A. C., Larrabee, J. A., and Schenk, G. (2008) Substrate-Promoted Formation of a Catalytically Competent Binuclear Center and Regulation of Reactivity in a Glycerophosphodiesterase from *Enterobacter aerogenes*. *J. Am. Chem. Soc.* **130**, 14129-14138
274. Hadler, K. S., Mitic, N., Yip, S. H.-C., Gahan, L. R., Ollis, D. L., Schenk, G., and Larrabee, J. A. (2010) Electronic Structure Analysis of the Dinuclear Metal Center in the Bioremediator Glycerophosphodiesterase (GpdQ) from Enterobacter aerogenes. *Inorg. Chem.* **49**, 2727-2734
275. Aravind, L., and Koonin, E. V. (1998) Phosphoesterase domains associated with DNA polymerases of diverse origins. *Nucleic acids research* **26**, 3746-3752
276. Judy K. Morona, R. M., David C. Miller, and James C. Paton. (2002) Streptococcus pneumoniae Capsule Biosynthesis Protein CpsB Is a Novel Manganese-Dependent Phosphotyrosine-Protein Phosphatase *J. Bacteriol.* **184**, 577-583
277. Selleck, C. L., J. L., Harmer, J.; Guddat, L. W.; Mitić, N.; Helweh, W.; Ollis, D. L.; Craig, W. A.; Tierney, D. L.; Pedroso, M. M.; Schenk, G. (2016) AIM-1: a paradigm B3-type metallo-β-lactamase displaying mechanistic flexibility. *Chemistry - A Euroepan Journal* ***in press***
278. Hou, C.-F. D., Liu, J.-w., Collyer, C., Mitić, N., Pedroso, M., Schenk, G., and Ollis, D. L. (2017) Insights into an evolutionary strategy leading to antibiotic resistance. *Scientific Reports* **7**, 40357
279. Pedroso, M. M., Ely, F., Carpenter, M. C., and Mitic, N. (2017) Mechanistic Insight from Calorimetric Measurements of the Assembly of the Binuclear Metal Active Site of Glycerophosphodiesterase (GpdQ) from Enterobacter …. *Biochemistry*

Appendix A

Multiple sequence alignment including MBLs AIM-1, MIM-1, MIM-2, SMB-1, L1, BJP, FEZ-1 and RM3. Sequences were extracted from the protein data bank and were aligned using online software Clustal Omega (http://www.ebi.ac.uk/Tools/msa/clustalo/). The alignment was then manipulated using online software ESPript3 (http://espript.ibcp.fr/ESPript/ESPript/).

Highly conserved residues are highlighted in red whilst homologous regions are surrounded by blue boxes. Secondary structure features for MIM-2 are shown above the alignment, whilst secondary structure features for AIM-1 are shown below the alignment for comparison.

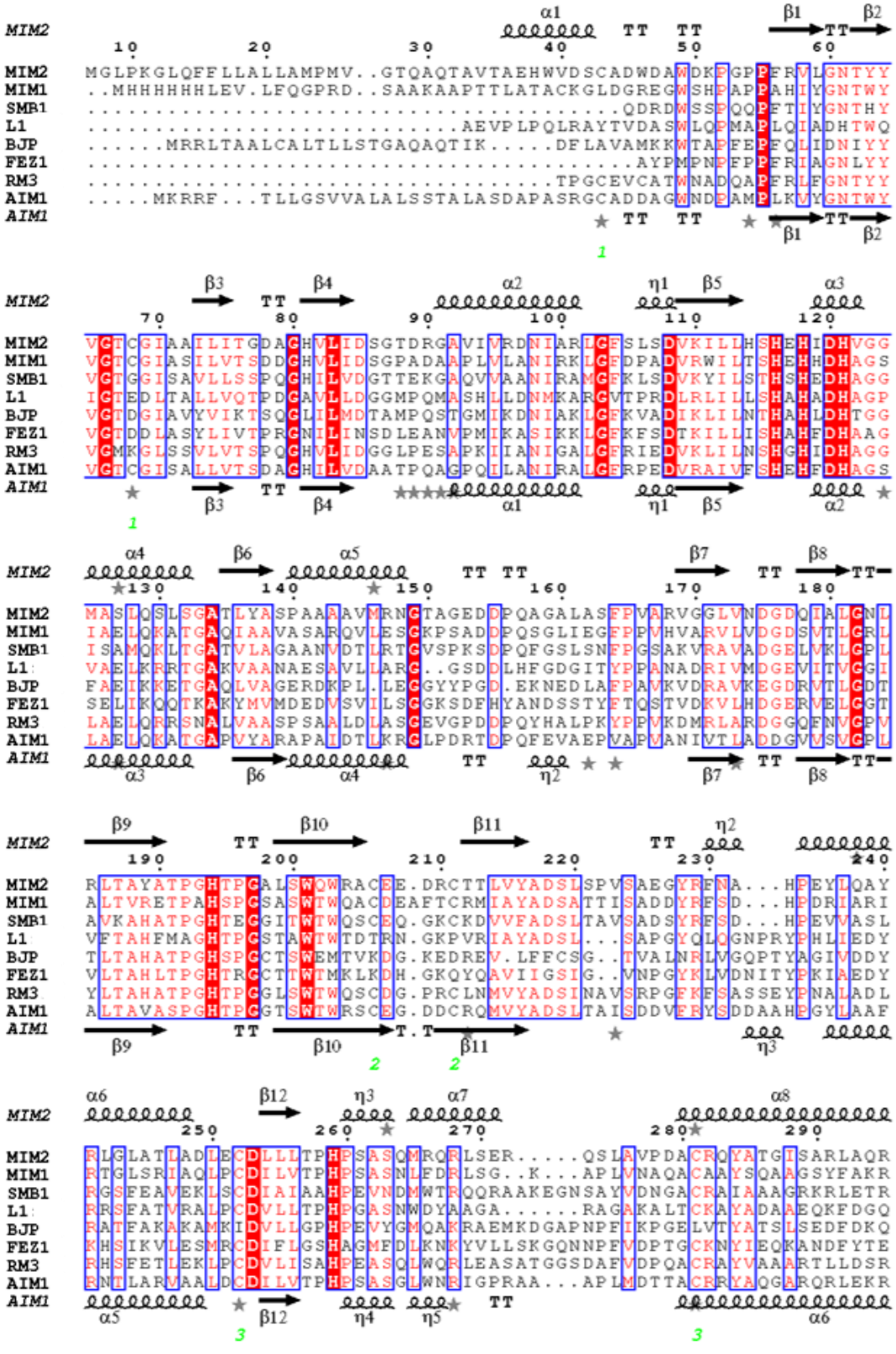
MIM2
MIM1
SMB1
L1
BJP
FEZ1
RM3
AIM1
AIM1